TECHNISCHE UNIVERSITÄT MÜNCHEN

TUM School of Engineering and Design

AN APPLICATION OF MULTI-FIDELITY UNCERTAINTY QUANTIFICATION FOR COMPUTATIONAL WIND ENGINEERING

Mayu Sakuma

Vollständiger Abdruck der von der TUM School of Engineering and Design der Technischen Universität München zur Erlangung des akademischen Grades einer

Doktorin der Ingenieurwissenschaften

genehmigten Dissertation.

Vorsitzender:

Prof. Dr.-Ing. habil. Michael Manhart

Prüfer der Dissertation:

1. Prof. Dr.-Ing. Kai-Uwe Bletzinger
2. Prof. Francesco Montomoli, Ph.D.

Die Dissertation wurde am 21.12.2021 bei der Technischen Universität München eingereicht und durch die TUM School of Engineering and Design am 25.04.2022 angenommen.

Schriftenreihe des Lehrstuhls für Statik
TU München

Band 52

Mayu Sakuma

AN APPLICATION OF MULTI-FIDELITY UNCERTAINTY QUANTIFICATION FOR COMPUTATIONAL WIND ENGINEERING

München 2022

Veröffentlicht durch

Kai-Uwe Bletzinger
Lehrstuhl für Statik
Technische Universität München
Arcisstr. 21
80333 München

Telefon: +49(0)89 289 22422
Telefax: +49(0)89 289 22421
E-Mail: kub@tum.de
Internet: www.cee.ed.tum.de/st/startseite/

ISBN: 978-3-943683-41-7

Kurzfassung

In dieser Arbeit wird die Multi-Fidelity Non-Intrusive Polynomial Chaos Methode (MF-NIPC) auf die numerische Simulation im Windingenieurwesen angewendet. Die Windsimulationen enthalten Unsicherheiten und der Entwurf muss diese Unsicherheiten berücksichtigen, um Strukturen im sicheren Bereich zu entwerfen. Die Anwendung der Unsicherheitsquantifizierung auf die numerische Simulation im Windingenieurwesen ist aufgrund der Rechenkosten eine Herausforderung. Um die Gesamtberechnungskosten zu reduzieren, wird in dieser Arbeit das Multi-Fidelity Framework auf die Non-Intrusive Polynomial Chaos Methode angewendet. Das Multi-Fidelity Framework wurde auf Computational Fluid Dynamics Simulationen zum Zweck der Optimierung und nicht zur statistischen Bewertung von Entwurfskandidaten angewandt. Im Windingenieurwesen wurden bisher vor allem High-Fidelity Modelle entwicklt, ohne den Multi-Fidelity Framework zu berücksichtigen. In dieser Arbeit wird MF-NIPC zum ersten Mal auf Probleme des rechnergestützten Windingenieurwisens angewandt.
Um die MF-NIPC zu demonstrieren, werden zwei bekannte Benchmark Probleme untersucht, nämlich: das BARC-Problem (Benchmark on the Aerodynamics of a Rectangular 5:1 Cylinder) und das Silsoe 6m Würfelproblem. Die rechteckige Form des BARC Problems spielt eine wichtige Rolle für den Entwurf im Bauwesen. Die Krümmung des rechteckigen Zylinders und der Anströmwinkel werden als Eingangsunsicherheiten betrachtet. Durch den Vergleich der Wahrscheinlichkeitsdichtefunktion, die aus den verschiedenen Modellen gewonnen wurde, konnte festgestellt werden, dass das Multi-Fidelity Modell die Genauigkeit der Unsicherheitsanalyse erhöht. Anschließend wurden die Ergebnisse von MF-NIPC mit den experimentellen Ergebnissen verglichen. Es zeigt sich, dass die Ergebnisse von MF-NIPC besser mit den experimentellen Daten übereinstimmen als die deterministische Simulation, die mit dem Mittelwert der Eingangs-Zufallsvariablen ausgewertet wird.
Das Silsoe 6m Würfelproblem stellt einen Flachbau dar, der den Problemen der natürlichen Windanströmung ausgesetzt ist. Die Referenzgeschwindigkeit und die Windrichtungen werden als Eingangsunsicherheiten betrachtet. Das Multi-Fidelity Modell zeigt eine Verbesserung der Genauigkeit im Vergleich zum Single-Fidelity-Modell, und die Rechenkosten werden erheblich reduziert. In Bezug auf die Lage des minimalen Sogs auf dem Dach zeigt die Multi-Fidelity-Analyse im Vergleich mit der deterministischen Simulationen, besser Übereinstimmung mit den Ergebnissen der Großversuche.

Abstract

In this thesis the Multi-Fidelity Non-Intrusive Polynomial Chaos method (MF-NIPC) is applied to computational wind engineering problems. The computational wind engineering simulations contain uncertainties and the design must account for these uncertainties to design structures within the safe range. It is challenging to apply the uncertainty quantification to computational wind engineering problems due to computational cost. In order to reduce total computational cost, the multi-fidelity framework is coupled with the Non-Intrusive Polynomial Chaos method in this thesis. The multi-fidelity framework has been applied to Computational Fluid Dynamics simulations for the purpose of optimization, rather than for the statistical assessment of candidate design. In computational wind engineering it has been rather focused on developing high-fidelity model and the multi-fidelity framework has not yet been considered. In this thesis MF-NIPC is applied to computational wind engineering problems for the first time.

In order to demonstrate MF-NIPC, two well-documented benchmark cases are studied, namely: the Benchmark on the Aerodynamics of a Rectangular 5:1 Cylinder (BARC) problem and a flow around the Silsoe 6m cube problem. The rectangular shape used in BARC plays an important role for civil engineering design. The curvature of the cylinder and the angle of attack are considered as input uncertainties for the purpose of validation to the experimental data. By comparing the probability density function obtained from the multi-fidelity model and the single-fidelity model, we observed that the multi-fidelity model increases the accuracy of the uncertainty analysis. Then the results of MF-NIPC was compared with the experimental results. It is shown that the results of MF-NIPC is more compatible to the experimental data than the deterministic simulation evaluated at the mean value of the input random variables.

The Silsoe 6m cube problem represents a low-rise building subjected to the natural wind inflow problems. The architectural structures are located in the atmospheric boundary layer and the inflow is affected by ground surface. The reference velocity and the wind directions are considered as input uncertainties. The multi-fidelity model shows the accuracy improvement compared to the single-fidelity model and the total computational cost is significantly reduced. In terms of the location of the minimum suction on the roof, the multi-fidelity analysis shows more compatible results to the full-scale observation than the deterministic simulations.

Acknowledgements

Throughout the writing of this dissertation I have received a great deal of support and assistance. First, I would like to thank Prof. Dr.-Ing. Kai-Uwe Bletzinger and Prof. Dr.-Ing. habil. Roland Wüchner for giving me a chance to pursue the doctoral degree at the Technical University of Munich. I would like to thank DAAD for funding and examiners for their effort in reviewing my thesis. I wish to acknowledge Prof. Akihiro Takahashi, Prof. Tomohide Takeyama and Dr. Katsuya Abe for their support to start the doctoral study. I would like to express my gratitude to Prof. Francesco Montomoli for giving me an opportunity to work with his team at the Imperial College London and his invaluable advice. I would like to thank Dr. Nick Pepper for his numerous support. I would like to thank my colleagues at TUM, especially Suneth Warnakulasuriya and Anoop Kodakkal, for their support and discussions. Almost half of this work had been carried out during the COVID-19 pandemic, and I would like to thank my housemates at the time of working at home, Stephanie and Leonie, for motivating and encouraging me. Finally, I wish to thank my family, especially my mother Mina, for their continuous support at every step of my life.

Mayu Sakuma
Technische Universität München
December, 2021

Contents

List of Abbreviations

ABL	Atmospheric Boundary Layer.
aPC	arbitrary Polynomial Chaos.
BARC	the Benchmark on the Aerodynamics of a Rectangular 5:1 Cylinder.
CFD	Computational Fluid Dynamics.
CWE	Computational Wind Engineering.
FEM	Finite Element Method.
FSI	Fluid Structure Interaction.
FVM	Finite Volume Method.
gPC	generalized Polynomial Chaos.
HF	high-fidelity.
LES	Large Eddy Simulation.
LF	low-fidelity.
MC	Monte Carlo.
MF-NIPC	Multi-fidelity Non-Intrusive Polynomial Chaos method.
NIPC	Non-Intrusive Polynomial Chaos methods.
PCE	Polynomial Chaos Expansion.
PDF	Probability Density Function.
QoI	Quantity of Interest.
RANS	Reynolds Averaged Navier Stokes.
RHS	Right Hand Side.
SST	Shear Stress Transport.

T.I.	Turbulence Intensity.
UQ	Uncertainty Quantification.
URANS	Unsteady Reynolds Averaged Navier Stokes.
V&V	Verification & Validation.
VMS	Variational Multiscale method.

List of Symbols

(D_x, D_y, D_z) computational domain size components.

(I_u, I_v, I_w) turbulence intensity components.

$(\cdot)^n$ value at n th time step.

$(\cdot)_H$ large scale variable.

$(\cdot)_S$ small scale variable.

$(\cdot)_\delta$ value of discrepancy between value of a high-fidelity model and value of a low-fidelity model.

$(\cdot)_h$ value of the high-fidelity model.

$(\cdot)_l$ value of the low-fidelity model.

(u, v, w) velocity components.

B chord length of a rectangular cylinder.

C_μ empilicaly determined constant defined in Eq. (3.18).

C_d drag coefficient.

C_f skin friction coefficient.

C_l lift coefficient.

C_p pressure coefficient.

$D_{i_1,\ldots,i_s}$ partial variance.

D thickness of a rectangular cylinder.

$E(k)$ von Karman energy spectrum.

$E[\cdot]$ expected value.

F_d drag force.

F_l lift force.

H height of the Silsoe cube.

J Jacobian matrix.

M Henkel matrix.

N^a shape function.

P total number of terms for n dimensional and p th order polynomial chaos expansion defined by Eq. (3.37).

$Q_{d,k}$ Smolyak quadrature rule with level k for dimension d.

Q_{q_j} Gauss quadrature rule for a variable X_j.

Re Reynolds number.

R upper triangular matrix.

$S_i(f)$ turbulent energy spectrum.

S_t Strouhal number.

$S_{i_1,\ldots,i_s}$ Sobol's indices for $1 \leq i_1 < \cdots < i_s \leq n, s = 1, \ldots, n$ (n:number of random variables).

U_∞ freestream velocity.

Y_p p th order polynomial chaos estimation of Y.

Γ_D Dirichlet boundary.

Γ_N Neumann boundary.

Ω whole computational domain.

β_{LT} dimensionless eddy lifetime.

ϵ turbulent dissipation rate.

κ von Karman constant.

$\langle \cdot \rangle$ time averaged value.

$\mathbb{R}^n$ n dimensional vector space.

$\mathbf{L}^{(i)}$ multi variate Lagrange polynomial to interpolate i th collocation point defined in Eq. (3.43).

$\mathbf{R}^m, R^c$ the strong form residuals defined in Eq. (3.12).

$\mathbf{U}$ time averaged velocity vector.

$\mathbf{X}^*$ bootstrap samples of random variables X.

$\mathbf{X}$ input random variables.

$\mathbf{\Psi}(\beta_{LT})$ turbulence spectrum tensor defined in Mann [86].

$\mathbf{\Psi}(\mathbf{X})$ multivariate orthogonal polynomial.

σ stress tensor.

$\mathbf{a}$ polynomial chaos expansion coefficient.

$\mathbf{f}$ external force.

$\mathbf{l}^{(i)}$ one dimensional Lagrange polynomial to interpolate i th collocation point defined in Eq. (3.43).

$\mathbf{u}'$ time fluctuating component of velocity vector.

$\mathbf{u}_0$ initial velocity vector.

$\mathbf{u}_D$ inlet velocity vector.

$\mathbf{u}$ fluid velocity vector.

$\mathbf{w}$ velocity test function.

μ_T Eddy viscosity.

μ fluid viscosity.

ν_T kinematic Eddy viscosity.

ω turbulent specific energy dissipation rate.

$\overline{(\cdot)}$ time averaged value.

$\partial\Omega$ boundary of computational domain.

ρ fluid density.

$\sigma_{(\cdot)}$ time standard deviation value.

$\tau_u, \tau_p, \xi_h, \delta_h$ the stabilization parameters defined in Eq. (3.12).

τ_w shear stress at wall.

$\tilde{C_p}$ time standard deviation of pressure coefficient.

k turbulence kinetic energy.

p_∞ reference pressure.

p_{ESG} pressure calculated by the equivalent-steady gust model defined in Eq. (5.4).

q dynamic pressure defined in Eq.(5.2).

r curvature radius.

$t - avr(\cdot)$ time averaged value.

$t - std(\cdot)$ time standard deviation value.

t^* non dimensional time.

u^+ dimensionless velocity.

u_τ friction velocity.

w_q pressure test function.

y^+ dimensionless wall distance.

z_* roughness parameter used for generated fluctuating inlet wind by WindGen.

z_0 roughness length for the logarithmic profile of mean velocity defined in Eq. (5.6).

$||\cdot||$ norm.

Chapter 1

Introduction

Thanks to the improvement of computational power, Computational Wind Engineering (CWE) has been rapidly developed recently. In addition to development of deterministic simulations, Uncertainty Quantification (UQ) has been increasingly receiving attention in finance and mechanical engineering field. While the improvement of CWE, wind engineering design is still relying heavily on wind tunnel tests. In this chapter first the role of Computational Fluid Dynamics (CFD) simulations in design codes are explained to review the role of CWE in wind engineering design. Afterwards, it is introduced how UQ can help wind engineering designs from the aspect of Verification & Validation (V&V) and the climate change adaptation design in section 1.2. Finally, the objective of this thesis will be explained in section 1.3 and the outline of the thesis will be introduced in section 1.4.

1.1 Roles of Computational Fluid Dynamics simulations in Wind Engineering design

According to Blocken [15] CWE is defined as "the use of CFD for wind engineering applications" and wind engineering is defined as "the rational treatment of interactions between wind in the atmospheric boundary layer and man and his works on the surface of Earth". CWE can be roughly divided to two fields, namely: Environmental Wind Engineering and Structural Wind Engineering. Problems included in the Environmental Wind Engineering are, for example, pedestrian level urban flow for human comfort problems (Mochida et al. [96]) and pollutant dispersion problems (Sabatino et al. [132]), while the Structural Wind Engineering are dealing with wind lads on structures (Kareem [74]) and wind-structure interaction problems (Tamura [152]). This thesis focuses on the Structural Wind Engineering problems. The comprehensive

explanation of the Environmental Wind Engineering problems may be found in Blocken [15]. Recently CFD has been applied to both Environmental Wind Engineering Problems and Structural Wind Engineering problems. In the Environmental Wind Engineering the advantage of CFD is what is easier to make graphic presentation of wind flow field compared to the wind tunnel tests (Stathopoulos et al. [144]). Stathopoulos et al. [144] and Phillips et al. [114] discussed the potential of CFD usage as an alternative to the wind tunnel tests in the Environmental Wind Engineering. As examples of application of CFD in the Environmental Wind Engineering problems Stathopoulos et al. [144] compared CFD results of Reynolds Averaged Navier Stokes (RANS) model and wind tunnel results. They found that CFD results and wind tunnel results have significant discrepancy in a case of highly complex re-circulation flow region. Phillips et al. [114] introduces several turbulence models for CFD and listed three difficulties to apply CFD to the pedestrian problems, namely: inlet boundary condition, maintaining the velocity and turbulence profiles into the domain and the prediction of aerodynamic flow around bluff bodies. Compared to Environmental Wind Engineering problems, there are fewer research papers concerning validation of CFD simulations for the Structural Wind Engineering problems. It may be because for the Structural Wind Engineering problems the extreme pressure coefficient is also important and it is more difficult to reduce variation both in wind tunnel tests and CFD simulations, while in the Environmental Wind Engineering problems usually only the mean value is in interest. This fact has made it more difficult to carry out validation for the Structural Wind Engineering problems. As results of this aspect, most of design codes still do not approve to determine wind load depending on CFD results alone. According to most of existing design codes it is required to carry out wind tunnel tests in order to determine wind loads. In this section, design codes from the European Committee for Standardization, the American Society of Civil Engineers and the Architectural Institute of Japan are compared from the standpoint of CFD for structural design. In addition, several best practice guidelines will also be introduced later in this section. The best practice guidelines have been published, so that CFD simulations give reliable results regardless of the experience and skill of simulation engineers.

Design code: the European Committee for Standardization

In the European Code (EN 1991-1-4:2005) by European Committee for standardization [46] it has been indicated that the design process may be assisted by testing and measurements as:

1. In supplement to calculations wind tunnel tests and proven and/or properly validated numerical methods may be used to obtain load and response information, using appropriate models of the structure and of the natural wind.

2. Load and response information and terrain parameters may be obtained from appropriate full scale data.

As the European code is followed by the national annex, it indicates that "The National Annex may give guidance on design assisted by testing and measurements". The German annex (Deutsches Institut für Normung e. V. [36]) mentions usage of wind tunnel tests results for building design, however there is no description about usage of CFD results. It is to say that CFD results alone still cannot be used for the wind engineering design in the German design code.

Design code: the American Society of Civil Engineers

In the American Society of Civil Engineers Standard American Society of Civil Engineers [6] the allowed procedure for the wind load calculation should be one of the following methods.

1. Method 1 - Simplified Procedure as specified in Section 6.4 for buildings meeting the requirements specified therein
2. Method 2 - Analytical Procedure as specified in Section 6.5 for buildings meeting the requirements specified therein
3. Method 3 - Wind Tunnel Procedure as specified in Section 6.6

Method 1 is applied to relatively simple structures, to which the along wind effect can be ignored. Method 2 is applied to more complicated structures than one in Method 1, and the along wind effect is considered. Method 3 is applied to the most complicated structures, and wind tunnel tests should be carried out. Thus CFD has not been defined yet as a method to determine the wind load as is the case with the European code.

Design code: the Architectural Institute of Japan (AIJ)

In Japan the wind load should be decided based on the building standard law. For buildings which exceed coverage of the building standard law, such as high rise buildings and buildings with special shape, the AIJ Recommendation for Loads on Buildings Architectural Institute of Japan [10] is applied to determine the wind load. In 2007 the Guidebook of Recommendations for Loads on Buildings 2 – Wind induced Response and Load Estimation/Practical Guide of CFD for Wind Resistant Designs Architectural Institute of Japan [11] is published, and since then for the exceptional buildings it is allowed to determine wind load only by CFD. The procedure to determine the wind load is illustrated in Figure 1.1. The wind load determined by CFD results should pass the performance assessment by the ministry of Land, Infrastructure, Transport and Tourism. In order to confirm reliability of CFD simulations as a tool to determin wind loads in designing process, Tamura et al. [153] carried out validations by comparing wind tunnel tests and CFD simulations for two types of tall building and compared results. This research is the base of the Guidebook of Recommendations for Loads on Buildings 2 – Wind induced Response and Load Estimation/Practical Guide of CFD for Wind Resistant Designs Architectural Institute of Japan [11]. In Tamura et al. [153],

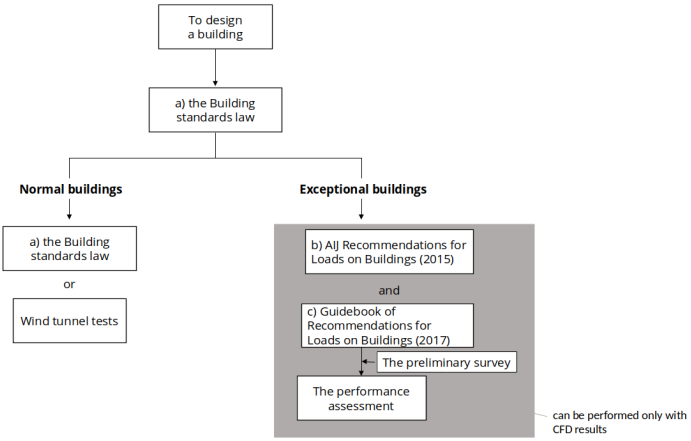

Figure 1.1: The procedure of determining wind load in Japan

in order to consider variation included in the wind tunnel tests and CFD simulations, three wind tunnel tests and seven CFD simulations has been carried out. It shows that the wind tunnel results and CFD results agreed very well not only about time averaged pressure coefficient but also about unsteady pressure coefficients, such as maximum- and minimum peak, and it concluded that CFD simulations predict wind load as same level as wind tunnel tests do. It should be noted that CFD simulations used in Tamura et al. [153] are all relatively large in practical point of view, such as 30 to 200 million cells. Tamura et al. [153] also pointed out that it is critical to investigate the minimum requirement of CFD simulations to obtain adequate accuracy with practically affordable computational power. I would like to acknowledge Prof. Tetsuro Tamura for providing information.

Best practice guidelines of CFD simulations

Since accuracy of CFD simulations heavily depends on skills of engineers, several best practice guidelines have been published (Blocken et al. [16]). A primary best practice guideline was published by European Research Community on Flow, Turbulence and Combustion (ERCOFTAC, Casey et al. [25]). This best practice guideline covers only RANS, and focuses more on mechanical engineering applications, as application examples are transonic airfoil, engine valve and so on. For CWE problems European Cooperation in Science and Technology (COST) published two best practice guidelines namely: “Recommendations on the use of CFD in wind engineering”(Franke et al. [51]) and “The COST 732 Best Practice Guideline for CFD simulation of flows in the urban environment: a summary”(Franke et al. [52]). Franke et al. [51] is published as a contribution of the European COST Action C14.

This best practice guide focuses on application of CFD to CWE problems, and mentions about flow in Atmospheric Boundary Layer (ABL). As is the case with Casey et al. [25], Franke et al. [51] focuses on RANS as a turbulence model. The other best practice guideline from COST, Franke et al. [52], is published as an extension of Franke et al. [51], and it is published as a contribution of the European COST Action 732. Franke et al. [52] focuses on RANS as well and it is based on previous best practice guidelines. Outside of Europe the Architectural Institute of Japan (AIJ) published a best practice guideline (Tominaga et al. [158]). Tominaga et al. [158] focuses on RANS as well, however the best practice guideline is based on result of their own benchmark cases, while the guidelines from COST is based on literature review. Tominaga et al. [158] investigated six benchmark cases, namely: single high-rise building with two different cross section, simple city block model, a high-rise building in the city model and building complexes in two different actual urban areas. Some results used for development of the guideline has been introduced in Yoshie et al. [171]. The CFD results have been compared with wind tunnel results and field measurement data. The AIJ guideline focuses on pedestrian level urban flow problems which are classified to the Environmental Wind Engineering.

1.2 Roles of Uncertainty Quantification in Computational Wind Engineering

In previous section, it has been introduced how CWE have been used in the Wind Engineering design. The aim of this research is to apply UQ to CWE problems. In this section two example cases are introduced, in which UQ for CWE may help design procedure.

1.2.1 Validation

Before introducing application of UQ to the validation let us look at basic terminology of Verification and Validation (V&V), since often "verification" and "validation" are used ambiguously. The terminology of V&V has been often discussed in several committees. Here the history of the terminology is briefly introduced. Along with improvement of numerical analysis methodologies and computational power, it has been sought how to assure accuracy of CFD simulations. For this purpose V&V plays a key role. The concept of V&V is illustrated by Schlesinger [136] as in Figure 1.2.

Now let us look at definitions of term *Verification* and *Validation*. In 1987 the American Nuclear Society defined V&V as (Roache et al. [129]):

- Verification: The process of evaluating the products of a software development phase to provide assurance that they meet the requirements defined for them by the previous phase
- Validation: The process of testing a computer program and evaluating the results to ensure compliance with specific requirements.

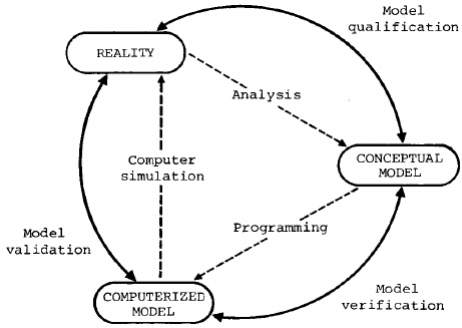

Figure 1.2: Illustration of Verification and Validation process
Schlesinger [136]

This definition had been criticized due to its low utility (Oberkampf [104]). Bradley [17] introduced the following definition determined by an ad hoc committee formed by the National Aeronautics and Space Administration (NASA). It is noted that definition of the verification was not given in Bradley [17].

- Validation: Detailed surface-and-flow-field comparisons with experimental data to verify the code's ability to accurately model the critical physics of the flow. Validation can occur only when the accuracy and limitations of the experimental data are known and thoroughly understood and when the accuracy and limitations of the code's numerical algorithms, grid-density effects, and physical basis are equally known and understood over a range of specified parameters.

- Calibration: The comparison of CFD code results with experimental data for realistic geometries that are similar to the ones of design interest, made in order to provide a measure of the code's capability to predict specific parameters that are of importance to the design objectives without necessarily verifying that all the features of the flow are correctly modeled.

After these definitions were published Roache [128] and Oberkampf [104] reviewed the terminologies and made their own definitions. Oberkampf [104] defined verification and calibration as:

- Code Verification Activities: Activities, either experimental, analytical, or numerical, that build confidence in a code's ability to predict well-known physics or a specified mathematical model of physics.

- Code Calibration Activities: Activities, either experimental, analytical, or numerical, that build confidence in a code's ability to predict flow variables when the physics is incompletely or poorly known.

Oberkampf [104] did not make definition of validation, while validation is higher requirement for the code which may be done between the code verification and the code calibration. Roache [128] made simple definition for V&V as:

- Verification: solving the equations right
- Validation: solving the right equations.

In 1998 the American Institute of Aeronautics and Astronautics (AIAA) make a following definition focusing on CFD simulations (*Guide for the Verification and Validation of Computational Fluid Dynamics Simulations* [64]).

- Verification: The process of determining that a model implementation accurately represents the developer's conceptual description of the model and the solution to the model.
- Validation: The process of determining the degree to which a model is an accurate representation of the real world from the perspective of the intended uses of the model.

The detailed explanation of V&V may be found in Oberkampf et al. [106].
Now let us apply the introduced V&V procedure to CWE problems. In Fig. 1.3 the V&V process is illustrated for CWE problems. In CWE, the conceptual model is Navier-Stokes equations, additional turbulence modelings and simplification of structure geometry and surrounding buildings. If structures are flexible, such as bridge decks and high-rise buildings, Fluid Structure Interaction (FSI) models may be used for the conceptual models. The computational models are software such as KratosMultiphysics (Ferrándiz et al. [48]) and OpenFOAM (Weller et al. [160]), that are implemented to solve equations defined in the conceptual models. The verification is to confirm whether the software is solving the Navier-Stokes equations and additional turbulence equations right and implemented correctly, including eliminating bugs. The verification of CFD simulations in KratosMultiphysics is carried out in Abodonya [2].
UQ may be used in the validation process. Considering comparisons between reality and the computational model, it is not possible to avoid all uncertainties in reality or wind tunnel tests, such as manufacturing error and inflow velocities. The classification of the uncertainties will be introduced in detail in the following chapter. UQ is used for taking these uncertainties account during the validation process. In this thesis UQ will be applied for validation of two benchmark problems in CWE, and the detail will be explained in greater detail in the following chapter.

1.2.2 Climate Change Adaptation Design

It has been known that changing climate will cause significant damage to infrastructures in future. Considering that infrastructures and buildings have long in-service period, it becomes necessary to take into account the future climate change impact for design. The climate change adaptation design has

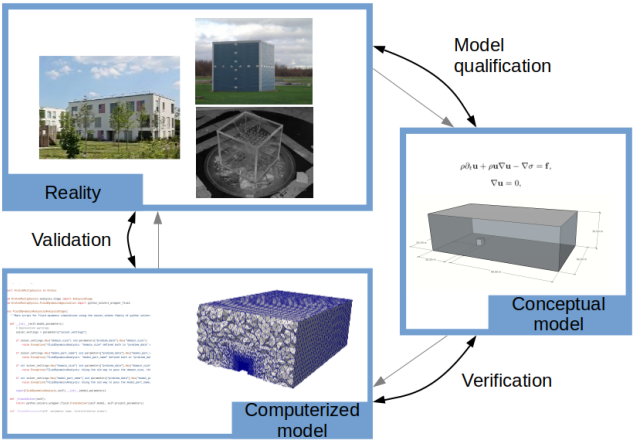

Figure 1.3: Illustration of Verification and Validation process in CWE. Pictures are taken from *muenchen.de Das offizielle Stadtportal* [98], Richards et al. [124] and Richards et al. [120]

been receiving increasing attention, as a methodology to take the climate change in account to the civil engineering design. According to "Climate change 2007: The physical science basis" [28], the climate change adaptation is defined as: *initiatives and measures to reduce the vulnerability of natural and human systems against actual or expected climate change effects.* Connor et al. [30] introduces a whole climate change adaptation process. Here we focus on roles of CWE in the climate change adaptation design. As mentioned in previous section 1.1, the role of CFD in the design code is to determine wind loads according to input extreme wind speed. The difference between climate change adaptation design and the conventional design is that in the climate change adaptation design the design wind speed is changed depending on the climate change scenarios. While in the conventional design the extreme wind speed has been decided only by historical value, in the climate adaptation design the extreme wind speed is decided depending on the climate change scenarios. Since changing climate includes a lot of uncertainties, there are many different scenarios, for example "Climate change 2007: The physical science basis" [28] introduces 40 different climate change scenarios. Usually one climate change scenario is chosen and from the greenhouse gas suggested by the climate change scenario the extreme wind speed is calculated using projection methods (Jeong et al. [72]). Jeong et al. [72] calculated the extreme wind using a projection method Canadian Regional Climate Model (CRCM5, Côté et al. [32]) using two different climate change scenarios, and pointed out that the projected extreme wind is quite dependant on the climate scenarios.

For architectural designs the climate change adaptation has been considered

especially for the Environmental Wind Engineering problems, in order to investigate thermal comfort and energy usage caused by temperature change (Stagrum et al. [143]). Hooff et al. [66] compares effect of six passive climate change adaptation measures with respect to overheating hours and the temperature increase. Kleerekoper et al. [77] compares different cooling measures. These studies are neither using specific climate change scenarios nor the probabilistic theories. In the Structural Wind Engineering, Stewart et al. [146] investigates cost of climate adaptation measure, however in this research CFD simulations are not used for calculating the vulnerability of infrastructures and only statistical models are used to determine the relationship between vulnerability of the structure and the peak gust wind speed.
Thus, CFD simulations with UQ have not yet been applied to the climate change adaptation design in the structural wind engineering, though many works in the literature are aware of the uncertainties included in the climate change scenarios(e.g. Jeong et al. [72]). In order to take the uncertainties account into the climate change adaptation design, the probability density function (PDF) of the extreme wind should be given for each climate change scenario. There are two challenges to get the PDF of the extreme wind, namely:

1. The climate change scenario should indicate the uncertainty quantitatively.
2. The projection should quantify the uncertainty of the climate change scenario.

After having PDF of the extreme wind, stochastic wind load to buildings caused by the wind can be simulated using UQ methodologies, which will be introduced in this thesis, and it may help developing the design code considering climate change.

1.3 Objectives

The main topic of this thesis is to investigate the applicability of UQ to CWE problems with practically affordable computational costs. As mentioned in section 1.1, the CFD simulations have taken increasingly bigger role in architectural design, and in future UQ will take more important role when the uncertainties of the climate change should be necessarily considered. In addition, UQ is a very useful tool in validation. UQ has not yet been applied to CWE problems, Because UQ requires several runs of deterministic simulations and a deterministic simulation of CWE is already computationally very expensive. In order to reduce total computational cost, in this thesis the multi-fidelity framework is applied to UQ for the first time for CWE problems. For CWE problems it has been more focused on improving high-fidelity simulations, while the multi-fidelity framework has not been considered. To carry out deterministic CFD simulations, Finite Element Method (FEM) based software is used. In order to carry out UQ taking geometry as an input random variables, it is necessary to express detailed shape of the structure.

Since the FEM uses tetrahedron/triangle meshes which can express geometry in detail, the FEM based method has great advantage in terms of carrying out UQ. The FEM based CFD is getting popular especially for Fluid-Structure Interaction simulations, however there are not yet many research in CWE. In this thesis MF-NIPC with FEM based CFD simulations is applied to two well-known benchmark cases in CWE, namely: the Benchmark on the Aerodynamics of a Rectangular 5:1 Cylinder (BARC) and the Silsoe 6m cube problems. For developing the multi-fidelity framework Large Eddy Simulation (LES) is used as a high-fidelity model and the Unsteady Reynolds Averaged Navier-Stokes (URANS) simulations is used as a low-fidelity model. The accuracy of the multi-fidelity model is investigated by comparing PDF of different models and the results of MF-NIPC is validated with experimental data.

1.4 Outline of this document

The remaining chapters are organized as follows.
In Chapter 2 the literature related to the multi-fidelity Non-Intrusive Polynomial Chaos methods for CWE problems are reviewed. First uncertainties in CWE problems are classified, and then literature about UQ for wind engineering problems and CFD problems are reviewed. Here the CFD problems include not only the wind engineering problems, but also mechanical engineering problems. Then the multi-fidelity framework used for CFD problems are reviewed and appropriate multi-fidelity framework for CWE problems is discussed.
In Chapter 3, first the theory of CFD simulations are explained then the Non-Intrusive Polynomial Chaos methods are introduced. Afterwards the Non-Intrusive Polynomial Chaos is expanded to the multi-fidelity framework.
In Chapter 4 the introduced MF-NIPC is applied to a homogeneous inflow CWE problem. As a target problem, flow around a rectangular problem is chosen which is well studied in CWE field both using CFD simulations and wind tunnel tests.
In Chapter 5 the introduced MF-NIPC is applied to a natural wind inflow problem. As a target problem, Silsoe cube problem is chosen, for which full-scale observation data is available.
Finally in Chapter 6 we summarize the work.

Chapter 2

Multi-fidelity Uncertainty Quantification for Computational Wind Engineering problems (Literature review)

In this chapter literature related to multi-fidelity UQ for CWE problems are reviewed. First section is a literature review about UQ without the multi-fidelity framework. The literature that carried out UQ for CWE and CFD problems are reviewed. Then, literature that applied multi-fidelity framework are reviewed. In this section, not only application of the multi-fidelity framework to UQ but also application to other problems such as optimisations are reviewed, in order to overview widely the multi-fidelity framework in CFD problems. Finally existing CFD models, which have different fidelity, are reviewed and suitable multi-fidelity framework for CWE problems are discussed.

2.1 Uncertainty Quantification in Computational Wind Engineering

2.1.1 Classification of uncertainties in Computational Wind Engineering

Generally uncertainties can be classified as either aleatory uncertainty or epistemic uncertainty. According to Oberkampf et al. [107], these uncertainties are defined as:

- Aleatory uncertainty: the inherent variation associated with the physical system or environment being considered

- Epistemic uncertainty: a cause of non-deterministic behavior derives from some level of ignorance or lack of knowledge about the system or environment

Recently it has been also said that uncertainties cannot always be classified to these two types of uncertainties and the classification is not always necessary, however this classification has been often used for UQ and it helps readers to understand the characteristics of uncertainties. In Fig. 2.1, possible uncertainties in CWE are listed up and classified to the aleatory- and epistemic uncertainty. The inflow wind is the significant aleatory uncertainty in the CWE, and the parameters induced from CFD solver settings and modelings are epistemic uncertainties. Geometry can be both aleatoric- and epistemic uncertainties. For example, variation of geometry might happen during manufacturing process, and in this case it is an aleatoric uncertainty. On the other hand, we basically cannot model whole detailed geometry of structures, such as balcony and plants, and in this case the uncertainty can be classified as epistemic uncertainty. In this thesis we focus only on the aleatory uncertainties. This is because, to apply the multi-fidelity framework the input uncertainties should be consistent in low- and high fidelity models. The epistemic uncertainties are often model dependent and therefore difficult to be considered in the multi-fidelity framework. In this thesis only literature review is carried out for the epistemic uncertainties.

2.1.2 Uncertainty Quantification for wind engineering problems

In this section literature, which deal with uncertainties for wind engineering problems, are reviewed. It should be noted that not all literature are using CFD simulations, and the deterministic models may be introduced below. Literature for UQ specially in CFD problems, which are not dealing with wind problems but mechanical and other fluid problems, will be introduced in the following section 2.1.3. The literature for UQ in wind engineering can be roughly categorized to:

- Meteorological problems

- Human comfort problems

- Structural problems.

Meteorological problems In the meteorological field, Sochala et al. [141] investigated the uncertainty of peak water level evaluation, considering storm characteristic and empirical constitutive laws as input uncertainties. As a deterministic simulation the storm surge model is used and as a UQ methodology the polynomial chaos method is used. Ak et al. [5] investigate the short term wind speed time series, considering hourly and dairy wind speed as

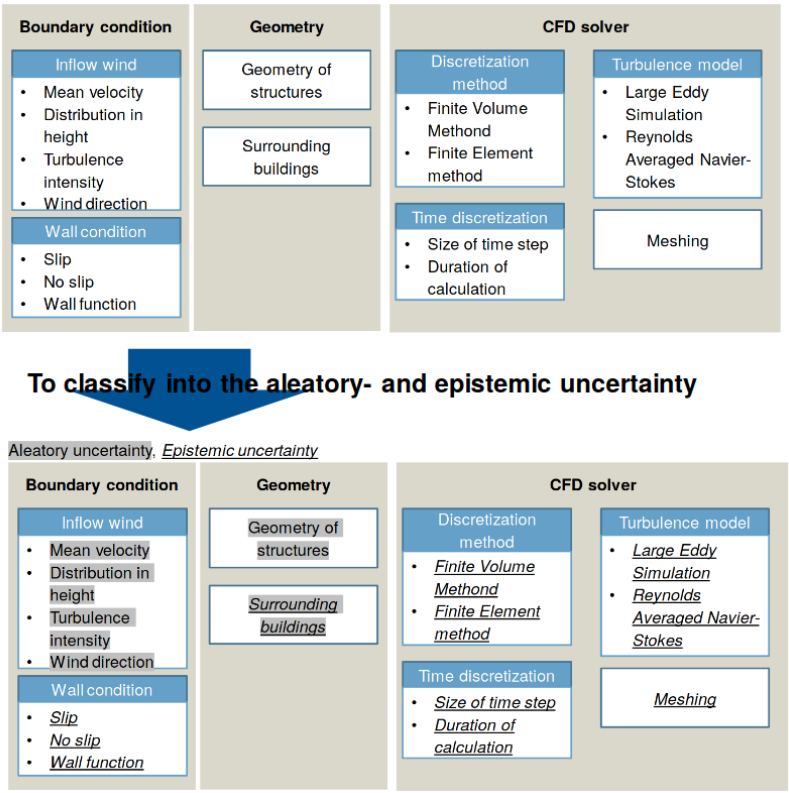

Figure 2.1: Uncertainties in CWE

input uncertainties. As a deterministic model, a neural network is used and as UQ methodology an interval analysis is performed. Many researches in the meteorological field are motivated by estimating wind energy production, for example, Du et al. [39] investigate uncertainties of the available transmission capabilities of existing-and future wind firm, considering wind time series data as input uncertainties. The available transfer capability assessment is used as a deterministic model and the Monte Carlo (MC) methods are used as a UQ methodology. Jin et al. [73] investigate the short term wind speed at hub height at a wind farm. Jin et al. [73] uses combination of the Weather Research Forecasting (WRF) model and CFD model as a deterministic model, and consider the inlet wind distribution and turbulence model parameter in the CFD model as input uncertainties. The polynomial chaos methods are used as UQ methodologies. For the meteorological problems, not only CFD

simulations but also various physical models have been used as deterministic simulations.

Human comfort problems For the human comfort problems, Garcıéa-Sánchez et al. [54] carried out UQ for wind field simulations using RANS as a deterministic model, and stochastic results are compared with measured data. Wind speed and wind direction at a reference height and aerodynamic roughness in the logarithmic velocity inlet profile are considered as input random variables. Quantity of Interest (QoI)s are velocity magnitude and direction at field measurement stations, and Non-Intrusive Polynomial Chaos methods (NIPC) was used as an UQ methodology. Gorlé et al. [62] considers both aleatoric- and epistemic uncertainties. RANS was used for deterministic simulations and mean wind velocity and wind directions are considered as QoIs. Inflow velocity parameters are considered as aleatoric uncertainties, and NIPC is used to propagate these uncertainties. The epistemic uncertainties are considered by introducing perturbation in the Reynolds stress. To propagate the epistemic uncertainties, the interval method was used. Garcıéa-Sánchez et al. [55] carried out UQ for pollutant dispersion problems in urban environment using RANS as a deterministic simulations. Velocity magnitude and direction and a terrain roughness length are considered as input random variables and these Probability Density Function (PDF)s were derived from measurement data. QoIs are wind magnitude and direction and non-dimensional concentration, and these are compared with measured data. NIPC method is used as an UQ methodology. Garcıéa-Sánchez et al. [53] investigated uncertainties, which occur when a meso-scale model and micro-scale model are coupled. Here the meso-scale model is numerical weather prediction models and the micro-scale model is CFD simulations. UQ was carried out for the micro-scale model considering roughness length, wind direction and magnitude as input random variables. PDF of roughness length is determined from empirical data and PDF of wind direction and magnitude are determined from the meso-scale simulation. Gorlé et al. [61] investigates the epistemic uncertainty in RANS by introducing perturbation in the Reynolds stress. This methodology is applied to the separated flow problems such as flow over periodic wavy wall problems and a three dimensional hill problem. Margheri et al. [90] carried out UQ for high-fidelity simulations using the anchored-ANOVA and POD/Kriging methods. The anchored-ANOVA method is a sensitivity analysis and it is used to reduce the UQ dimension space. The combination of these methods makes it possible to reduce the number of required deterministic simulations and UQ was carried out for large simulations, such as pedestrian wind comfort study in a full scale urban area, using LES as a deterministic simulation. Sun et al. [150] carried out UQ for building energy assessment problems. Building energy simulations are used as a deterministic simulations. Before carrying out the building energy simulations, lower fidelity models were used to determine input random variables. Sun et al. [149] carried out UQ for single-sided ventilation rate problems for a building. RANS are used for a deterministic simulation, and wind speed, incident angle and ground roughness are considered as input random variables. QoI is the ventilation rate and generalized Polynomial Chaos (gPC) method is used as a

UQ methodology. For the human comfort problems most of literature uses CFD simulations as deterministic simulations. Though not LES but RANS simulations are used, the spectral method, such as polynomial chaos methods, are used as UQ methodologies. It follows that if we want to apply UQ for LES simulations, which has rather high computational cost compared to RANS, it is necessary to consider auxiliary framework to reduce total computational cost for practically affordable application.

Structural problems For structural problems, several literature carried out UQ to bridge deck simulations. Bruno et al. [20] carried out UQ for a bare bridge deck with trapezoidal cross section. The section lower edge degree of sharpness and oncoming turbulence integral length scale are considered as input random variables and the aerodynamics coefficient is QoI. Time dependent RANS is used as a deterministic model and an adaptive form of the Multi-Element generalized Polynomial Chaos (aME-gPC) is used as a UQ methodology. Bruno et al. [19] carried out UQ for a flat plate by solving incompressible, unsteady and two dimensional arbitrary Lagrangian-Eulerian version of Navier-Stokes equation. Incoming mean flow velocity is considered as an input random variable, and steady force, friction coefficient and velocity in the wake and flutter are considered as QoIs. Multi-Element gPC is used as an UQ methodology. Canuto et al. [23] carried out UQ for the Sunshine Skyway Bridge deck using two dimensional RANS as a deterministic model. Curvature radius is considered as an input random variable. PDF of the curvature radius is expressed by Weibul distribution and the truncation of the Weibul distribution was changed to find proper PDF. QoIs are time averaged lift coefficient and the Strouhal number. NIPC is used as an UQ methodology. As a benchmark problem for bridge decks and other civil engineering structures, a Benchmark on the Aerodynamics of a Rectangular 5:1 Cylinder (BARC) has been widely investigated (Bruno et al. [22]). There are several literature about UQ for the BARC problem, for example, Siconolfi et al. [139] carried out UQ for the BARC. The more detailed review of BARC and UQ applied for BARC will be found in the following chapter.
Until now researches for part of civil engineering structures are introduced and now let us look at researches for entire buildings. Lamberti et al. [79] carried out UQ for a high-rise building model using RANS as a deterministic model. Reference velocity, roughness length and angle of misalignment are considered as input random variables and QoI is wind pressure coefficient of a high-rise building. The NIPC method is used as a UQ methodology and also model uncertainties have been considered by introducing perturbation in the Reynolds stress. Some researches focus more on dynamic structural response for high rise buildings, for example, UQ for structural problems are often carried out for the purpose of Performance-Based Wind Engineering (PBWE) design. PBWE consider the whole range of performances of buildings in a probabilistic context and throughout the whole life-cycle of the structure. Decision makers will decide location and design of the structure depending on the structural risk which is calculated considering uncertainties in every phase. The detailed explanation of the PBWE may be found in Ciampoli et al. [27]. Chuang et al. [26] applied NIPC to the multi degree of freedom structure

excitation problem. Structural variables, such as mass and damping, are considered as input random variables. Li et al. [81] introduced a framework, where PBWE is embedded into Risk Design Optimization (RDO), in order to make complex decision making relatively easy multi-attribute decision making process. As an example, CAARC benchmark case Thordal et al. [157] was considered. Intensity measure of wind, structural parameter and resistance are consdiered as input random variables and the micro multi-objective particele swarm optimization (Micro-MOPSO) was used as UQ methodology. Cui et al. [34] carried out deterministic simulations using GPU and applied Monte Carlo methods. In summary most of literature except Cui et al. [34] uses the spectral methods as is the same with the human comfort problems. Though for the structural problems for architectural design LES simulation has been more often used than for the human comfort problems, most of literature uses RANS simulations as deterministic simulations. From this fact it can be easily imagine that it is practically very difficult to carry out UQ for LES simulations. In addition to architectural problems, there has been also increasing number of literature which carried out UQ for the wind turbine problems. For example, Murcia et al. [99] carried out UQ for DTU 10 MW reference wind turbine. Compared to architectural wind engineering problems, there are various deterministic simulations are used for wind turbine simulations.

2.1.3 Uncertainty Quantification for CFD problems

UQ has been increasingly popular for CFD problems in last decades. Walters et al. [159] introduces probabilistic methods, such as Monte Carlo (MC) method, moment method and Polynomial Chaos (PC) method and non-probabilistic methods, such as interval analysis. A summary of probabilistic and non-probabilistic method for UQ may be found in Walters et al. [159]. Though it is not focused on in this thesis, in CFD simulations, it has been known that the epistemic uncertainties also play an important role. Oberkampf et al. [105] summarizes nature of the epistemic uncertainties in CFD simulations and applied a evidence theory to a simple system given by an algebraic equation. In the evidence theory the input random variables are not given by PDF but by intervals and plausibility and belief are given as outputs. As an example, Ling et al. [83] investigated the epistemic uncertainty of RANS simulation using machine leaning algorithm. The data base for machine learning is trained by results of direct numerical simulations or LES results, and region with high model uncertainties are specified. In addition aforementioned Gorlé et al. [61] and Gorlé et al. [62] investigated also the epistemic uncertainties of RANS simulations by introducing perturbation to the Reynolds stress. The interested readers about the epistemic uncertainties are referred to those literature, and from now on we are focusing on propagating the aleatory uncertainties.

As it is observed in previous section about UQ for CWE problems, for CFD problems the spectral analysis have been widely used to reduce total computational time. In addition, most of used spectral analysis is non-intrusive to use CFD code as *black box*. The non-intrusive spectral methods will be

used in this thesis as well, the detail will follow. Here we would like to review literature which apply spectral methods to CFD simulations other than CWE applications. The major disadvantage of the spectral methods is the so-called *curse of dimensionality*, meaning that the number of required deterministic simulations increases exponentially with dimension of the input random variables. To overcome the *curse of dimensionality*, a two-step approach is often carried out in case there are large dimension of possible input random variables. The two-step approach is introduced by Loeven et al. [84] for the chaos collocation method. It should be noted that by using the polynomial chaos expansion, sensitivity analysis can be carried out without any additional effort (Sudret [147]). In the two-step approach, first the sensitivity analysis is carried out with large number of input random variables with lower order polynomial chaos. Then important input random variables are selected from the initial variables, and then as a second step the chaos collocation method is carried out with higher order polynomial chaos. Loeven et al. [84] applied the two-step approach to a linear piston problem with an unsteady boundary condition, and compare different spectral methods, namely: the polynomial chaos method, the stochastic collocation method and the chaos collocation methods. The polynomial chaos method uses Askey scheme to determine orthogonal polynomials, and the stochastic collocation project the input random variables to so-called α domain. The chaos collocation method uses Lagrange interpolation to construct polynomials. In the examples of Loeven et al. [84] the chaos collocation gave the most accurate results. Loeven et al. [85] applied the two-step approach with the chaos collocation method to the NACA0012 airfoil problem. From eight input random variables the most important three variables, namely: freestream velocity, angle of attack and the camber of the airfoil, were selected by the first step. CFD simulations are solved with RANS modeling. There are several methods in the spectral method, for example, Hosder et al. [67] applied the point collocation non-intrusive polynomial chaos method to CFD simulations. The point collocation non-intrusive polynomial chaos methods uses the regression method to determine coefficient of the polynomials, which are often determined by the Gauss quadrature. Carnevale et al. [24] applied the probabilistic collocation method to heat transfer in internal channels. The detail of each method will be given in greater detail later. Since the spectral methods is a surrogate model, Walters et al. [159] compares the results with one estimated by the MC method with 10,000 samples to confirm its accuracy. In order to investigate effect of accuracy of deterministic simulations, Carnevale et al. [24] uses two different deterministic simulations, namely: Numerical Large Eddy Simulation(NLES) and steady RANS. By comparing stochastic results from two different deterministic simulations, it is found that the propagated uncertainties are turbulence model dependent and it is recommended to use high-fidelity model to get rid of the model uncertainty. Montomoli et al. [97] applied the probabilistic collocation method to transient three dimensional thermomechanical analysis. Then, in order to investigate the effect of shape of input PDF, Montomoli et al. [97] uses two different PDFs for an input random variable and compared the results. One is the Gaussian distribution and the other is the t-distribution which is a fat-tailed distribution which can express

rare event. Usually the used polynomial order for CFD simulations is 4, Shimoyama et al. [138] further investigated appropriate polynomial order and number of sampling points for the non-intrusive polynomial chaos methods and they observed that if the order of polynomial chaos is increased, it is possible that unphysical oscillation occurred. To further reduce total computational costs the spectral methods have been combined to Kriging models. Sakai et al. [133] uses the co-Kriging method, which is an extension of the Kriging method, for estimation of deterministic results at several collocation points instead of carrying out high-fidelity deterministic simulations at every collocation point. As introduced above the non-intrusive spectral methods have been widely used for CFD problems, however, there are some researches which applied intrusive methods or the Monte Carlo (MC) methods to CFD problems. Kawai et al. [76] used the Kriging method and estimate non-smooth response output by MC methods. Kawai et al. [76] carried out 7 CFD simulations and by using Kriging model estimated 10,000 samples for the MC method. Kawai et al. [76] found that for non-smooth function, the Kriging-model-based gives better accuracy and robustness than the polynomial chaos methods. Huyse et al. [70] applied the MC methods to a one-dimensional Burger equation model and studied propagation of uncertainty of the viscosity and boundary conditions. The input uncertainties are considered in different approaches, one is random variables and the other is random fields. Pisaroni et al. [115] carried out the Continuation Multi-Level Monte Carlo (C-MLMC) methods to the 2D RAE-2822 transonic airfoil and the 3D NASA rotor 37 using RANS simulations. It should be noted that, since spatial discretization plays an important role for CFD simulations, distances from first grid node to the wall were kept same in every mesh level. Geneva et al. [57] carried out UQ with the MC method using data-driven RANS simulations as a deterministic model. In the data-driven RANS simulations the Reynolds stress is predicted by Bayesian deep learning neural network. Model form uncertainties and epistemic uncertainties induced by limited training data are considered as input random variables and it is applied to the backwards step and wall mounted cube problem. So far all introduced literature uses CFD solver as *black box*, however, Xiu et al. [168] applied the intrusive polynomial chaos method to the Navier-Stokes equation. In Xiu et al. [170] the introduced method is expanded to Fluid Structure Interaction (FSI) problems. Since most of open-source or industrial CFD codes are complicated and it takes massive effort to rewrite and carry out V&V, the non-intrusive methods becomes getting more attention compared to intrusive methods. Overall in the CFD simulations other than CWE problems, it has been investigated to apply UQ using LES as deterministic simulations. It has been reported that the model uncertainties has non-negligible effect to the stochastic results (e.g. Carnevale et al. [24]), in case only low-fidelity models as RANS are used as a deterministic simulation.

2.2 Overview of the multi-fidelity framework in CFD

In previous section, UQ application to the CWE problems and other CFD problems have been introduced. As described, the challenge of application of UQ to CFD problems is its high computational cost, since UQ requires to run a deterministic simulation several times. Especially CWE problems often has significantly high Reynolds number comparing to mechanical engineering problems introduced above. In addition computational domain is also larger in CWE compared to the mechanical engineering problems and it leads to large mesh, for example, models introduced in later chapters such as Silsoe cube problems have 3,000,000 cells and BARC problem has 50,000 cells. The higher Reynolds number requires finer mesh resolution, finer time resolution and longer simulation time to get statistical values. Having summarized previous section, in order to reduce required number of deterministic simulations, the spectral methods has been widely used for CFD problems. In practical point of view it is still difficult to apply the spectral methods even using RANS simulations, however, it has been also reported that the low-fidelity model can produce model uncertainties, as Carnevale et al. [24] recommended to use high-fidelity model to get rid of the model uncertainties. To further reduce the total computational cost and reduce model uncertainties of low-fidelity model, the multi-fidelity frame work is applied in this thesis. The multi-fidelity framework has been used not only for UQ but also for other objectives such as optimizations. Peherstorfer et al. [112] identifies three strategies through which high-fidelity simulations may be leveraged by larger data sets of low-fidelity model evaluations, namely: fusion, filtering and adaptation. The fusion method combines available information from all outputs, an example being the method presented in Pepper et al. [113], in which experimental data is used in order to adjust the polynomial chaos expansion coefficients by maximizing the entropy subjected to the experimental data. The filtering method runs the high-fidelity simulations based on the low-fidelity filter while the adaptation method creates a multi-fidelity model by training a meta-model with the discrepancies between the high- and low- fidelity models. There are three literature which apply multi-fidelity or multi-level hierarchy to the stochastic collocation method. The adaptation method is applied in Eldred et al. [45] to the multi-fidelity framework. Narayan et al. [102] uses filtering method, such that first evaluate the low-fidelity model and choose where the high-fidelity models are evaluated depending on the results of low-fidelity model. Teckentrup et al. [155] carried out Multi-Level Stochastic Collocation method (MLSC) with hierarchical FEM models and found that the MLSC is more accurate and efficient than Multi-Level Monte Carlo (MLMC) up to number of random variables 20. The methodology used in Teckentrup et al. [155] is categorized to fusion.

Now let us look at different fidelity models used in literature. There has been many different fidelity CFD models available, and Giselle Fernández-Godino et al. [58] summarized literature which use multi-fidelity models for development of surrogate models. According to Giselle Fernández-Godino et al. [58], Polynomial Chaos Expansion (PCE) is a surrogate model classified as one of the response surface methods. Giselle Fernández-Godino et al. [58]

introduced following types of models which are used as high- and low-fidelity models, namely: analytical model, empirical model, linear model, potential flow, Euler flow and RANS. Since there are many possibilities to choose high- and low- fidelity models, we might be interested in criteria to choose proper high- and low- fidelity in terms of high accuracy of the combined results. However, Giselle Fernández-Godino et al. [58] does not indicate that there is any specific tendency to get better results depending on models used in the multi-fidelity framework. Several validation techniques of the multi-fidelity framework exist, for example, Park et al. [111] compares several multi-fidelity framework quantitatively by comparing Root Mean Square Error (RMSE) from high-fidelity results. Park et al. [111] compared two types of multi-fidelity system, one is a simple framework and the other is a Bayesian framework. Park et al. [111] concluded that the Bayesian framework has better accuracy than the simple framework, however, the improvement is small compared to large effort to implement the Bayesian framework. To the best of authors knowledge, there has been no specific and systematic way to choose high- and low- fidelity model and so far it should be chosen by experience.

2.3 Possible multi-fidelity models for CWE problems

In previous section, the multi-fidelity framework used in a wide range of areas of CFD is introduced. In this section, we are focusing on finding suitable multi-fidelity frameworks for CWE problems. First possible models which have different fidelity are reviewed. Then, based on the literature review a multi-fidelity model will be chosen for this thesis. Recently CFD simulations have been increasingly used for CWE problems. CFD simulations for CWE problems can be categorized as:

(a) Buildings (structural stability and human comfort inside and outside of the buildings)

(b) Bridges

(c) Wind turbines

(d) Airfoils

In cases of (a), (b) and (c), the flow is normally the atmospheric boundary layer (ABL) flow and no variation of the fluid properties are considered and these problems are called as Computational Wind Engineering (CWE) problems (Franke et al. [50]). In ABL, the Reynolds number is calculated as $Re = 67,000UL$, where U is the reference wind velocity [m/s] and L is the reference length [m] (Simiu et al. [140]). It is to say that the Reynolds number in CWE can easily exceed $Re = 1.0 \times 10^6$, which is known to be very high Reynolds number for CFD simulations. The other specific problem for CWE problems is that except c) wind turbines civil engineering structures have bluff body shape such as buildings and bridges. Characteristic of the flow around the bluff body shape is that edges of the structure causes flow

separation and the separation leads to vortex shedding. Many multi-fidelity models have been developed in field of wind turbines, since simulations of wind turbines often require fluid-structure interaction simulations and its computational cost becomes very high (Sprague et al. [142] and Padron et al. [109]). For buildings and bridges, the multi-fidelity framework has still not yet been commonly used. One reason is that according to Giselle Fernández-Godino et al. [58], more than half of reviewed journal papers use multi-fidelity framework for optimization purpose, and in the field of buildings and bridges, the optimization is not commonly used. There are few literature in recent years to apply multi-fidelity framework to the optimization for bridges and buildings. For example, Bernardini et al. [14] applied optimization to design of high rise buildings and Ding et al. [37] carried out a multi-fidelity shape optimization to design a cross section of a building. Ding et al. [37] used LES as a high-fidelity model and URANS as a low-fidelity model, and then developed a surrogate model using Co-kriging method. As mentioned in previous section, according to Giselle Fernández-Godino et al. [58], following models have been used in CFD simulations:

1. Analytical expressions
2. Empirical relations
3. Numerical linear approximations
4. Potential flow
5. Numerical non-linear non-viscous approximation (Euler equation)
6. RANS

To give an example of each method, the selective averaging method (Sankar et al. [134]) is one of the analytical expressions and it has been used for the micro-structural composites problems (Goldsmith et al. [59]). The Tadpole program (Cousin et al. [33]) is one of the empirical relations which estimate drag coefficient empirically. The low-order panel methods (Maskew [94]) is one of the numerical linear approximations. Forrester et al. [49] carried out multi-fidelity optimization, in which the Tadpole program is used as a low-fidelity model and the low-order panel methods is used as a high-fidelity model. Forrester et al. [49] investigate a generic transonic civil aircraft wing using aforementioned multi-fidelity optimization method. Another example of numerical linear approximation is a blade element/vortex lattice aerodynamic model implemented as CACTUS (Murray et al. [100]). Padron et al. [109] carried out the multi-fidelity uncertainty quantification using the CACTUS as the low-fidelity model and the Euler equation as the high-fidelity model. In Padron et al. [109] vertical axis wind turbines are investigated. As an example of the potential flow and Euler equation, Nelson et al. [103] carried out the multi-fidelity optimization to the PARSEC airfoil, using the non-linear potential solver TRAN2D as low-fidelity model and the Euler equation as the high-fidelity model. Thus, most of the low-fidelity models have been applied to wind turbines or airfoils. On the other hand, having considered that the flow around the bluff body has non-linear and unsteady characteristics, it

has been known that for CFD simulations of the bluff body shape structures it is required to invoke Navier-Stokes equations (Dowell et al. [38]). Wu et al. [167] developed a low-dimensional model based on the Volterra series, however it is recommended to use the higher order approximation for the flow around the bluff body at high Reynolds number. Having considered that the objective of this thesis is to carry out the multi-fidelity UQ for architectural wind engineering problem, we now conclude that the RANS/URANS models are used as low-fidelity model and the LES model is used as the high-fidelity model.

Chapter 3

Methodology

In this chapter, the theory of deterministic CFD simulations and Multi-fidelity Non-Intrusive Polynomial Chaos method (MF-NIPC) are introduced. First we introduce the theory of two different fidelity CFD simulations, namely: Unsteady Reynolds Averaged Navier Stokes (URANS) as a low-fidelity model and the Large Eddy Simulations (LES) as a high-fidelity model. Then, the Non-intrusive Polynomial Chaos (NIPC) methods and its multi-fidelity extension will be introduced. Finally the software management to carry out MF-NIPC will be explained.

3.1 CFD simulations

All CFD simulations in this thesis are carried out by open source code KratosMultiphysics (Ferrándiz et al. [48]). In KratosMultiphysics, the CFD simulations are implemented based on Finite Element Methods (FEM). Many well-known software for CFD simulations have been developed based on Finite Volume Method (FVM), such as OpenFOAM(Weller et al. [160]). An advantage of the FEM based CFD is that FEM based methods can express more accurate geometry of complicated structures by using unstructured tetrahedra or triangle elements. Because of this advantage, the FEM based CFD simulation has been often used for multi-physics simulations because of its capability to express the deformed configuration (Helgedagsrud et al. [65]). In addition, this feature is a great advantage for UQ as well, for example, in a case that geometry of structures are considered as input random variables and it is required to change the geometry accurately. In order to carry out CFD simulations in practical engineering problems, it is necessary to use models to the Navier-Stokes equations. As discussed in previous chapter, in this thesis two models for CFD simulations are used for the multi-fidelity framework,

one is LES and the other is URANS.
The incompressible Navier-Stokes equations in the computational domain Ω are given by

$$\rho\partial_t\mathbf{u} + \rho(\mathbf{u}\cdot\nabla)\mathbf{u} - \nabla\cdot\sigma = \mathbf{f}, \tag{3.1}$$

$$\nabla\cdot\mathbf{u} = 0, \tag{3.2}$$

where $\mathbf{u}$ is the fluid velocity, ρ is the fluid density, σ is the stress tensor and $\mathbf{f}$ is the external force acting on the domain. The incompressible Navier-Stokes equation Eq. (3.1) and Eq. (3.2) are numerically solved with initial condition and boundary conditions. The initial condition and the boundary conditions are written as:

$$\mathbf{u} = \mathbf{u}_0 \quad \text{in} \quad \Omega, t = 0, \tag{3.3}$$

$$\mathbf{u} = \mathbf{u}_D \quad \text{in} \quad \Gamma_D, \tag{3.4}$$

$$\partial_n\mathbf{u} = constant \quad \text{in} \quad \Gamma_N. \tag{3.5}$$

Eq. (3.3) is the initial condition where $\mathbf{u}_0$ is the initial velocity given to whole domain Ω. The boundary of computational domain $\partial\Omega$ is divided to two types of boundaries, one is the Dirichlet boundary Γ_D and the other is the Neumann boundary Γ_N. Eq. (3.4) is the Dirichlet boundary condition, where $\mathbf{u}_D$ is inlet velocity imposed to inlet boundary. Eq. (3.5) is the Neumann boundary condition. The Neumann boundary condition is imposed to the gradient normal to the boundary.
For the Newtonian fluid the stress tensor is expressed as:

$$\sigma = -p\mathbf{I} + 2\mu(\nabla^s\mathbf{u} - \frac{1}{3}(\nabla\cdot\mathbf{u})\mathbf{I}), \tag{3.6}$$

where $\mathbf{I}$ is the second order identify tensor, μ is the fluid viscosity and $\nabla^s\mathbf{u}$ is the symmetric gradient velocity defined as:

$$\nabla^s\mathbf{u} = \frac{1}{2}(\nabla\mathbf{u} + (\nabla\mathbf{u})^T). \tag{3.7}$$

The Galerkin weak form of the incompressible Navier-Stokes equations are written as:

$$\int_\Omega \mathbf{w}(\rho\partial_t\mathbf{u} + \rho\mathbf{u}\cdot\nabla\mathbf{u} - \nabla\cdot\sigma)d\Omega = \int_\Omega \mathbf{w}\cdot\mathbf{f}d\Omega, \tag{3.8}$$

$$\int_\Omega w_q\nabla\cdot\mathbf{u}d\Omega = 0, \tag{3.9}$$

where $\mathbf{w}$ is the velocity test function and w_q is the pressure test function.

3.1.1 Large Eddy Simulations

The problem variables in Eq. (3.1) and Eq. (3.2) can be separated to small scale variables $\mathbf{u}_S, p_S$ and large scale variables $\mathbf{u}_H, p_H$ as:

$$\mathbf{u} = \mathbf{u}_H + \mathbf{u}_S, \tag{3.10}$$

$$p = p_H + p_S. \tag{3.11}$$

The small scales are all variables that are smaller than elements of spatial discretization, and the large scales are ones that are larger than the elements. The small scale variables are modeled as:

$$\rho\partial_t\mathbf{u}_S + \frac{1}{\tau_u} \approx \mathbf{R}^m(\mathbf{u}_H, p_H) - \xi_H \quad \text{and} \quad \frac{1}{\tau_p}p_S \approx R^c(\mathbf{u}_H) - \delta_H, \tag{3.12}$$

where $\mathbf{R}^m$ and R^c are the strong form residual of the Navier-Stokes equations and τ_u and τ_p are stabilization parameters. ξ_H and δ_H values are determined depending on stabilization methods, namely: the algebraic sub-grid scales (AGSG) or orthogonal sub-grid scales (OSS) (Codina et al. [29]). To consider time evolution of the velocity small scale, time discretization is written as:

$$\rho\frac{\mathbf{u}_S^{n+1} - \mathbf{u}_S^n}{\delta t} + \frac{1}{\tau_u}\mathbf{u}_S^{n+1} = \mathbf{R}^m(\mathbf{u}_H, p_H)|_{n+1}. \tag{3.13}$$

Eq. (3.13) is rewritten as:

$$(\frac{\rho}{\delta t} + \frac{1}{\tau_u})\mathbf{u}_S^{n+1} = \mathbf{R}^m(\mathbf{u}_H, p_H)|_{n+1} + \frac{\rho}{\delta t}\mathbf{u}_S^n. \tag{3.14}$$

Due to large amount of required memory to store the old small scale data, $\mathbf{u}_S^n$ in Eq. (3.14) is neglected in KratosMultiphysics implementation. In addition, $\frac{\rho}{\delta t}$ is multiplied by a stabilization parameter *dynamic tau*, to avoid instability. Using the modeled $\mathbf{u}_S$ and p_S, the large scale variables are solved by FEM. As a time discretization method for the large scale variables, the Bossak time integration method(Wood et al. [164]), which is one of the generalized α Newmark method and has second-order accuracy, is used. The detailed explanation about the implementation of KratosMultiphysics may be found in Dalmau [35]. It should be noted that in this implementation the LES turbulence model, such as dynamic Smagorinsky model, is not used. As a matter of fact the aforementioned stabilization method is called as the Variational Multiscale (VMS) mthod, which is often used in FEM for fluid problems (Hughes [69]). Provided the mesh sizes are small enough, the scale separation of VMS can be thought of as analogous to the scale separation by filtering in LES (Codina et al. [29]). Therefore in this thesis this method is referred to as LES simulations.

3.1.2 Unsteady Reynolds Averaged Navier Stokes simulations

In URANS it is assumed that the velocity can be separated to the time-averaged component $\mathbf{U}$ and the fluctuating component $\mathbf{u}'$. By taking time

average of Eq. (3.1), it gives:

$$\rho\nabla_t\mathbf{U} + \rho\mathbf{U} + \rho U \cdot \nabla\mathbf{U} - \nabla\sigma = \mathbf{f} + \rho\nabla(-\overline{\mathbf{u}'\mathbf{u}'}). \tag{3.15}$$

The first term of Eq. (3.15) is neglected in case of RANS but it will remain for URANS. Iaccarino et al. [71] pointed out that URANS gives more accurate results than RANS, in cases where the flow is not statistically stationary. In this thesis, flow around bluff body structures will be investigated that are not statistically stationary. Therefore, URANS is used in this thesis instead of RANS. The last term of Eq. (3.15) is called as the Reynolds stress and is written as:

$$-\overline{\mathbf{u}'\mathbf{u}'} = 2\frac{\mu_T}{\rho}\mathbf{S}, \tag{3.16}$$

where

$$S_{ij} = \frac{1}{2}(\frac{\partial U_i}{\partial x_j} + \frac{\partial U_j}{\partial x_i}), \tag{3.17}$$

and μ_T is the eddy viscosity. There are several models used for μ_T. The models are often classified by number of transport equations, such as zero-equation model, one equation model, two equation models and so on. The more equations that are used, the more accurate the results, however the computational cost becomes higher. In this paper the Shear Stress Transport (SST) $k-\omega$ model, which is one of two equations model, is used. The SST $k-\omega$ model is introduced by Menter [95]. There are three well-known two equation model for the eddy viscosity. One is $k-\varepsilon$ model, another is the $k-\omega$ model and the other is the SST $k-\omega$ model. In the SST $k-\omega$ model, the $k-\omega$ model is used at the near wall region, otherwise the $k-\varepsilon$ model is used, because it has been known that $k-\omega$ model is more robust in near wall region. The eddy viscosity μ_T is calculated by k (Turbulence Kinetic Energy) and ε (Turbulent dissipation rate) as:

$$\mu_T = \rho C_\mu \frac{k^2}{\varepsilon}, \tag{3.18}$$

where C_μ is a constant value determined empirically. μ_T can be also expressed using k (Turbulence Kinetic Energy) and ω (Turbulent specific energy dissipation rate) as:

$$\mu_T = \rho\frac{k}{\omega}. \tag{3.19}$$

In the SST $k-\omega$ model, the kinematic Eddy viscosity $\nu_T = \mu_T/\rho$ is calculated as:

$$\nu_T = \frac{a_1 k}{max(a_1\omega; SF_2)}, \tag{3.20}$$

where a_1 is a constant, $S = \frac{\partial u}{y}$ and F_2 is a constant which has value of one in boundary layer flow and zero in free shear layer. k and ω are calculated by:

$$\frac{\partial k}{\partial t} + U_j\frac{\partial k}{\partial x_j} = P_k - \beta^* k\omega + \frac{\partial}{\partial x_j}[(\nu + \sigma_k\nu_T)\frac{\partial k}{\partial x_j}] \tag{3.21}$$

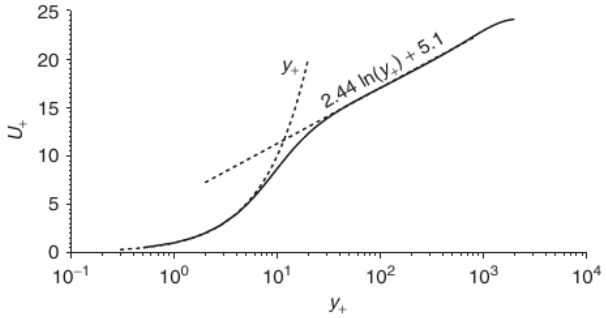

Figure 3.1: The law of the wall (Durbin et al. [41])

$$\frac{\partial \omega}{\partial t} + U_j \frac{\partial \omega}{\partial x_j} = \alpha S^2 - \beta \omega^2 + \frac{\partial}{\partial x_j}[(\nu + \sigma_\omega \nu_T)\frac{\partial \omega}{\partial x_j}] + 2(1 - F_1)\sigma_\omega 2 \frac{1}{\omega} \frac{\partial k}{\partial x_j} \frac{\partial \omega}{\partial x_i}, \tag{3.22}$$

where β^*, σ_k, α, β, σ_ω and $\sigma_{\omega 2}$ are constants, and F_1 is a constant which has value of one near wall region and zero away from the surface. Eq. (3.21) and Eq. (3.22) are called as the turbulence transport equations and solved by FEM. For the stabilization of the turbulence transport equation, a hybrid method based on the Discrete Maximum Principle (DMP), the Algebraic Flux Correction (AFC) method and the Cross Wind Diffusion method (Kuzmin et al. [78]) is used. The Bossak time integration method is used as the time integration scheme.

3.1.3 Wall treatment

The boundary conditions of wall boundaries for both LES and URANS are usually determined based on the dimensionless wall distance y^+, which is defined as:

$$y^+ = \frac{y u_\tau}{\nu}, \tag{3.23}$$

where y is a distance from the wall, u_τ is the friction velocity and ν is the kinematic viscosity. u_τ is calculated by:

$$u_\tau = \sqrt{\frac{\tau_w}{\rho}}, \tag{3.24}$$

where τ_w is the shear stress at the wall and ρ is density of the flow. The dimensionless velocity u^+ is calculated as:

$$u^+ = \frac{\|\mathbf{u}\|}{u_\tau}. \tag{3.25}$$

The relationship between u^+ and y^+ in near wall region is depicted in Fig. 3.1. In outer region, u^+ and y^+ follows the log law as:

$$u^+ = \frac{1}{\kappa} \ln y^+ + \beta, \tag{3.26}$$

where κ is the von Karman constant $\kappa \approx 0.41$ and β is a constant $\beta \approx 5.1$. β is determined according to wall roughness, and these constants have been determined empirically. The inner region is called viscous sublayer and u^+ and y^+ follows:

$$u^+ = y^+. \tag{3.27}$$

It has been known that the two formulas intersect at $y^+ \approx 11$ (Durbin et al. [41]) and the region between viscous sublayer and the log law region is called as the buffer layer. If the first node from the wall is located outside of the viscous sublayer, wall functions may be used as wall boundary conditions with slip conditions instead of no-slip conditions, especially if linear shape function elements are used for FEM discretization. This is because the linear elements cannot express the non-linearity of the viscous sublayer. For VMS simulations it has been sought to impose the no slip condition weakly (Bazilevs et al. [13]) or to use higher order shape functions (Ravensbergen et al. [116]), to improve accuracy of flow close to wall. To determine the wall treatment and the first grid, y^+ may be estimated before running simulations. y^+ can be estimated before running simulations by estimating the wall shear stress τ_w from the skin friction coefficient C_f which is estimated by the Reynolds number (Schlichting [137]). However, this estimation is based on an assumption for flow over a flat plate and not applicable to all problems. In case estimation of y^+ is not possible, for example for structures that are not flat plates or have more complicated shapes, y^+ should be calculated in postprocess using resulted reaction. The wall shear stress τ is calculated as:

$$\tau = \frac{\mathbf{R} - (\mathbf{R} \cdot \mathbf{n})\,\mathbf{n}}{A}, \tag{3.28}$$

where $\mathbf{R}$ is the reaction, $\mathbf{n}$ is the outward pointing unit normal and A is the surface area of the condition.

In KratosMultiphysics two types of wall functions are implemented. One is the Werner Wengle Wall model (Werner et al. [161]) and the other is the simple log-law model. Though there are some possible wall functions, Temmerman et al. [156] pointed out that results are more sensitive to its implementation than type of the wall functions. In this chapter the implementation of the log-law wall function is introduced. The interested reader for the Werner Wengle wall model may refer to Andre [9]. A flowchart of implementation of the Neumann boundary condition using the wall function is illustrated in Fig. 3.2. First, y^+_{limit}, which is the boundary of the linear region ($u^+ = y^+$) and the log law region ($u^+ = \frac{1}{\kappa} \ln y^+ + \beta$), is calculated by solving the following equation by the Newton-Raphson method.

$$y^+_{limit} = \frac{1}{\kappa} \ln(y^+_{limit}) + \beta \tag{3.29}$$

Assuming that the first node is in the linear region, u_τ is calculated by solving:

$$u^+ = y^+ \Leftrightarrow \frac{|\mathbf{u}|}{u_\tau} = \frac{u_\tau y}{\nu}. \tag{3.30}$$

Once u_τ is calculated, y^+ is calculated by Eq. (3.23). Then y^+ is compared with y^+_{limit}, and if $y^+ > y^+_{limit}$, u_τ is recalculated by solving following equation by the Newton-Raphson method.

$$\frac{|\mathbf{u}|}{u_\tau} = \frac{1}{\kappa}\ln(y^+_{limit}) + \beta \tag{3.31}$$

Finally the Neumann boundary condition is applied by:

$$\int_{\Gamma_N} N^a t_i d\Gamma_N = -\int_{\Gamma_N} N^a \rho u_\tau^2 \frac{u_i}{|\mathbf{u}|} d\Gamma_N, \tag{3.32}$$

where Γ_N is the Neumann boundary and N^a is a shape function and t_i is the traction on the Neumann boundary.

In the SST $k-\omega$ model, the Neumann boundary condition due to the wall stress should be considered to the turbulence transport equations. The traction at the Neumann boundary g_N is calculated as:

$$g_N = \frac{u_\tau^3}{\kappa C_\mu^0 .5(y^+\nu)^2}. \tag{3.33}$$

KratosMultiphysics has two types of solvers. One is the monolithic solver and the other is the fractional step solver. In the monolithic solver the pressure and velocity are solverd at the same time, and in the fractional step solver the pressure and velocity are uncoupled. Interested readers are referred to Dalmau [35] for monolithic solver implementation and Andre [9] for fractional step solver implementation. Codina et al. [29] pointed out that the fractional step solver is more stable compared to the monolithic solver, and it has been observed that the monolithic solver has convergence issues. The solver type should be carefully selected depending on the requirement for models. For example, fractional step solver requires high effort to implement the periodic boundary conditions which is often used for CFD simulations.

3.2 Multi-Fidelity Non Intrusive Polynomial Chaos methods

In this section the theory of the MF-NIPC is introduced. As mentioned in the previous chapter, NIPC is getting attention in CFD field thanks to its comparably low computational cost. In this section, first the basic theory of the NIPC is introduced and then it is expanded to multi-fidelity framework.

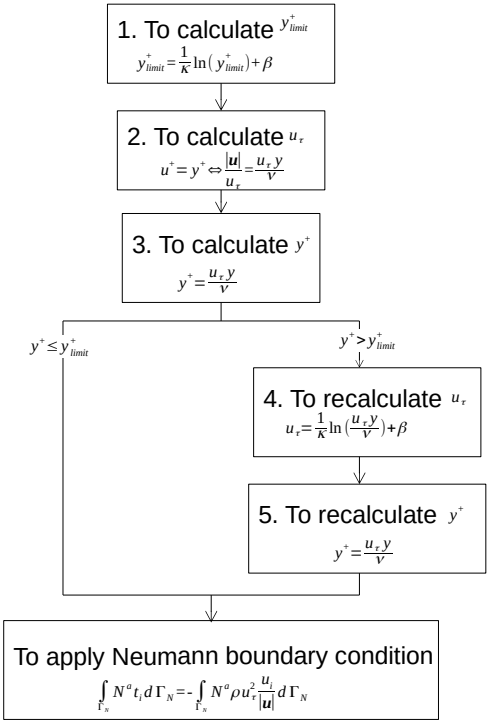

Figure 3.2: Implementation of the Neumann boundary condition using the wall function

3.2.1 Non-Intrusive Polynomial Chaos methods

Let us consider a stochastic CFD problem. The unknown Quantity of Interest (QoI), Y, is calculated as a function of d uncertain inputs:

$$Y = g(\mathbf{X}), \tag{3.34}$$

where $\mathbf{X} = [X_1, X_2, ..., X_d]$ are the input random variables and g refers to the results of a CFD simulation for these inputs. A single evaluation of g may be computationally expensive, for this reason we wish to construct a meta-model for g based on a limited training set of model evaluations. Assuming that Y is second-order ($E[Y^2] < \infty$), Y can be expressed with orthogonal polynomials as:

$$Y = \sum_{k \in \mathbf{N}^d} a_k \Psi_k(\mathbf{X}), \tag{3.35}$$

where $\Psi_k(\mathbf{X})$ is a multivariate orthogonal polynomial, which itself is a product of univariate orthogonal polynomials. The contribution of these polynomials to the summation is weighted by the Polynomial Chaos Expansion (PCE) coefficients, a_k. The polynomial basis may be user selected; for certain families of probability distribution an optimal choice of polynomial basis exists, referred to as the Wiener-Askey scheme (Xiu et al. [169]). Alternatively, the polynomials may be calculated directly from the available data for the inputs. This method, referred to as arbitrary Polynomial Chaos (aPC), is used in this thesis and will be discussed in greater detail below. For practical implementations, the summation in Eq. (3.35) is truncated, with the pth order Polynomial Chaos approximation of Y expressed as:

$$Y \approx \sum_{k=1}^{P} a_k \Psi_k(\mathbf{X}). \tag{3.36}$$

The total number of terms, P, in the expansion is calculated as:

$$P = \frac{(p+d)!}{p!d!}. \tag{3.37}$$

The PCE coefficients, $\mathbf{a} = \{a_1, \ldots, a_P\}^\top$, must be determined numerically. There are several methods to calculate the PCE coefficients a_k in Eq. (3.36) such as: the pseudo-spectral projection method, the point collocation method and the stochastic collocation method (see, e.g. Le Maître et al. [80]). Each method will be explained below.

3.2.1.1 The pseudo-spectral projection method

The pseudo-spectral projection method calculate the PCE coefficients $\mathbf{a} = \{a_1, \ldots, a_P\}^\top$ by numerical integration as:

$$\begin{aligned} a_k &= \frac{1}{||\Psi_k||} \int_{\mathbf{X}\in\Omega} Y(\mathbf{X})\Psi_k d\Gamma(\mathbf{X}) \\ &\approx \frac{1}{||\Psi_k||} \sum_{j_1=0}^{q_1} \cdots \sum_{j_d}^{q_d} Y(X_{j_1}, \ldots, X_{j_d})\Psi_k(X_{j_1}, \ldots, X_{j_d})(w_{j_1} \ldots w_{j_d}), \end{aligned} \tag{3.38}$$

where N_U is the dimension of input random variables, q_i is the number of Gauss quadrature points in each dimension and $||\Psi_k||$ is the norm of the orthogonal polynomials. The quadrature points $(X_{j_1}, \ldots, X_{j_d})$ and the quadrature weights $(w_{j_1}, \ldots, w_{j_d})$ are calculated following Golub and Welsch (Golub et al. [60]). To exactly integrate the p th order polynomial, the Gauss integration requires $2q - 1 > p$ quadrature points. Considering that Eq. (3.38) integrates $2p$ th order polynomials, the number of quadrature points should be $2q-1 > 2p$. The total number of collocation points increases exponentially with dimension of the input random variables, it is called the *curse of dimensionality*. To overcome the *curse of dimensionality*, sparse quadrature methods have often been used. The Smolyak quadrature rule $Q_{d,k}$ for level k is calculated as:

$$Q_{d,k} = \sum_{k-d}^{k-1} (-1)^{(k-1-i)} \binom{d-1}{k-1-i} \sum_{q\in N_i^d} Q_{q_1} \otimes \ldots Q_{q_d}, \tag{3.39}$$

where Q_{q_j} is the Gauss quadrature for a variable X_j. The further explanation of the Smolak quadrature is included in Appendix B.

3.2.1.2 Point collocation method

The point collocation method is based on linear regression. Assuming that there are N deterministic results of the CFD simulation $g(\cdot)$ available a set of linear equations can be constructed:

$$\begin{bmatrix} \Psi_1(\mathbf{X}_1) & \ldots & \Psi_P(\mathbf{X}_1) \\ \Psi_1(\mathbf{X}_2) & \ldots & \Psi_P(\mathbf{X}_2) \\ \vdots & \ddots & \vdots \\ \Psi_1(\mathbf{X}_N) & \ldots & \Psi_P(\mathbf{X}_N) \end{bmatrix} \begin{bmatrix} a_1 \\ a_2 \\ \vdots \\ a_P \end{bmatrix} = \begin{bmatrix} g(\mathbf{X}_1) \\ g(\mathbf{X}_2) \\ \vdots \\ g(\mathbf{X}_N) \end{bmatrix}, \tag{3.40}$$

where $g(\mathbf{X}_i)$ refers to a model evaluation at the ith sample point in the uncertain input space. The PCE coefficients $\mathbf{a}$ are estimated by solving the least-squares optimisation problem:

$$\mathbf{a} = \underset{\mathbf{a}\in\mathbb{R}^P}{\operatorname{argmin}} \sum_{i=1}^{n} \{g(\mathbf{X}_i) - \mathbf{a}^T \mathbf{\Psi}(\mathbf{X}_i)\}^2. \tag{3.41}$$

From these equations it is clear that a tradeoff exists between the accuracy of the PCE and the size of the training dataset: increasing the order of the PCE will increase the number of terms in the expansion and hence improve its accuracy, however, this will require more PCE coefficients to be found numerically. This tradeoff in part motivates our use of multi-fidelity PCE in this thesis. In point collocation methods, the choice collocation points $(X_{j_1}, \ldots, X_{j_d})$ is made by the user, however usually the Gaussian quadrature points are chosen as the collocation points, which is also the case in this thesis.

3.2.1.3 Stochastic Collocation method

The stochastic collocation method is based on the Lagrange polynomial interpolation. The stochastic collocation method does not estimate the PCE coefficient in Eq. (3.36), but estimate response surface of Y by Lagrange interpolation as:

$$Y \approx \sum_{i=1}^{N} g(\mathbf{X}^{(i)})\mathbf{L}^{(i)}(\mathbf{X}), \tag{3.42}$$

where N is the number of collocation points and $\mathbf{L}$ is the Lagrange polynomials. The multi-variate Lagrange polynomials are calculated as:

$$\mathbf{L}^{(i)}(\mathbf{X}) = l^{(i)}(X_1) \otimes l^{(i)}(X_d), \tag{3.43}$$

where $l^{(i)}(X_j), j = 1, \ldots, d$ is the one dimensional Lagrange polynomials:

$$l^{(i)}(X_j) = \prod_{k=1, k\neq j}^{N} \frac{X_j - X_j^{(k)}}{X_j^{(i)} - X_j^{(k)}}. \tag{3.44}$$

It is known that Lagrange polynomial is not stable for some set of interpolation points (Gasca et al. [56]) and not all Gaussian quadrature points are stable with respect to Lagrange interpolation. The collocation points should be carefully chosen, so that the Lagrange interpolations are stable.

3.2.1.4 Postprocess

The goal of UQ is to estimate the statistical moments and PDF of QoI Y. Mean and variance of Y can be calculated from the PCE coefficient $\mathbf{a}$ as:

$$E[Y_p] = a_1, \tag{3.45}$$

$$E[Y_p^2] = \sum_{k=1}^{P} a_k^2, \tag{3.46}$$

where Y_p is the QoI estimated by p th order polynomials. In order to calculate the PDF of Y_p, the Bootstrap methods (Efron [42]) may be used. According to the Bootstrap methods, the PDF of Y can be estimated from the bootstrap

samples $\mathbf{X}^*$, which is reproduced by an estimated PDF of samples of $\mathbf{X}$. The bootstrap distribution of Y is approximated as:

$$\begin{aligned} Y &\approx g(\mathbf{X}^*) \\ &= \sum_{k=1}^{P} a_k \Psi_k(\mathbf{X}^*) \end{aligned} \tag{3.47}$$

The calculation of Eq. (3.47) is usually done by the Monte Carlo approximation.

3.2.2 Arbitrary Polynomial Chaos method

As has been discussed, the choice of orthogonal polynomial in the PCE is made by the user, while in the case of arbitrary Polynomial Chaos (aPC) the orthogonal polynomials are derived from the matrices of sample moments. This is advantageous as aPC can calculate the orthogonal polynomials and the collocation points for any type of input distributions, while the Wiener-Askey scheme is restricted to several families of probability distribution, for example the Legendre polynomials for the uniform distribution and the Hermite polynomials for the normal distribution. aPC can therefore handle scarce data efficiently. SAMBA, the particular implementation of aPC used in this thesis, computes the orthogonal polynomials and collocation points from moment matrices of each input random variable using the theory of Golub et al. [60].

Let us consider finding p th order orthogonal polynomials and corresponding collocation points for a input random variable whose probability distribution is described by N samples $\xi_1, ..., \xi_N$. The kth raw moment m_k of the random variable is calculated as:

$$m_k = \frac{1}{N} \sum_{i=1}^{N} \xi_i^k. \tag{3.48}$$

The Hankel matrix M is defined as:

$$M = \begin{bmatrix} m_0 & m_1 & \dots & m_p \\ m_1 & m_2 & \dots & m_{p+1} \\ \vdots & \vdots & \ddots & \vdots \\ m_p & m_{p+1} & \dots & m_{2p} \end{bmatrix}. \tag{3.49}$$

Its Cholesky decomposition $M = R^T R$ is calculated as:

$$R = \begin{bmatrix} r_{11} & r_{12} & \dots & r_{1,p+1} \\ & r_{22} & \dots & r_{2,p+1} \\ & & \ddots & \vdots \\ & & & r_{p+1,p+1} \end{bmatrix}. \tag{3.50}$$

According to the Mysovskih theorem, an orthogonal system of polynomials can be determined by the inverse matrix of R. Instead of the inversion of the

matrix, Rutishauser [131] states that the polynomials $\psi_j(\xi)$ for $j = 1, \ldots, p$ can be determined of the three-term recurrence as:

$$\xi\psi_{j-1}(\xi) = b_{j-1}\psi_{j-2}(\xi) + a_j\psi_{j-1}(\xi) + b_j\psi_j(\xi), \tag{3.51}$$

where

$$a_j = \frac{r_{j,j+1}}{r_{j,j}} - \frac{r_{j-1,j}}{r_{j-1,j-1}}, b_j = \frac{r_{j+1,j+1}}{r_{j,j}}, \tag{3.52}$$

and $r_{0,0} = 1$ and $r_{0,1} = 0$. The optimal collocation points can be found by finding the eigenvalues of a symmetric tri-diagonal Jacobi matrix J:

$$J = \begin{bmatrix} a_1 & b_1 & & & & \\ b_1 & a_2 & b_2 & & 0 & \\ & b_2 & a_3 & b_3 & & \\ & & \ddots & \ddots & \ddots & \\ & 0 & & b_{p-2} & a_{p-1} & b_{p-1} \\ & & & & b_{p-1} & a_p \end{bmatrix}. \tag{3.53}$$

In addition, SAMBA adapts Smolyak's formula, in order to overcome the so-called *curse of dimensionality*. Smolyak's formula generates a sparse grid on which to sample from a set of d one-dimensional Gaussian quadrature rules. A parameter referred to as the level, l, controls the number of points in the sample grid. Typically we choose $l = p + 1$; again the accuracy of the Polynomial Chaos is conditioned by the polynomial order. For more details on the mathematical background of SAMBA, see Ahlfeld et al. [4].

3.2.3 Multi-fidelity Non-Intrusive Polynomial Chaos methods

While approaches such as Smolyak's algorithm can mitigate the computational cost of increasing the accuracy or dimensionality of a PCE, it is possible that the computational cost of Polynomial Chaos approaches may still be too high. This has motivated the development of multi-fidelity approaches such as that introduced by Eldred et al. [44] for multi-fidelity, non-intrusive Polynomial Chaos (MF-NIPC). The term 'non-intrusive' refers to the fact that $g(\cdot)$ is not altered in the formulation and may be evaluated as a black box. In the MF-NIPC framework, a limited set of expensive model evaluations is leveraged by a larger set of evaluations of a cheaper, although less accurate, model. These models are referred to as high-fidelity and low-fidelity models respectively. By evaluating the low-fidelity model at the collocation points corresponding to a high-order PCE, which will include the collocation points of lower-order PCEs at which the high-fidelity model is evaluated, the discrepancy between the models at the shared collocation points can be used to estimate a set of PCE coefficients for a high-order PCE. This PCE will have more terms than could be calculated if the high-fidelity model evaluations were used in isolation.

Mathematically, a stochastic expansion of the high-fidelity model, $g_h(\mathbf{X})$, is found in terms of a PCE for the low-fidelity model, $g_l(\mathbf{X})$, with PCE

parameters $\mathbf{a}_l$ and a PCE that represents the discrepancy, δ, between the two models, with associated PCE parameters $\mathbf{a}_\delta$:

$$\tilde{g}_h(\mathbf{X}) = \sum_{k \in J_q} a_{l,k} \Psi_k(\mathbf{X}) + \sum_{k \in J_{q-r}} a_{\delta,k} \Psi_k(\mathbf{X}) \tag{3.54}$$

where q is the sparse grid level, which corresponds to the order of polynomial, $r < q$ is the sparse grid level off set and J_q is the number of the orthogonal polynomials for the sparse grid level q. aPC is used to determine the optimal orthogonal polynomials, $\mathbf{\Psi}_k$. δ is the discrepancy between the high- and low-fidelity models and is expressed as:

$$\delta(\mathbf{X}) = g_h(\mathbf{X}) - g_l(\mathbf{X}). \tag{3.55}$$

It is possible to determine PCE coefficients either the pseudo-spectral projection methods or the point collocation methods. Here the point collocation methods are introduced. In order to determine the two sets of PCE coefficients the two terms on the RHS of Eq. (3.54) are written in matrix form as:

$$\begin{bmatrix} \Psi_1(\mathbf{X}_1) & \dots & \Psi_{J_q}(\mathbf{X}_1) \\ \Psi_1(\mathbf{X}_2) & \dots & \Psi_{J_q}(\mathbf{X}_2) \\ \vdots & \ddots & \vdots \\ \Psi_1(\mathbf{X}_N) & \dots & \Psi_{J_q}(\mathbf{X}_N) \end{bmatrix} \begin{bmatrix} a_{l,1} \\ a_{l,2} \\ \vdots \\ a_{l,J_q} \end{bmatrix} = \begin{bmatrix} g_l(\mathbf{X}_1) \\ g_l(\mathbf{X}_2) \\ \vdots \\ g_l(\mathbf{X}_N) \end{bmatrix}, \tag{3.56}$$

and

$$\begin{bmatrix} \Psi_1(\mathbf{X}_1) & \dots & \Psi_{J_{q-r}}(\mathbf{X}_1) \\ \Psi_1(\mathbf{X}_2) & \dots & \Psi_{J_{q-r}}(\mathbf{X}_2) \\ \vdots & \ddots & \vdots \\ \Psi_1(\mathbf{X}_{N'}) & \dots & \Psi_{J_{q-r}}(\mathbf{X}_{N'}) \end{bmatrix} \begin{bmatrix} a_{\delta,1} \\ a_{\delta,2} \\ \vdots \\ a_{\delta,J_{q-r}} \end{bmatrix} = \begin{bmatrix} \delta(\mathbf{X}_1) \\ \delta(\mathbf{X}_2) \\ \vdots \\ \delta(\mathbf{X}_{N'}) \end{bmatrix}, \tag{3.57}$$

where J_q is the number of the orthogonal polynomials for the sparse grid level q and N is the number of collocation points at this level. N' is the number of collocation points for sparse grid level $q - r$. Note that the collocation points are determined based on the sparse grid level, hence N' is smaller than N. The two sets of coefficients $\mathbf{a}_l$ and $\mathbf{a}_\delta$ are estimated by the least-squares method as:

$$\mathbf{a}_l = \underset{\mathbf{a}_l \in \mathbb{R}^{J_q}}{\operatorname{argmin}} \sum_{i=1}^{N} \{g_l(\mathbf{X}_i) - \mathbf{a}_l^T \mathbf{\Psi}(\mathbf{X}_i)\}^2, \tag{3.58}$$

and

$$\mathbf{a}_\delta = \underset{\mathbf{a}_\delta \in \mathbb{R}^{J_{q-r}}}{\operatorname{argmin}} \sum_{i=1}^{N'} \{\delta(\mathbf{X}_i) - \mathbf{a}_\delta^T \mathbf{\Psi}(\mathbf{X}_i)\}^2. \tag{3.59}$$

As the low-fidelity simulations are carried out for both sparse grid level q and $q - r$, care was taken to ensure that the collocation points are nested between each level, reducing the computational expense of the method.

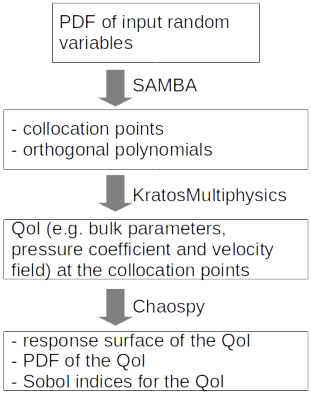

Figure 3.3: Flowchart and software usage for NIPC

3.3 Software management

A flowchart of the MF-NIPC is shown in Fig. 3.3. First the PDF of the input random variables are determined by expert's knowledge, literature review and/or experimental data. The PDF can be expressed either by functions or histograms. Based on the decided PDF, the collocation points and the optimal orthogonal polynomials are calculated using aPC by SAMBA. Then, CFD models are set up for running CFD simulations at the collocation points in KratosMultiphysics. It should be noted that there is still no interface programs between SAMBA and KratosMultiphysics. After the CFD simulations are finished, the preprocess is carried out by open source python code Chaospy (Feinberg et al. [47]). In this way, UQ methods and CFD simulations are carried out completely separately. This can take advantage of existing CFD code.

3.4 Example: Low Reynolds number flow around a rectangular cylinder

In this section, the introduced multi-fidelity NIPC is demonstrated for low Reynolds number flow around a rectangular cylinder problem with the Reynolds number is set to 400. The Reynolds number 400 is very low as a CWE problem, however it is much faster to converge and appropriate as a demonstration case and the objective of this section is to demonstrate the introduced MF-NIPC. CFD simulations are solved by the software Kratos-Multiphysics, as a turbulence modelling LES is used. LES usually should be calculated in three dimensions for high Reynolds number flow, however in

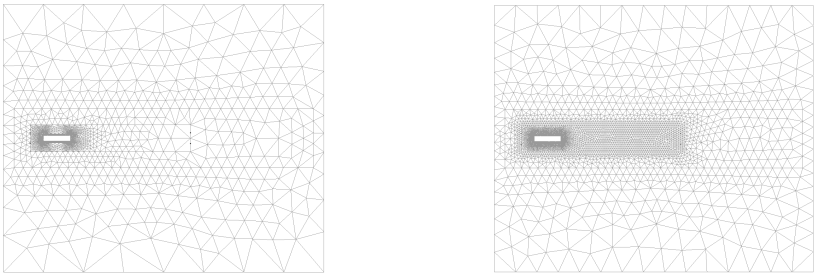

(a) (b)

Figure 3.4: Details of the fine and coarse meshes used

this section two dimensional simulation is used because of its low Reynolds number. For performing MF-NIPC, a coarse mesh as low-fidelity model and a fine mesh as high-fidelity model are created. It is noted that the multi-fidelity framework with different meshes are also called as multi-level framework. The meshes are shown in Fig. 3.4. The coarse mesh has 7956 and the fine mesh has 22,313 cells. Time steps are determined by performing convergence study, $dt = 3.0$[s] for the coarse mesh and $dt = 1.5$[s] for the fine mesh are used respectively. The simulations are carried out until $30,000$[s] and time statistics are calculated by results after $15,000$[s]. About boundary conditions, the inflow velocity is applied to left wall, no-slip condition at the cylinder surface and slip condition at far-field are imposed.

The resulted time statistics of aerodynamic coefficient C_d, C_l and the Strouhal number S_t are compared with ones in Hourigan et al. [68]. In Hourigan et al. [68], the flow at $R_e = 400$ is solved by the finite element method. C_d, C_l are calculated as:

$$C_d = \frac{2F_d}{\rho {U_{inlet}}^2 D} \qquad C_l = \frac{2F_l}{\rho {U_{inlet}}^2 B},$$

where F_d, F_l are the drag and lift force subjected to the structure, $\rho = 1.225 kg/m^3$ is the density of the air, U_{inlet} is the applied inlet velocity, B is the chord length and D is the thickness of the structure. The Strouhal number is calculated as $S_t = fB/U_{inlet}$, where f is the frequency of the lift force coefficient. In Table 3.1 the time averaged C_d ($: t - avr(C_d)$) and time standard deviation of C_l ($: t - std(C_l)$) are compared. It can be seen that the fine mesh gets very close values as Hourigan et al. [68]. The coarse mesh also got very close value of C_d with the one from the literature and the fine mesh, on the other hand there is more difference in C_l and S_t value between results of the fine- and coarse mesh. It is assumed that the angle of attack has a normal distribution with mean 0.0° and standard deviation 3.0°, and the curvature has a half normal distribution with the location parameter 0.0 and the scale parameter 0.05. Fig. 3.6 shows collocation points for sparse grid level 1 to 3 calculated by SAMBA.

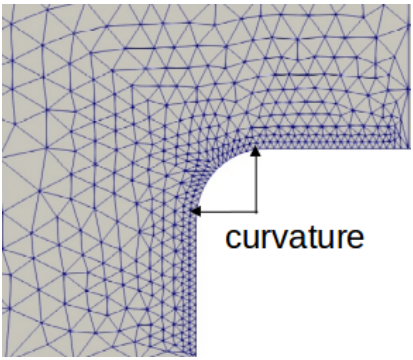

Figure 3.5: Definition of the curvature

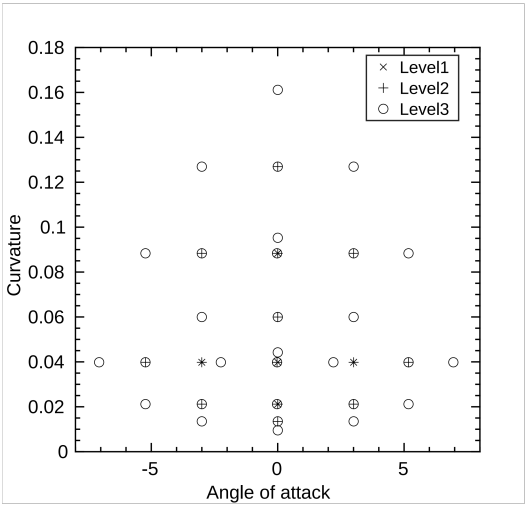

Figure 3.6: The collocation points for the sparse grid level 1 to 3

CFD model	$t - avr(C_d)$	$t - std(C_l)$	S_t
Hourigan et al., 2001	1.12	0.216	0.55
Coarse mesh	1.03	0.0724	0.75
Fine mesh	1.00	0.206	0.56

Table 3.1: Comparison of time statistics of the aerodynamics coefficient and Strouhal number

Fig.3.7 shows PDF outlines of $t - avr(C_d)$ and $t - std(C_l)$ computed by single fidelity model of the coarse mesh with the level 3 and the fine mesh with the level 3, and the multi-fidelity model of the coarse mesh with the level 3 and the additive correction with the level 1 and level 2 using Eq.(3.54). Note that the single fidelity model of the fine mesh with the level 3 is the most accurate model. Comparing results of the single fidelity models, as can be seen in Fig.3.7(a) the shape of the PDF of $t - avr(C_d)$ computed by the coarse mesh model is different from the one of the fine mesh model. Even with the additive correction, the shape of PDF is not exactly same as the one of the fine mesh model but by using additive correction, the shape of PDF gets closer to the one computed by the fine mesh model only. In Fig.3.7(b) the locations of the PDFs of $t - std(C_l)$ are different between the ones of the coarse mesh with level 3 and the fine mesh with level 3. By applying the additive correction, location and shape of PDF gets similar as the PDF evaluated by the fine mesh only. In the case of both $t - avr(C_d)$ and $t - std(C_l)$, it can be confirmed that by increasing the level of the additive correction, the shape of PDF tends to converge to the shape of the PDF computed by the fine mesh model only.

Figure 3.8 and 3.9 show the statistic moments, which are mean, standard deviation, skewness and kurtosis, computed by the single fidelity model of the coarse mesh with the level 1 to level 3 and the fine mesh with the level 1 to level 3 respectively, and the multifidelity model of the coarse mesh with level 3 and the additive correction level 1 and level 2. The horizontal axis is the total calculation time and the unit t_0 is the calculation time of a coarse mesh deterministic simulation. The ratio of calculation time of the fine mesh deterministic simulation to the one of the coarse mesh deterministic simulation is 2, which is determined by averaging actual calculation time of deterministic simulations. It can be seen that except skewness and kurtosis of $t - std(C_l)$, the statistic moments computed by the fine mesh model and the multifidelity model converge to almost same value, while the ones of the coarse mesh converges to different value. Comparing total calculation time of the single fidelity model of the fine mesh and the multifidelity model, the convergence speed is faster by the single fidelity model of the fine mesh than by the multifidelity model. It happens because in this case the computational time ratio of the fine mesh to the coarse mesh is not very high. In order to further reduce the computational time of low-fidelity, it might help to use different turbulence model such as URANS, which will be further investigated in this thesis.

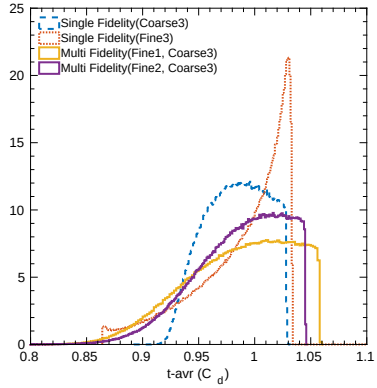

(a)

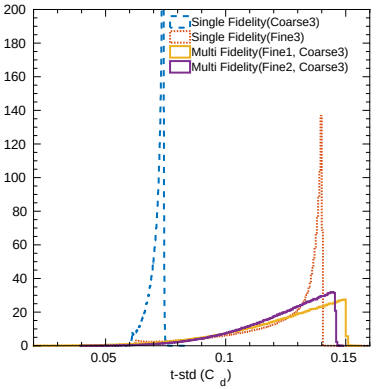

(b)

Figure 3.7: The PDF outlines of (a) $t - avr(C_d)$ and (b) $t - std(C_l)$ computed by the single fidelity model (the coarse mesh level 3, the fine mesh level3) and the Multi-fidelity model (the coarse mesh level, the fine mesh level) = (3,1),(3,2))

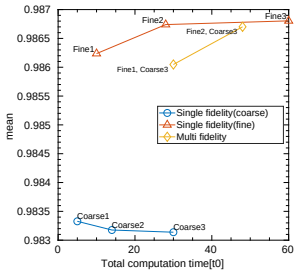

(a) Mean

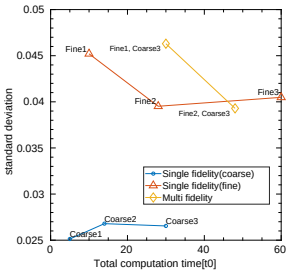

(b) Standard deviation

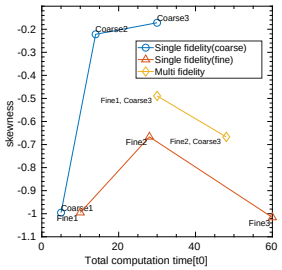

(c) Skewness

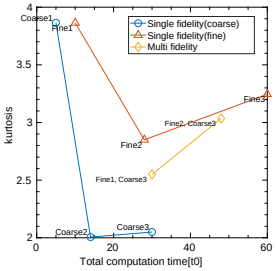

(d) Kurtosis

Figure 3.8: The moment convergence of $t - mean(C_d)$

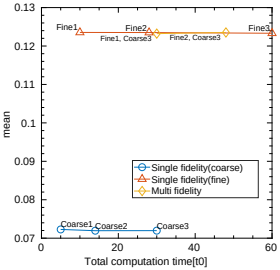

(a) Mean

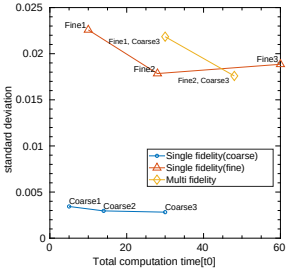

(b) Standard deviation

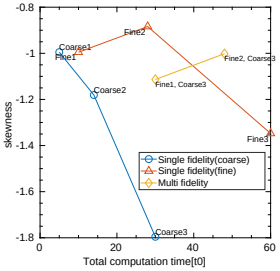

(c) Skewness

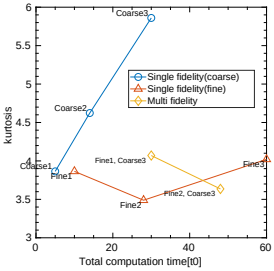

(d) Kurtosis

Figure 3.9: The moment convergence of $t - std(C_l)$

	$t - avr(C_d)$	$t - std(C_l)$
Correlation	0.984	0.988
Mean Absolute Relative Error	0.0207	0.360

Table 3.2: The correlation and the mean absolute relative error between the coarse- and the fine mesh models

	mean	mean ± standard deviation	Deterministic result
$t - avr(C_d)$	0.986	(0.940, 1.032)	1.03
$t - std(C_l)$	0.123	(0.101, 0.145)	0.206

Table 3.3: The comparison between the stochastic result and the deterministic result

For comparing deterministic results of the coarse mesh and the fine mesh, Table 3.2 shows the correlation and the mean absolute relative error, which are calculated from 35 deterministic results used for NIPC of the level 1 to 3. The correlation and the mean absolute relative error are calculated as Palar et al. [110]:

$$\text{Correlation} = \left(\frac{\sum_{i=1}^{N} (g_{h_i} - \overline{g}_h)(g_{l_i} - \overline{g}_l)}{\sqrt{\sum_{i=1}^{N} (g_{h_i} - \overline{g}_h)^2} \sqrt{\sum_{i=1}^{N} (g_{l_i} - \overline{g}_l)^2}} \right)^2 \tag{3.60}$$

$$\text{MeanAbsoluteRelativeError} = \frac{1}{N} \sum_{i=1}^{N} \left| \frac{g_{l_i} - g_{h_i}}{g_{h_i}} \right| \tag{3.61}$$

where N is the number of deterministic simulations and $\overline{g}_l$ and $\overline{g}_h$ is the mean of the N observation data sets. From Table 3.2 it can be seen that $t - avr(C_d)$ is predicted well by the coarse mesh, while $t - std(C_l)$ has 36.6% error. The correlation values are similar in $t - avr(C_d)$ and $t - std(C_l)$. Even though the coarse mesh cannot predict $t - std(C_l)$ well, the multifidelity NIPC is able to get a similar PDF to the one computed by fine mesh only. Finally, let us think about the results of the multi-fidelity model of the coarse mesh with level 3 and the discrepancy model with level 1. Table 3.3 compares the stochastic result of the multifidelity model and the deterministic result of the fine mesh with angle of attack 0.0° and the curvature 0.0. For $t - avr(C_d)$, the result of deterministic simulation is close to the mean value of the stochastic results. On the other hand, $t - std(C_l)$ has different feature. The deterministic result and the stochastic result are very different. In addition the standard deviation of the $t - std(C_l)$ is 17.7% of the mean value, that is $t - std(C_l)$ has unignorable variation due to input uncertain parameters, the angle of attack and the curvature. $t - std(C_l)$ is caused by flow separation at the leading- and trailing edges and it is physically understandable that the geometry of

the edges influences results of $t - std(C_l)$. The stochastic results confirmed that uncertainty of the curvature causes large variation of $t - std(C_l)$ and it is important to take into account the geometric variations in the design procedure. A problem of consideration of the curvature is that, the flow phenomenon has large difference between without curvature and with a curvature even as small as 0.01 which is the smallest curvature in the calculated collocation points. This results in that $t - std(C_l)$ calculated by the deterministic simulation with the curvature 0.0 is not included in the stochastic result of $t - std(C_l)$.

Conclusion

From this demonstration case we can conclude that, by an additive correction, the shape of PDF of $t - mean(C_d)$ and the shape and position of PDF of $t - std(C_l)$ are improved. By applying the additive correction, the statistic moments of QoIs converge to the similar value as the ones calculated by the single fidelity model of the fine mesh, while the statistic moments calculated by the single fidelity model with the coarse mesh does not converge. Finally we observed that the uncertainty of the angle of attack and the curvature causes variation to the time statistics of the lift- and drag coefficients, especially $t - std(C_l)$.

In next chapters we will apply the successfully demonstrated MF-NIPC to flow with high Reynolds number which is more realistic case in civil engineering.

Chapter 4

Application of MF-NIPC to homogeneous inflow problems

In this chapter an application of the MF-NIPC to a homogeneous inflow problem is introduced. As a homogeneous inflow problem the Benchmark on Aerodynamics of a Rectangular 5:1 Cylinder (BARC) problem is considered. BARC problem is a well-documented benchmark case studied by both CFD simulation and wind tunnel tests. In this chapter, first literature about BARC are reviewed in the introduction. Then the input random variables are determined from literature and the collocation points for NIPC are calculated. Afterwards, the settings of two different fidelity models, namely: LES simulations and URANS simulations are introduced, and deterministic results from both models are compared for validation. Finally the MF-NIPC is applied to the BARC problem. The accuracy of the MF-NIPC is investigated by comparing Probability Density Function (PDF) estimated by different models, and then the stochastic results calculated by MF-NIPC are compared with wind tunnel experiment results.

4.1 Introduction: Benchmark on Aerodynamics of a Rectangular 5:1 Cylinder

Rectangular shape plays an important role in architectural design. Many civil and industrial structures are characterized by rectangular shapes. While the geometry of the cylinder is simple, the wind-structure interaction of a rectangular cylinder can exhibit behaviour such as boundary layer separation and reattachment. For these reasons the BARC problem has been widely investigated both by CFD simulations and wind tunnel tests. The BARC problem represents the flow around two-dimensional rectangular cylinder prob-

lems. It has been known that the ratio of the along-wind dimension (Breadth, B) to the crosswind dimension (Depth, D), B/D governs the characteristic of the flow around rectangular cylinders (Nakaguchi et al. [101]). In case of B/D $>$ 3.5 it is expected that reattachment is permanent and the vortex shedding occurs from both the leading and trailing edges, though for the smaller B/D the reattachment is intermittent. The BARC problem is promoted with the aim of investigating assessing the consistency of the CFD simulations and the wind tunnel experiments for a case with B/D = 5.0. *a Benchmark on the Aerodynamics of a Rectangular 5:1 Cylinder* [1] recommends following conditions in addition to B/D = 5.0.

- Reynolds number: $2 \times 10^4 \leq Re = UD/\nu \leq 8 \times 10^4$
- Angle of incidence: $\alpha = 0^\circ$
- Turbulence intensity: $I_u \leq 0.01$
- Radius of curvature of the model edges: $r/D \leq 0.025$
- Sampling frequency. $f_{sam}D/U \geq 8St_D$

All the recommended setting for the BARC problem may be found in *a Benchmark on the Aerodynamics of a Rectangular 5:1 Cylinder* [1]. Bruno et al. [22] summarize CFD simulations and wind tunnel tests carried out following the BARC problem recommendations and statistically analyzed results such as drag- and lift coefficient, Strouhal number and pressure coefficient distributions. A number of works have focused on the problem of validating CFD simulations on the BARC test case through a comparison with experimental wind tunnel tests. Bruno et al. [21] carried out LES simulation based on Finite Volume method based software. It investigated three dimensional feature of vortex shedding around the rectangular cylinder. Mannini et al. [89] carried out URANS simulations using different turbulence modelling and compared the results with results of wind tunnel tests. Mannini et al. [88] carried out Detached-Eddy simulations (DES) which is the hybrid RANS and LES methods. RANS methods are used at the near wall region, where usually very fine mesh refinement is required and LES methods are used otherwise. It compared the results of DES with URANS results shown in Mannini et al. [89]. About the wind tunnel tests for BARC problem, Schewe [135] carried out wind tunnel test for low Reynolds number 2×10^4 and high Reynolds number 2×10^6, with angle of incidence 0° and 4°, in order to see the effect of Reynolds number and angle of intensity to bulk parameters. Bronkhorst et al. [18] carried out the wind tunnel tests with Reynolds number 5.0×10^4 and changing the angle of incoming flow. It also investigated effect of corner treatment by changing the material at the corner of the rectangular cylinder. Wind tunnel tests are subject to uncertainty and Bronkhorst et al. [18] pointed out possible sources of the uncertainties, such as: a disturbance in the oncoming flow, a misalignment of the model, an asymmetry in the flow, corner insert elements, pressure taps, and quality of the rectangular shape of the model. A number of recent works have employed Uncertainty Quantification (UQ) techniques in order to account for the irreducible uncertainties present in wind tunnel tests on the BARC geometry

in CFD simulations. For example, Mariotti et al. [92] used URANS as a turbulence model and considered the uncertainties associated with the angle of incidence, the longitudinal turbulence intensity, and the turbulence length scale. Mariotti et al. [93] used LES for their CFD simulations and instead considered the effect of uncertainties arising from the parameters of the CFD simulations, namely: the grid resolution and the weight associated with the turbulence model filter. Witteveen et al. [163] conducted an uncertainty study on the angle of attack, the longitudinal turbulence intensity and the turbulence length scale with two-dimensional URANS simulations. Finally, Rocchio et al. [130] considered the effect of uncertainties associated with the curvature radius of the rectangular cylinder corners using LES simulations. A significant challenge for conducting an uncertainty analysis on the flow around a rectangular cylinder is the required computational cost. The flow around the rectangular cylinder geometry with high Reynolds number requirs CFD simulations with fine mesh as well as fine time discretization. Consequently, there is significant computational cost associated with each individual CFD simulation. In this chapter, the MF-NIPC methods have been applied to the BARC problem and it is sought to validate the numerical simulation results with experimental data, by quantifying the aleatory uncertainty existing in the wind tunnel tests. As high-fidelity model LES are used and as low-fidelity model URANS are used. First each deterministic model's set up and its validation will be introduced. Afterwards the multi-fidelity results will be compared with the high-fidelity only results and the accuracy of the multi-fidelity framework will be investigated. Finally the MF-NIPC results are compared with wind tunnel experiments results and the effect of the input uncertainties are investigated.

4.2 BARC test case

The objective of this study is to quantify the effects of uncertainties in the incoming flow conditions and variations in the geometry of the structure on the time statistics of bulk parameters and pressure coefficients of the flow around a rectangular cylinder. A training data set comprising of evaluations of two CFD models is used to construct a multi-fidelity, non-intrusive Polynomial Chaos Expansion (PCE) for each of these bulk parameters and the pressure coefficients. This PCE is then validated against a scarce set of data from wind tunnel tests. In this section, we discuss the setup of the test case and give details of the two sets of CFD simulations. LES and URANS are tested without introducing curvature at edges of the rectangular cylinder and accuracy will be checked by comparing the results with ones in literature. The interested reader is referred to two studies that also validate CFD models of the BARC test case, namely: Mariotti et al. [91] and Rocchio et al. [130]. We intend to expand upon this work by incorporating a multi-fidelity approach to this problem in which the computational cost of the simulations is significantly reduced by leveraging a small set of LES simulations with a larger set of computationally cheaper, but less accurate, URANS simulations.

The Quantity of Interests (QoIs), that are mostly reported in the literature,

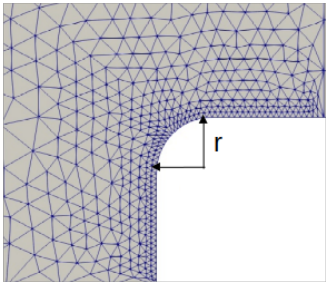

Figure 4.1: Assumption of the curvature radius at the edge of the rectangular cylinder

are the bulk parameters C_l, C_d and the pressure coefficient C_p. The lift coefficient C_l and the drag coefficient C_d are calculated as:

$$C_d = \frac{F_D}{\frac{1}{2}\rho A_D U_\infty^2} \quad C_l = \frac{F_L}{\frac{1}{2}\rho A_L U_\infty^2}, \tag{4.1}$$

where ρ is density of fluid, U_∞ is the freestream velocity of the fluid, A_D, A_L is the reference area and F_D, F_L are drag- and lift force respectively. The pressure coefficient C_p is calculated as:

$$C_p = \frac{p - p_\infty}{\frac{1}{2}\rho U_\infty^2}, \tag{4.2}$$

where p_∞ is the pressure at a reference point, ρ is the fluid density and U_∞ is the freestream velocity of the fluid. In the literature the side averaged C_p is usually reported, and in this thesis the side averaged C_p will be also used.

4.2.1 Calculation of the collocation points

In this study, the angle of attack and the curvature radius of the cylinder corners are considered to be input random variables. According to Mariotti et al. [91], the range of variation for the angle of attack is $[-1°, 1°]$, which represents small flow misalignments that are possible in wind tunnel tests. We choose to represent the angle of attack as a normal distribution with a mean of $0.0°$ and standard deviation $0.51°$. These parameters are chosen so that the angle of attack lies in $[-1°, 1°]$ with 95% confidence. Variations in the curvature radius of the cylinder corners are introduced by manufacturing errors. Assumption of the curvature radius is illustrated in Fig. 4.1. According to Rocchio et al. [130] the curvature radius r/D varies in the range $(0, 0.054)$. Here we represent the possible values of the curvature radius with a uniform distribution in $(0, 0.054)$. Collocation points are calculated by SAMBA for sparse grid levels 2 and 3. The resulting collocation points are shown in Fig. 4.2. There are 13 collocation points for the sparse grid level 2 and 30

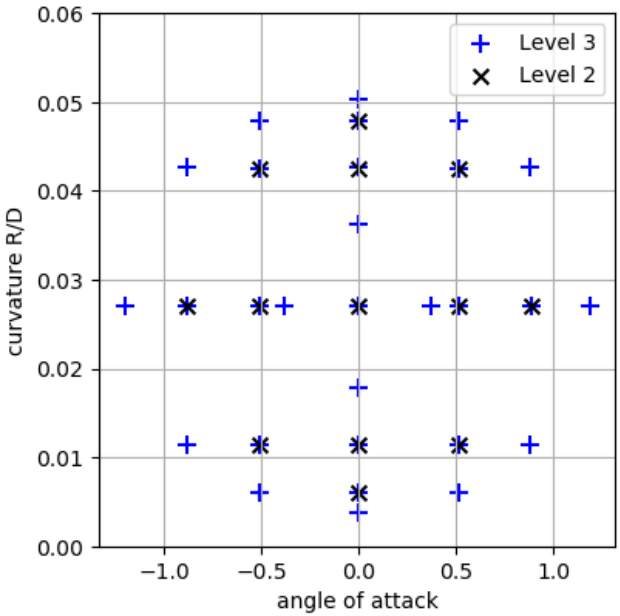

Figure 4.2: Collocation points calculated by Smolayak's algorithm at levels 2 and 3. The high-fidelity model is evaluated at the level 2 sample points, the low-fidelity model at the sample points in level 2 and level 3.

collocation points for the level 3. 11 collocation points are nested, they appear in both the level 2 and level 3 sample grids. High-fidelity LES simulations were run for each of the points in the level 2 grid, while low-fidelity URANS simulations were run for the points in the level 2 and level 3 grid. In order to change the input random variables, the curvature radius and the angle of attack, computational models should be developed carefully. At the top and bottom of the computational domain, periodic conditions are assigned instead of slip conditions. Meshes for each curvature of radius are generated using the mesh motion method based on a mesh without curvature radius. Interested readers about the mesh motion are referred to Winterstein [162].

4.2.2 High-fidelity model: Large Eddy Simulation

The computational domain and the boundary conditions of the LES simulations are shown in Fig. 4.3. The cross section of the rectangular cylinder had the along wind dimension $B = 0.5m$ and cross wind dimension $D = 0.1m$. The size of the computational domain was $(D_x, D_y, D_z) = (11B, 8B, 1B)$ and

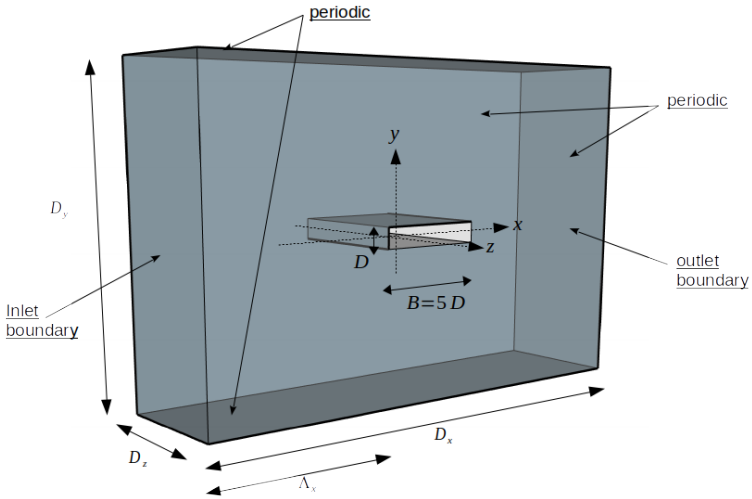

Figure 4.3: The computational domain for the LES. The axes and the boundary conditions are indicated.

the distance from the inlet boundary to the rectangular cylinder was $\Lambda_x = 4B$. Computational domain is determined according to Bruno et al. [22]. The inlet velocity was $7.5m/s$ corresponding to $Re_D = UD/\nu = 50,675$. This inlet condition was chosen so as to be consistent with the wind tunnel tests of Bronkhorst et al. [18]. The outlet boundary pressure was set to zero. The side boundaries were given periodic boundary conditions, in order to simulate an infinitely long cylinder in the z direction. The top and bottom of the domain were also given periodic boundaries, so that the angle of attack could be adjusted without changing the geometry. A no-slip boundary condition was enforced at the surface of the rectangular cylinder and no wall functions are used, the detail of wall treatment may be given later. The computational domain was spatially discretized by unstructured tetrahedral elements. The mesh for LES is shown for a case without curvature in Fig. 4.4, adjustments in the curvature of the cylinder corners required remeshing. The height of the first cell closest to the body surface Δ was $\Delta/B = 8.66e-3$. The surface meshes are refined at the edges, in order to express the curvature radius. This mesh has $2,399,943$ cells. The mesh study is given later in this section. The non-dimensional time-step size was $t^* = 0.15$ where non-dimensional time t^* was calculated as $t^* = tU_\infty/D$. The run time of the for 750 non-dimensional time and the statistical values are calculated for 650 non-dimensional time. In order to determine time window, the convergence of time averaged C_d and the time standard deviation of C_d and C_l are checked

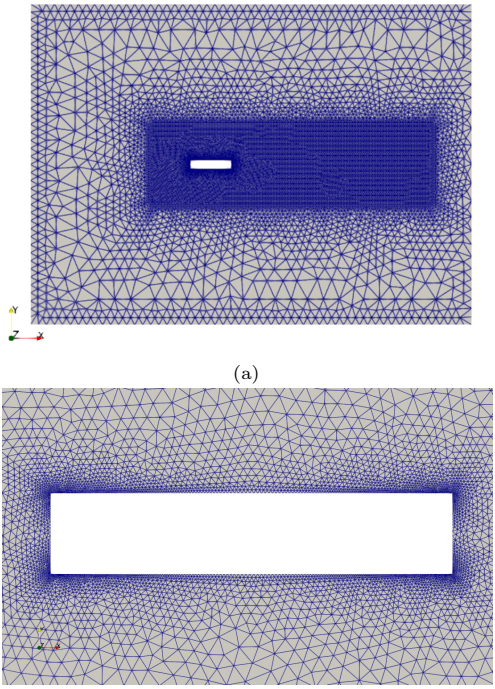

(a)

(b)

Figure 4.4: Meshing for LES (a) whole domain and (b) near-body

by sampling window as $T_1 = 50, T_n = T_{n-1} + 50$. The residual is calculated as $\phi_{res} = |(\phi_n - \phi_{n-1})/\phi_n|$. Fig. 4.5 shows time histories and the residual ϕ_{res} for each quantity of interests. It can be confirmed that if the time window is bigger than 550 non-dimensional time the standard deviation converges with the residual smaller than 2.5%. The mean value converges even with smaller time window, such as 100 non-dimensional time.

4.2.2.1 Boundary conditions for the structure

Here the cases with- and without the wall function are compared, in order to determine the appropriate boundary condition to the surface of the rectangular cylinder. Two simulations with different boundary surface condition, namely:slip condition + the wall function and the no-slip condition, are carried out with the mesh shown in Fig. 4.4. Except for the wall boundary conditions, the boundary conditions are same as illustrated in Fig. 4.3. Fig. 4.6 shows the side-averaged, span-wise averaged and time averaged pressure coefficient distribution calculated by LES with wall function and no-slip condition. The box

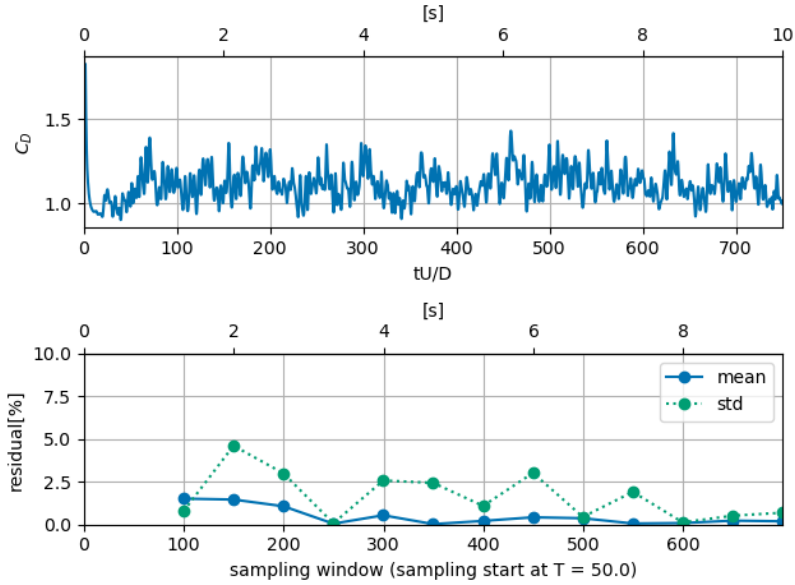

(a)

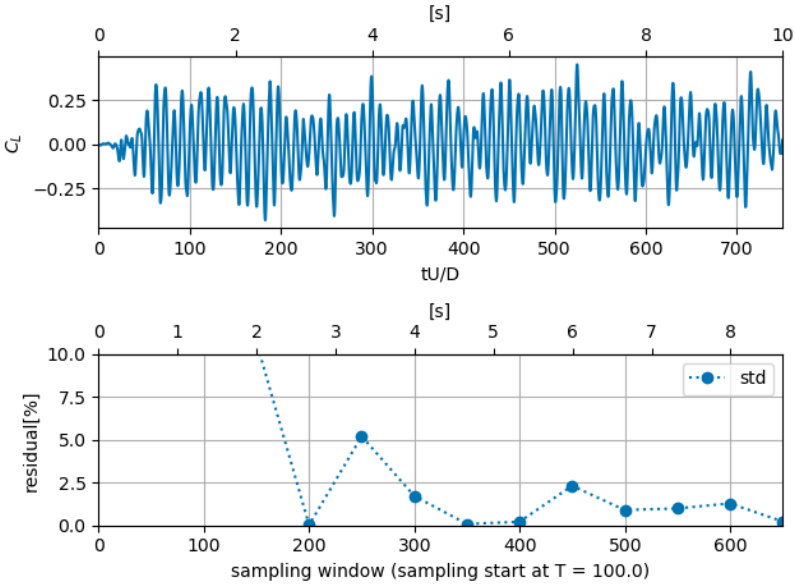

(b)

Figure 4.5: Time histories and the residual of statistics for (a) drag coefficient C_d and (b) lift coefficient C_l

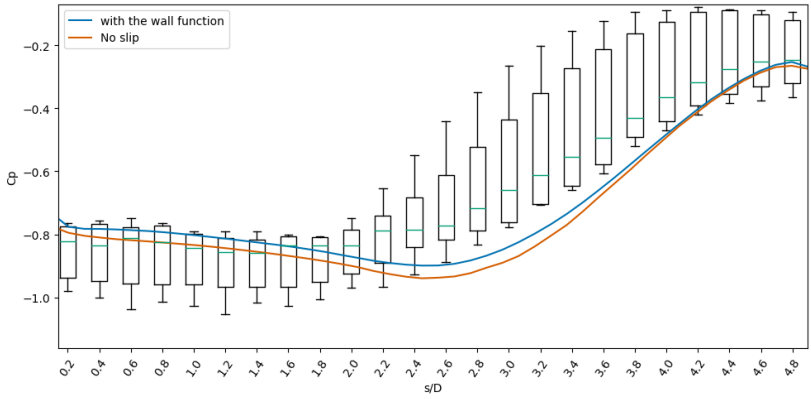

Figure 4.6: The side-averaged, span-wise averaged and time averaged pressure coefficient distribution: box plot of six wind tunnel tests, LES with wall function for the wall boundary condition and LES with no slip for the wall boundary condition

plot is the statistics of six wind tunnel tests (Bruno et al. [22]). y^+ calculated from the resulted reaction is $y^+ \approx 44$ for the no-slip case and $y^+ \approx 25$ for the wall function case. Though the range of y^+ is larger than the height of the viscous sublayer, which is known as $y+ \approx 11$(Durbin et al. [41]), the pressure coefficient distributions are very similar in both cases. It has been known that VMS, which is used as a stabilization method in KratosMultiphysics, is able to simulate the flow with coarse mesh due to numerical dissipation generated by VMS (Wornom et al. [165] and Ouvrard et al. [108]). By using the wall function degree of freedom increases and it takes more computational effort than with no-slip condition. Since computational costs play an important role for UQ, no slip conditions are used for the wall boundary conditions.

4.2.2.2 Mesh study

To create mesh the computational domain is divided to two regions as shown in Fig. 4.7. The mesh is further refined in the box which has size $(7B, 2B, 1B)$. Mesh study is carried out for with- and without curvature cases.

without curvature For the mesh study without curvature, three meshes are tested. In the fine mesh the cell size of the outer box is $\Delta/B = 0.1$ and the inner box $\Delta/B = 0.05$. In the middle mesh cell size of the outer box is kept same as the fine mesh and the cell size of the inner box is set as $\Delta/B = 0.1$. In the coarse mesh the cell size of the outer box is $\Delta/B = 0.2$ and the inner box $\Delta/B = 0.1$. The fine mesh has $3,082,547$ cells, the medium mesh has $2,099,458$ cells and the coarse mesh has $1,376,288$ cells. Fig. 4.8 compares

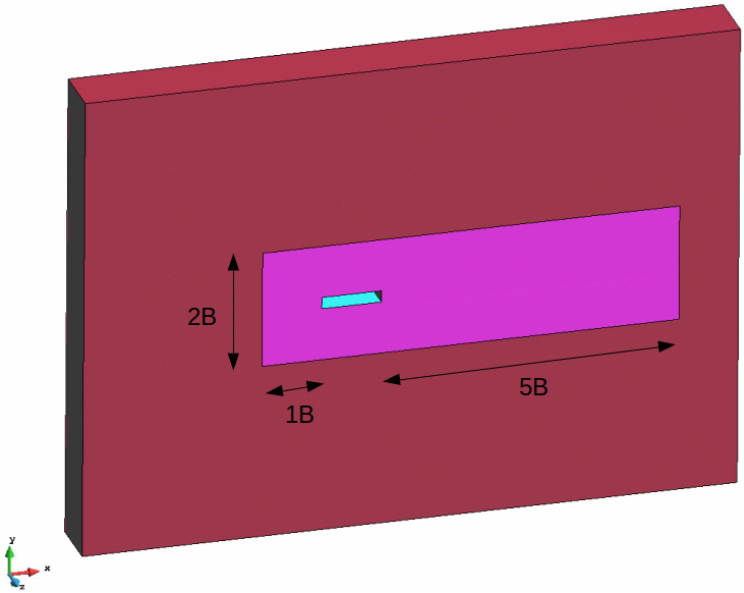

Figure 4.7: 3D computational domain for LES simulations. The refined box and its size is indicated.

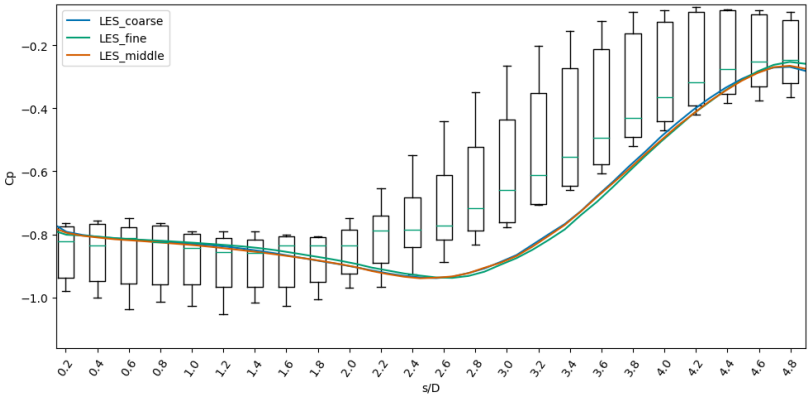

Figure 4.8: The side-averaged, span-wise averaged and time averaged pressure coefficient distribution: box plot of six wind tunnel tests, LES calculated with the fine mesh, the medium mesh and the coarse mesh

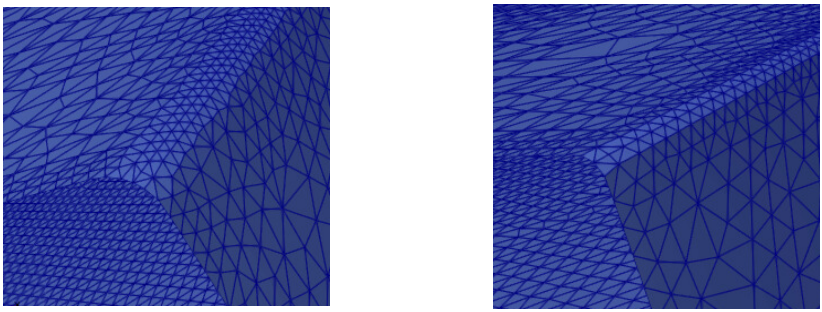

(a) (b)

Figure 4.9: Meshing for LES mesh study with curvature (a) fine (b) coarse

the pressure coefficient calculated by each mesh and from this result it is confirmed that all meshes converge to the same result. For the UQ study, the medium mesh is used.

with curvature For mesh study with curvature, two meshes are tested for a reference curvature. As the reference curvature, $r/D = 0.027$ is used. The reference curvature is the mean value of the input random variable. In the fine mesh the edges are refined, so that the curvature is discretized with 5 cells, and in the coarse mesh it is discretized with 2 cells. Each meshing is shown in Fig. 4.9. The fine mesh has $2,399,943$ cells and the coarse cells has $691,517$ cells. The pressure coefficients are compared in Fig. 4.10. The pressure coefficients are slightly different at both edges, however the results are almost converged in two types of meshes otherwise. Since curvature varies from $r/D = 0.0061$ to $r/D = 0.048$, the fine mesh is used, in order to express the minimum curvature.

4.2.3 Low-fidelity model: Unsteady Reynolds Averaged Navier-Stokes simulation

URANS simulations with a k-ω SST turbulence model were carried out in two dimensions and were used as a low-fidelity model in the multi-fidelity framework. The size of the computational domain was $(D_x, D_y) = (19.5B, 8B)$ and the distance from inlet boundary to the rectangular cylinder, $\Lambda_x = 4B$. The computational domain was made longer in along wind dimension than the one for LES, since URANS variables such as turbulent kinetic energy need relatively long domain to dissipate before reaching the outlet boundary for numerical stability. At the inlet boundary the turbulence intensity 0.01 and the turbulent mixing length $10.0m$ are given. The directions of inlet velocity are changed depending on the value of the collocation points. The computational domain was spatially discretized by unstructured triangle elements. The mesh

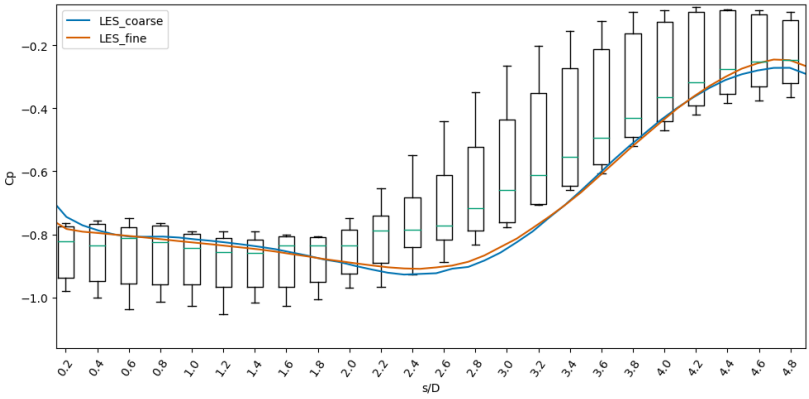

Figure 4.10: The side-averaged, span-wise averaged and time averaged pressure coefficient distribution: box plot of six wind tunnel tests, LES with the reference curvature $R/D = 0.027$ calculated with the fine mesh and the coarse mesh

for URANS is shown in Fig. 4.11. The height of the first cell closest to the body surface is $\Delta/B = 8.66e-3$. The mesh size is determined so that it is possible to express the difference of the curvature radius. The surface of the rectangular cylinder is considered as no-slip. This mesh has $69,594$ cells. The non-dimensional time-step size is $t^* = 0.075$. The time-step size is smaller in URANS than LES, because the size of cells around the rectangular cylinder is smaller in URANS. The statistical convergence was checked for the time-averaged drag coefficient as in LES, and 225 non-dimensional time is used as the time window. As seen in Fig. 4.12, results of URANS is periodic and statistical values converge much faster than LES.

4.2.3.1 Boundary condition for the structure

The dimensionless wall distance $y+$ is calculated from the resulted reaction, and $y+ \approx 7$ around the structure. Since the first node locates in the viscous sublayer, the no-slip condition is used around the structure. In order to apply the no-slip condition to the SST $k-\omega$ model, the velocity and the turbulence kinetic energy k is set to zero. The turbulent specific energy dissipation rate ω is set to value which is calculated by Menter [95] as:

$$\omega = \frac{6\nu}{\beta_1(\Delta y)^2}, \tag{4.3}$$

where ν is the kinematic viscosity, β_1 is a constant $\beta_1 = 0.0750$ and Δy is the distance to the first node from the no-slip boundary.

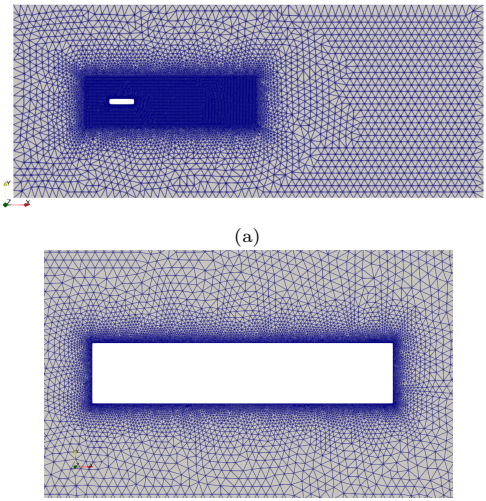

(a)

(b)

Figure 4.11: Meshing for URANS (a) whole domain and (b) near-body

4.2.3.2 Mesh study

To create mesh the computational domain is divided to two regions as shown in Fig. 4.13. The mesh is further refined in the box which has size $(7B, 2B)$. Mesh study is carried out for with- and without curvature cases as for the LES simulations.

without curvature For the mesh study without curvature, two meshes are tested. In the fine mesh the cell size in the outer box is $\Delta/B = 0.3$ and the inner box is $\Delta/B = 0.03$. In the coarse mesh the cell size in the outer box is kept same and the cell size of the inner box is set to $\Delta/B = 0.06$. The fine mesh has $69,594$ cells and the coarse mesh has $40,592$ cells. Fig 4.14 compares the pressure coefficient calculated by each mesh. From this results it is confirmed that the results are converged for both meshes. However, as mentioned above the mesh should be fine enough to express curvature changes and in this study the fine mesh is chosen.

with curvature For mesh study with curvature, two meshes are tested for the reference curvature $r/D = 0.027$. In the fine mesh the meshes around the structures are discretized, so that the curvature is discretized with 7 cells, and in the coarse mesh it is discretized with 4 cells. Each mesh is shown in Fig. 4.15. The fine mesh has $70,366$ cells and the coarse mesh has $57,517$ cells. The pressure coefficients are compared in Fig. 4.16. The results from

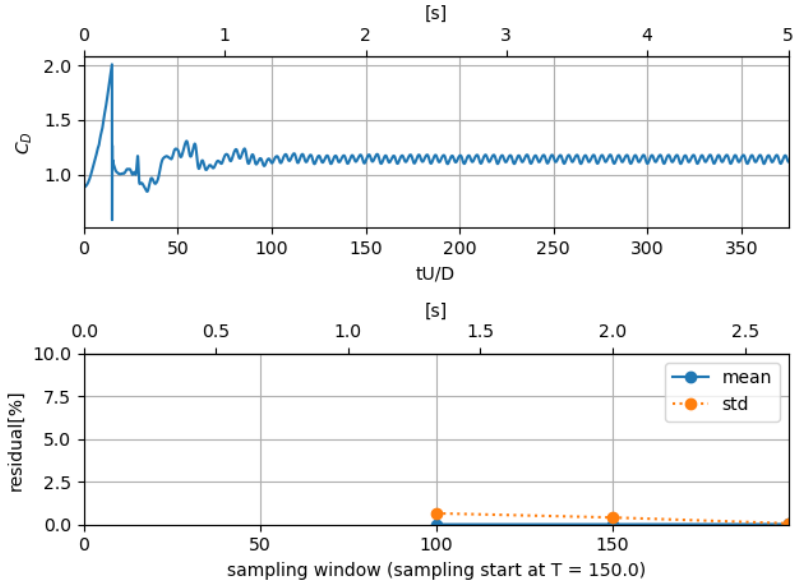

(a)

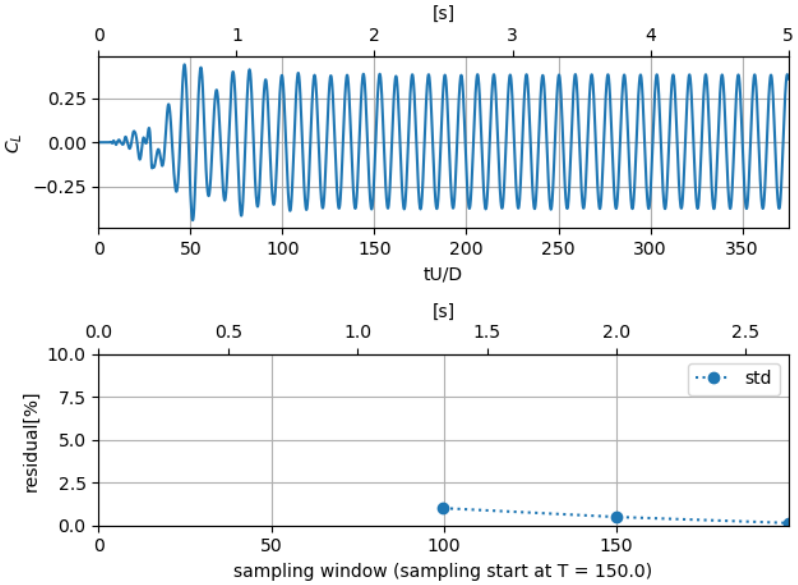

(b)

Figure 4.12: Time histories and the residual of statistics for (a) drag coefficient C_d and (b) lift coefficient C_l calculated by URANS

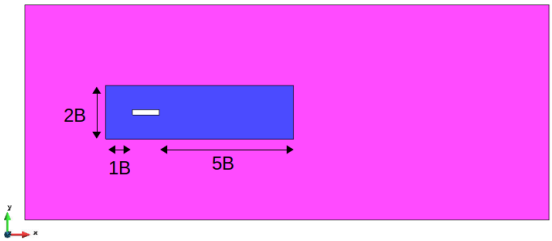

Figure 4.13: 2D computational domain for URANS simulations. The refined box and its size is indicated.

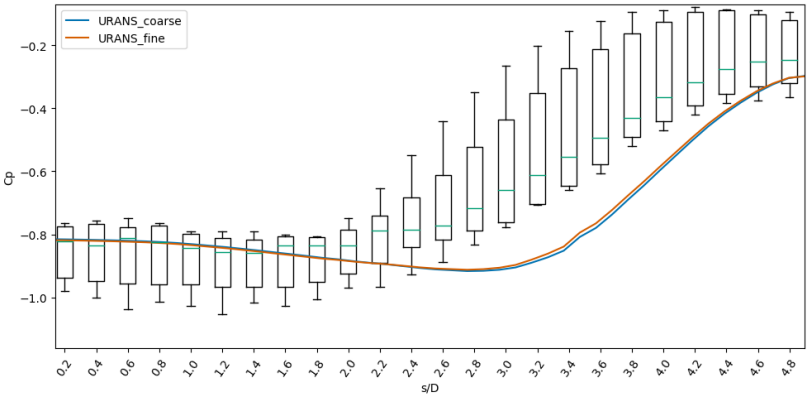

Figure 4.14: The side-averaged, span-wise averaged and time averaged pressure coefficient distribution: box plot of six wind tunnel tests, URANS calculated with the fine mesh and the coarse mesh

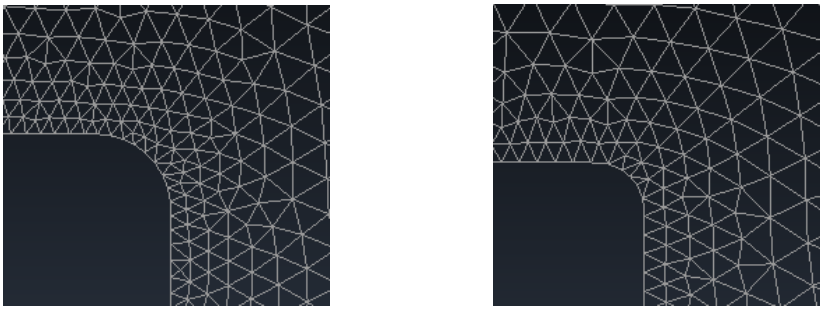

(a) (b)

Figure 4.15: Meshing for URANS mesh study with the reference curvature of (a) fine mesh (b) coarse mesh

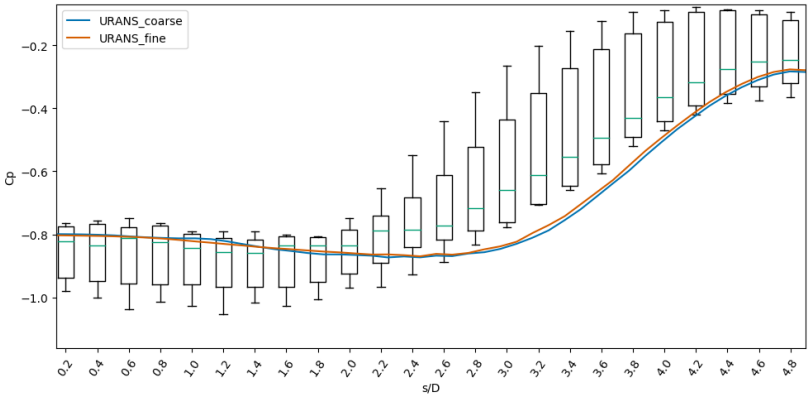

Figure 4.16: The side-averaged, span-wise averaged and time averaged pressure coefficient distribution: box plot of six wind tunnel tests, URANS with the reference curvature $R/D = 0.027$ calculated with the coarse mesh and the fine mesh

both meshes are converged, and the fine mesh is used for the UQ study, in order to express the minimum curvature.

4.2.4 Validation of deterministic results

Before carrying out UQ, LES and URANS results with curvature radius $r/D = 0.0$ and the angle of attack $= 0.0°$ were validated with results from Bruno et al. [22], in which results of both CFD and wind tunnel tests are summarized. Firstly, we compare the bulk parameters: the lift coefficient

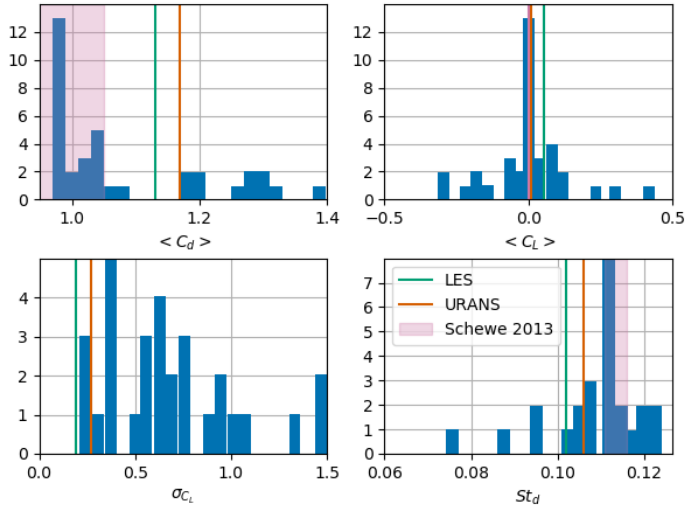

Figure 4.17: Comparison between results of LES, URANS, computational results from Bruno et al. [22] which consist of $\langle C_d \rangle$ over 36 realization, $\langle C_l \rangle$ over 36 realizations, σ_{C_l} over 30 realizations and S_t over 25 realizations and wind tunnel experiment results from Schewe [135]

	$\langle C_d \rangle$	$\langle C_l \rangle$	σ_{C_l}	St_D
LES	1.13	0.0535	0.190	0.102
URANS	1.17	0.0112	0.271	0.106

Table 4.1: Bulk parameters

C_l, the drag coefficient C_d, and the Strouhal number St_D. Table 4.1 shows the bulk parameters calculated by LES and URANS, where $\langle\rangle$ refers to time-averaged values and σ the standard deviation during a time window. In Fig. 4.17, the calculated bulk parameters are compared with values in Bruno et al. [22] and Schewe [135]. The histogram is drawn by several computational results whose detail may be found in Bruno et al. [22]. The wind tunnel experiments were carried out by Schewe [135] for $6 \times 10^3 < Re < 4 \times 10^5$. The results obtained from LES and URANS fall within the range of literature results.

For the second validation test, distributions for the time-averaged pressure coefficients $\langle C_p \rangle$ and standard deviation of the pressure coefficient $std(C_p)$ are compared. Fig. 4.18 shows the side-averaged, spanwise averaged distribution

of (a)$\langle C_p \rangle$ and (b)$std(C_p)$. The abscissa s denotes the distance from a leading edge of the structure. The box plots show the statistics of the 6 wind tunnel tests in Bruno et al. [22]. The objective here is to check the discrepancy between deterministic CFD results and wind tunnel tests, and the correlation between the high-fidelity results and the low-fidelity results.
First let us analyse the $\langle C_p \rangle$ distribution. Comparing with wind tunnel results, while both simulations capture the boundary layer separation and reattachment, both simulations underestimate recovery $\langle C_p \rangle$ in the downstream half of the top edge of the cylinder. This indicates that the CFD results have longer recirculation zones than the wind tunnel tests and consequently, the pressure increases at a slower rate along the stream wise direction in the CFD simulations compared to the wind tunnel tests. Bruno et al. [22] noted that URANS can overestimate the pressure increase and this was seen in the result of Mariotti et al. [91]. However, in our case URANS results match very well with LES results and the overestimation has not been observed. In our case URANS and LES results match very well, maybe because we use a relatively fine mesh compared to the meshes usually used for URANS simulations. In this study the mesh refinement is determined, so that it can express the change of curvature radius at each collocation point.
Now we consider the $std(C_p)$ distribution in Fig. 4.18(b). The results are almost in the range of wind tunnel tests results in the upstream side of the cylinder ($s/D < 2.5$), however in the downstream side both URANS and LES overestimate $std(C_p)$. It should be noted that compared to $\langle C_p \rangle$, $std(C_p)$ results are more variant within CFD simulations and wind tunnel tests (See for example Bruno et al. [22] and Mariotti et al. [91]). Both LES and URANS results show that $std(C_p)$ has maximum value at $s/D \approx 3.6 \sim 3.8$. In the wind tunnel tests, the maximum value occurs slightly more in the leading edge side. $std(C_p)$ of URANS shows minimum value at $s/D \approx 2.0$, which is not observed in LES results. URANS simulations which are carried out in Bruno et al. [22], Mariotti et al. [91] and Mannini et al. [89] observed the minimum value at the similar location as well, however the reason why URANS tends to show minimum value at $s/D \approx 2.0$ is still not clear. As it has been discussed, LES and URANS simulations give as same trend as wind tunnel tests both for $\langle C_p \rangle$ and $std(C_p)$, though both URANS and LES are not in the range of wind tunnel tests results in the downstream of the structure. Overall LES results and URANS results matched well both for $\langle C_p \rangle$ and $std(C_p)$. The time-averaged and spanwise averaged velocity contours are compared in Fig. 4.19. As was observed in the $\langle C_p \rangle$ distributions, the flow topology from LES and URANS was very similar and matched the streamlines shown in Bruno et al. [22]. While both the LES and URANS are generally consistent with Bruno et al. [22], as expected LES is the more accurate of the two simulations. From the plots of the velocity contours in Fig. 4.19, it can be seen that the flow reattaches faster in LES than in URANS which partly explains the discrepancy in accuracy.

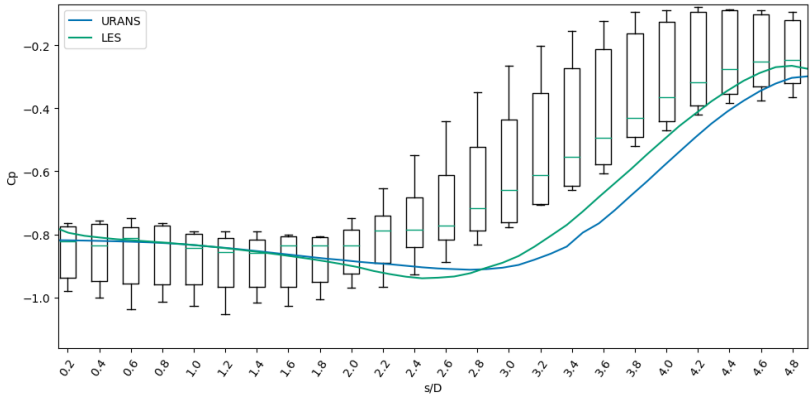

(a)

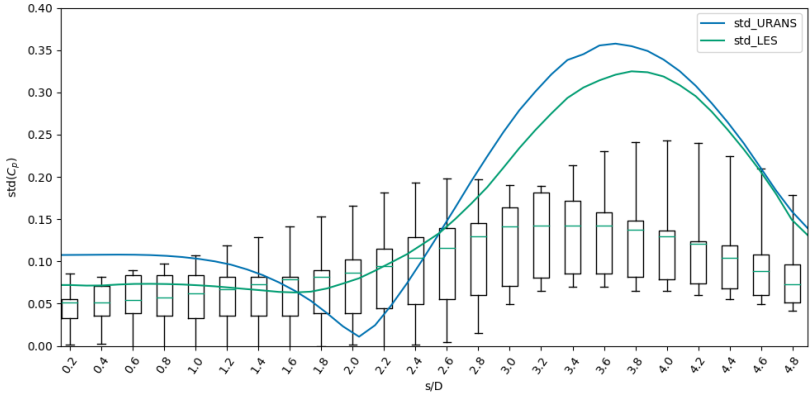

(b)

Figure 4.18: The side-averaged, span-wise averaged and time averaged pressure coefficient distribution: box plot of six wind tunnel tests, LES and URANS (a)$\langle C_p \rangle$ (b)the standard deviation of the pressure coefficient distribution $std(C_p)$

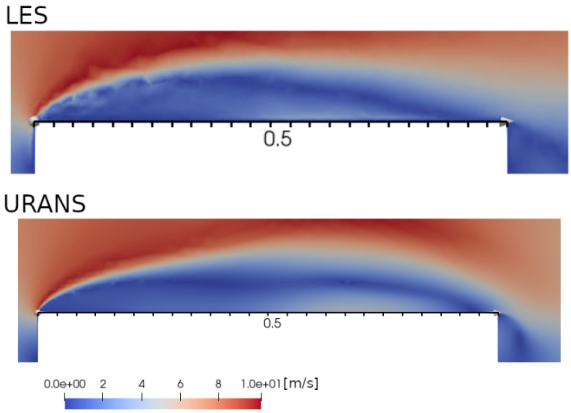

Figure 4.19: Velocity contours from the two deterministic CFD simulations.

4.3 Results: Multi-fidelity Non-Intrusive Polynomial Chaos

Having validated the setup of the two CFD methods, we now consider the multi-fidelity aspect of the study. LES simulations were run at the points in the level 2 sample grid in Fig. 4.2, while URANS simulations were run at the points in the level 2 and level 3 grid. A MF-NIPC representation of the uncertainty in the inflow conditions was derived from this data, following the method described in previous chapter. As with the deterministic simulations, the multi-fidelity framework was validated through a comparison of its predictions of the bulk parameters and then the pressure coefficient and velocity field. In the case of the bulk parameters, we compare the various computational approaches against one another, before comparing the probability distribution for the pressure coefficient estimated using MF-NIPC against experimental data from wind tunnel tests.

4.3.1 Bulk parameters

Fig. 4.20 shows a comparison between the Probability Density Functions (PDF) of the time-averaged drag and lift coefficients. PDFs were calculated using a low-fidelity PCE (URANS at level 3), a high-fidelity PCE (LES at level 2) and the multi-fidelity framework (MF-NIPC) and were compared against PDFs for the bulk parameters that were calculated from a high-fidelity PCE with coefficients estimated using LES data at level 3. Table 4.2 compares the mean and the standard deviation of the time-averaged drag and lift coefficients. Table 4.2 shows that in both instances the multi-fidelity framework is more

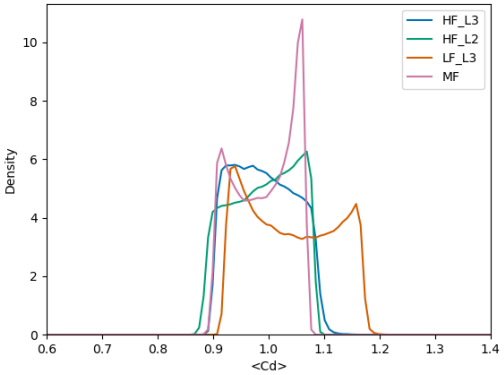

(a)

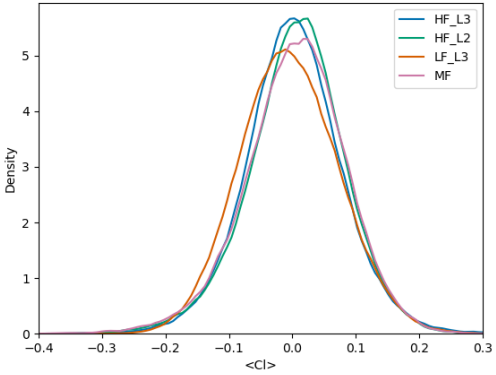

(b)

Figure 4.20: Probability Density Function of (a) $\langle C_d \rangle$ and (b) $\langle C_l \rangle$, calculated by the high-fidelity model L2(HF_L2, green), the high-fidelity model level 3 (HF_L3, blue), the low-fidelity model (LF, orange) and the multi-fidelity model (MF, pink).

		HF(L3)	absolute error from HF(L3)		
			HF(L2)	LF(L3)	MF
$\langle C_d \rangle$	mean	0.9918	0.0008	0.0474	**0.0003**
	std	0.0540	0.0028	0.0229	**0.0016**
$\langle C_l \rangle$	mean	0.0025	0.0036	0.0072	**0.0017**
	std	0.0769	**0.0001**	0.0013	0.0035

Table 4.2: Comparison of bulk parameters with different models and polynomial orders. The bulk parameters of the high-fidelity model with level 3 (HF(L3)) is presented and based on HF (L3) results the absolute error of the high-fidelity model with level 2 (HF(L2)), the low-fidelity model with level 3(LF(L3) and the multi-fidelity model (MF) is calculated. The lowest absolute error for each value are shown in bold.

accurate than both the low-fidelity and the level 2 high-fidelity PCEs taken in isolation, except the standard deviation of $\langle C_l \rangle$.

Fig. 4.21 shows the response surface calculated by the multi-fidelity NIPC and compares this surface to the location of the level 3 high- and low-fidelity collocation points. Note that there is significant discrepancy between the two sets of collocation points for the time averaged drag coefficient. It is noticeable from Fig. 4.21(a) the extent to which the response surface can be altered with MF-NIPC. However, the response surface of $\langle C_l \rangle$ is relatively linear and we would suggest that this is why the improvement of the multi-fidelity framework cannot be seen for the standard deviation of $\langle C_l \rangle$ in this particular case.

Now let us look at the time standard deviation of bulk parameters. Comparison of PDF of the time standard deviation of the bulk parameters are shown in Fig. 4.22. Compared to the time-averaged bulk parameters, there is greater discrepancy between positions of PDFs calculated by LES and URANS. Having applied the multi-fidelity framework, the mode of the PDF is improved. On the other hand, if we look at the response surfaces in Fig. 4.23, the response surfaces are not as non-linear as the response surface of the time-averaged C_d. Therefore, as it can be seen in Table 4.3, the improvement of MF compared to HF(L2) with respect to mean and standard deviation is not obvious in case for the time standard deviation of bulk parameters.

In addition to check the shape of response surface, Eldred et al. [43] calculated spectral coefficients of the PCE to compare the complexity of stochastic approximations of each model. Fig. 4.24 shows the spectral coefficients of the PCE estimated by HF(L3) and the discrepancy calculated by LES and URNAS which is used for MF framework. As we observed, $\langle C_l \rangle$ has rather simple response surface and value of the spectral coefficients are relatively small compared to ones of other QoIs. Except for $\langle C_l \rangle$, the spectral coefficient at the polynomial order 2 of the discrepancy between HF- and LF model is smaller than the spectral coefficient estimated solely by HF. From these results it can be said that PCE of the discrepancy is less complicated than PCE estimated by HF solely and the PCE of the discrepancy

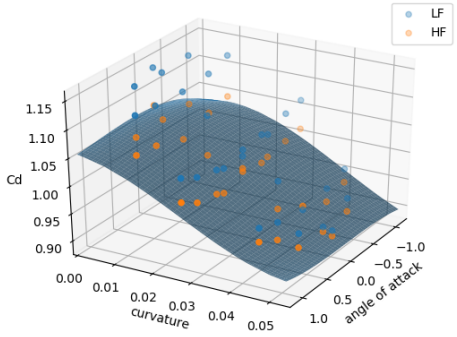

(a)

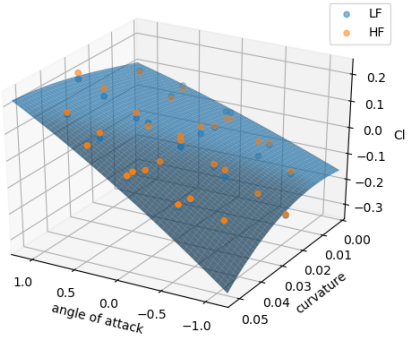

(b)

Figure 4.21: Response surface of (a) $\langle C_d \rangle$ and (b) $\langle C_l \rangle$, calculated by the the multi-fidelity model with CFD results at level 3 collocation points of the high-fidelity model (HF, orange) and the low-fidelity model (LF, blue).

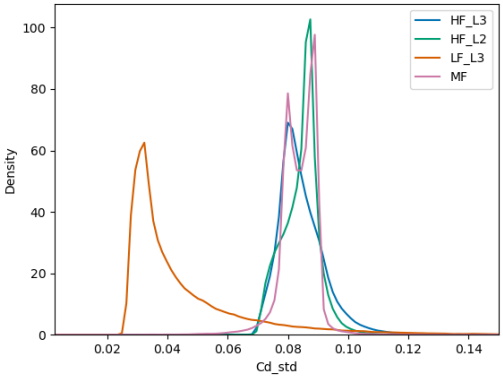

(a)

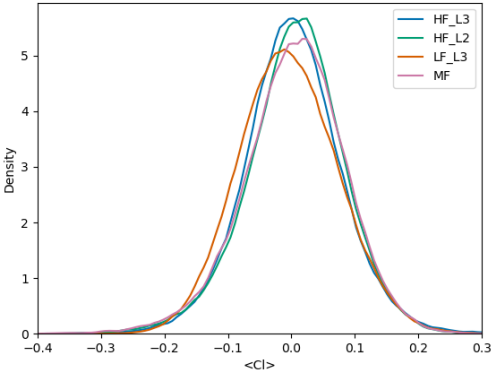

(b)

Figure 4.22: Probability Density Function of (a) $std(C_d)$ and (b) $std(C_l)$, calculated by the high-fidelity model L2(HF_L2, green), the high-fidelity model level 3 (HF_L3, blue), the low-fidelity model (LF, orange) and the multi-fidelity model (MF, pink).

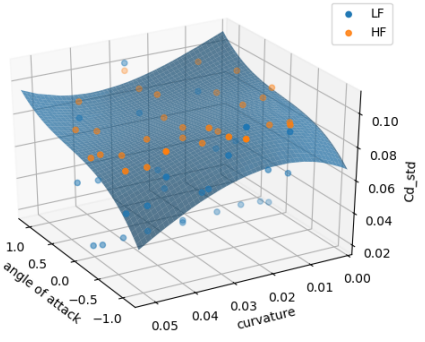

(a)

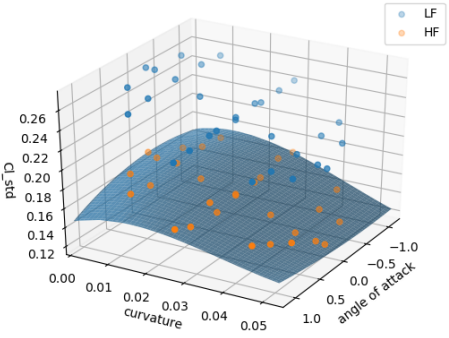

(b)

Figure 4.23: Response surface of (a) $std(C_d)$ and (b) $std(C_l)$, calculated by the multi-fidelity model with CFD results at level 3 collocation points of the high-fidelity model (HF, orange) and the low-fidelity model (LF, blue).

		HF(L3)	absolute error from HF(L3)		
			HF(L2)	LF(L3)	MF
$std(C_d)$	mean	0.0844	**0.0**	0.0389	0.0017
	std	0.0076	**0.0017**	0.015	**0.0017**
$std(C_l)$	mean	0.1554	**0.0002**	0.0808	0.0005
	std	0.0171	**0.0005**	0.0047	0.0011

Table 4.3: Comparison of standard deviation of the bulk parameters with different models and polynomial orders. The bulk parameters of the high-fidelity model with level 3 (HF(L3)) is presented and based on HF (L3) results the absolute error of the high-fidelity model with level 2 (HF(L2)), the low-fidelity model with level 3(LF(L3) and the multi-fidelity model (MF) is calculated. The lowest absolute error for each value are shown in bold.

can converge faster than the PCE of HF.

Then let us investigate correlation of URANS and LES results, by comparing the deterministic results calculated at all collocation points. Fig. 4.25 compares the LES results and the URANS results calculated at all the collocation points. The LES results and the URANS results correlate very well for $\langle C_d \rangle$ and $\langle C_l \rangle$, and for σ_{C_d} and σ_{C_l} the coefficient of determination are relatively low. This may explain why the improvement of the multi-fidelity framework is not as obvious as it is seen for $\langle C_d \rangle$ and $\langle C_l \rangle$.

Finally, computational time is compared in different models. Fig. 4.26 plot the bulk parameters calculated by different models and polynomial orders. The bulk parameters are plotted against the total CPU time. In order to carry out one simulation, URANS is simulated with 8 threads and the total CPU time of one simulation is about 400 hours. LES are calculated with 16 threads and the total CPU time of one simulation is about 1333 hours. Calculation time of URANS is relatively long compared to usual URANS simulations, since the mesh is so refined that change of curvature can be correctly visualized. As discussed above, about σ_{C_d} and σ_{C_l} HF(L2) converges to the result of HF(L3) and the improvement thanks to MF is not significant. For the $\langle C_d \rangle$ and $\langle C_l \rangle$, the improvement of MF from HF(L2) are seen.

4.3.2 Pressure coefficient

Having compared the PDFs for the bulk parameters estimated through the four computational methods against one another, we now compare the results of MF-NIPC to wind tunnel data. This comparison is made through the time-averaged pressure coefficient and the standard deviation of pressure coefficient. Fig. 4.27 compares the time-averaged- and standard deviation pressure coefficients of wind tunnel data with those predicted from MF-NIPC. The 95% confidence interval of MF-NIPC is also shown. This confidence interval was calculated using Monte Carlo sampling, referred to as the parametric bootstrap (Dubreuil et al. [40]). Let us look at the result of the time-

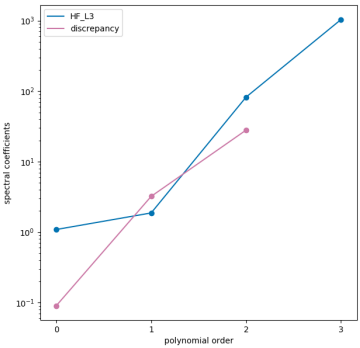

(a) $\langle C_d \rangle$

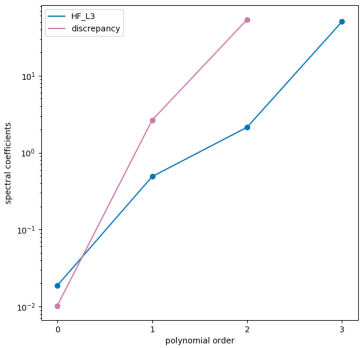

(b) $\langle C_l \rangle$

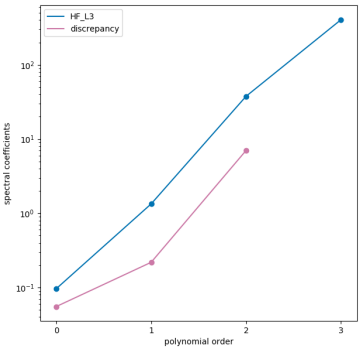

(c) σ_{C_d}

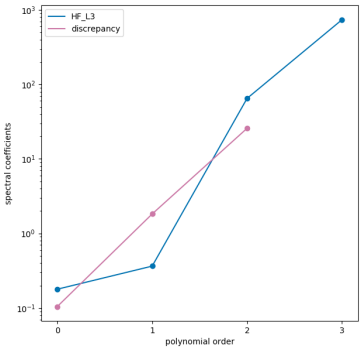

(d) σ_{C_l}

Figure 4.24: Comparison of spectral coefficient of PCE estimated by HF(L3)(:blue) and discrepancy between HF and LF(:pink).

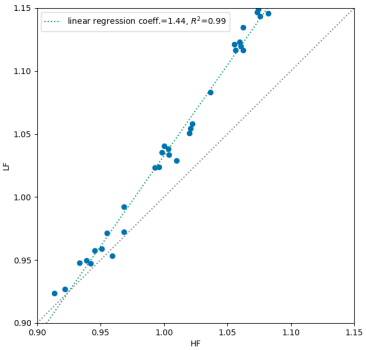

(a) $\langle C_d \rangle$

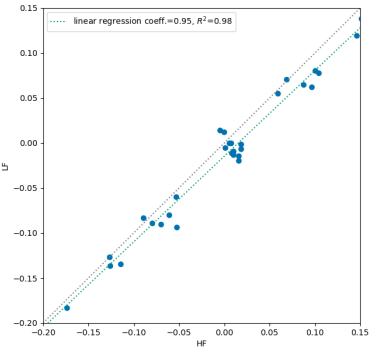

(b) $\langle C_l \rangle$

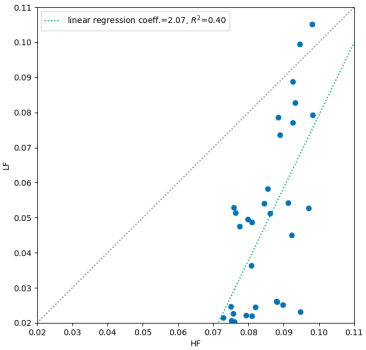

(c) σ_{C_d}

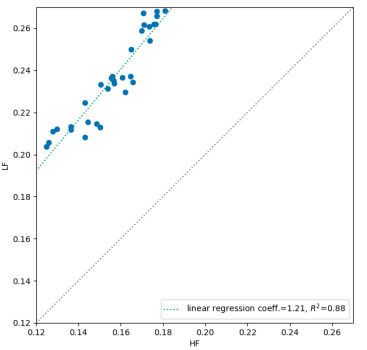

(d) σ_{C_l}

Figure 4.25: Comparison between the LES results(HF, x-axis) and the URNAS results(LF, y-axis) calculated at the collocation points for sparse grid level 2 and level 3. The linear approximation (:green) is plotted by the linear regression method. The coefficient of the linear approximation and the coefficient of determination R^2 are also shown.

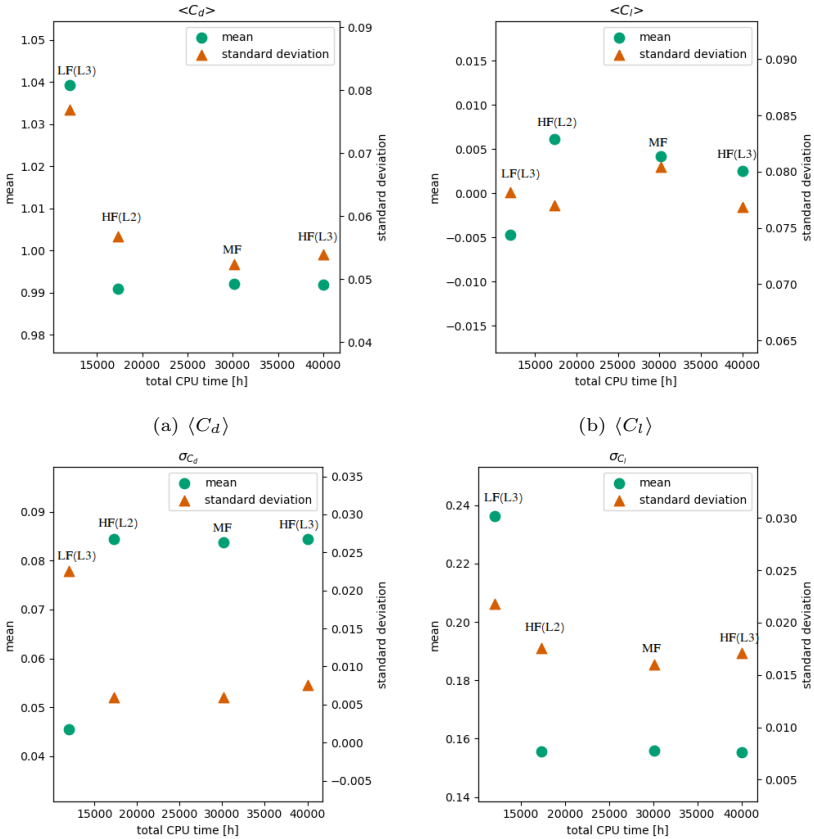

(a) $\langle C_d \rangle$ (b) $\langle C_l \rangle$

(c) σ_{C_d} (d) σ_{C_l}

Figure 4.26: Bulk parameters calculated with different models and polynomial orders. The bulk parameters are plotted against the total CPU time of each model.

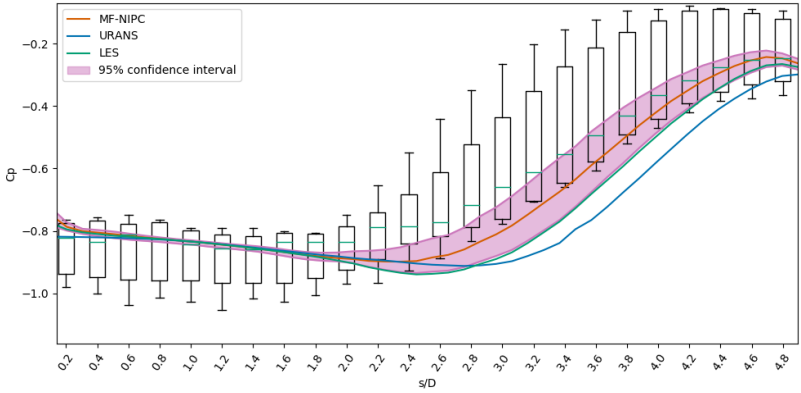

(a)

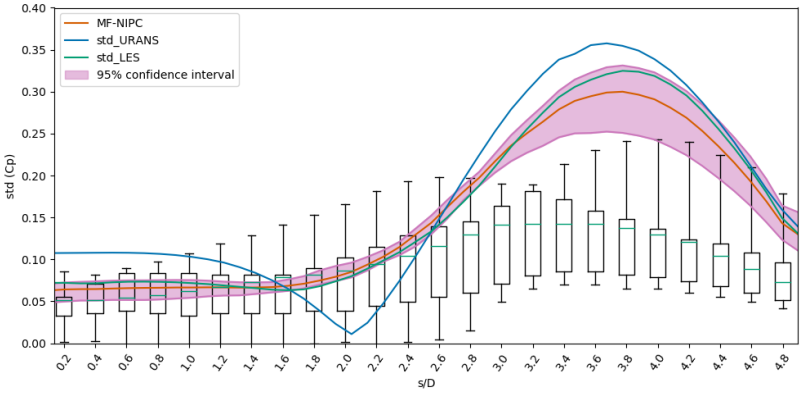

(b)

Figure 4.27: The side-averaged, span-wise-averaged distribution of (a) $\langle C_p \rangle$ and (b) $std(C_p)$: wind tunnel (6 realizations), mean and 95% confidence interval of the multi-fidelity NIPC result and deterministic simulation results (LES, URANS).

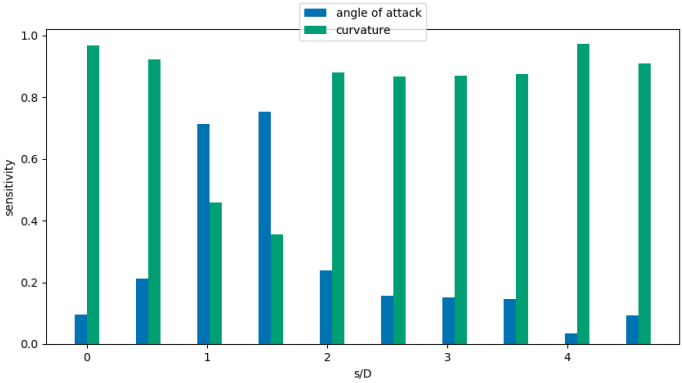

Figure 4.28: The Sobol sensitivity index as a function of downstream displacement. Close to the leading and trailing edges, the curvature radius is the dominant contributor to the uncertainty. However, in the region around the point where the pressure recovery starts both variables contribute almost equally.

averaged C_p. From Fig. 4.27(a), it can be seen that the largest uncertainties in MF-NIPC occur in the region where pressure recovery starts, with a similar tendency displayed in the six wind tunnel tests. For comparison, the deterministic simulations from section 4.2.4 are again plotted. We see that taking account of the uncertainties in the inflow conditions and the geometry of the structure in the MF-NIPC has produced a meta-model that is more consistent with the wind tunnel data than either of the two deterministic simulations. In the MF-NIPC, the position of pressure coefficient recovery moves upstream, which is closer to the behaviour seen in the wind tunnel results. Then, let us look at the results of the standard deviation of C_p. The largest uncertainties in MF-NIPC occur in the region where the standard deviation of C_p takes the maximum value, which is also seen in the wind tunnel tests. From these results, it can be said that the region, where the maximum standard deviation of C_p occurs, is caused by the considered input uncertainties in the MF-NIPC, namely: angle of attack and the curvature radius.

A benefit of employing Polynomial Chaos for uncertainty analyses is that the Sobol's sensitivity indices may be calculated at no additional cost through post-processing the PCE coefficients. The Sobol indices $S_{i_1,\ldots,i_s}$ for $1 \leq i_1 < \cdots < i_s \leq n, s = 1, \ldots, n$ (n:number of random variables) is defined as:

$$S_{i_1,\ldots,i_s} = \frac{D_{i_1,\ldots,i_s}}{D}, \tag{4.4}$$

where $D_{i_1,\ldots,i_s}$ is the partial variances and D is the total variance. Let us consider a two dimensional problem. As defined in the previous chapter PCE with two dimensional input variables is written as:

$$\begin{aligned} Y &= g(x_1, x_2) \\ &\approx \sum_{k=1}^{P} a_k \Psi_k(x_1, x_2). \end{aligned} \tag{4.5}$$

The first order Sobol's indices for each random variable are defined as:

$$S_1 = \frac{D_1}{D} \quad S_2 = \frac{D_2}{D}. \tag{4.6}$$

The second order Sobol's indices is defined as:

$$S_{12} = \frac{D_{12}}{D}. \tag{4.7}$$

The first order Sobol's indices means the influence of each variable alone and the second order Sonol's indices means the mixed influence of various variables. The total sensitivity indices for each variable is defined as:

$$S_{T_1} = S_1 + S_{12} \quad S_{T_2} = S_2 + S_{12}. \tag{4.8}$$

The partial variance is is defined from the Sobol's decomposition of PCE given in appendix A. Interested readers about the sensitivity analysis for the PCE methods are referred to Sudret [148]. Fig. 4.28 shows the total Sobol indices of each random variable as a function of distance downstream. From this figure, it can be seen that in region close to the leading and trailing edge, the curvature radius mostly effects the pressure coefficients. On the other hand, around the point where the pressure recovery starts ($s/D \approx 2.4$) uncertainties in both the curvature radius and the angle of attack contribute almost equally to the results.

4.3.3 Velocity field

Finally we consider the spatial distribution of the uncertainties in the velocity field. Fig. 4.29 shows the standard deviation of the span-wise averaged and time-averaged velocity field calculated by MF-NIPC. From this figure it can be seen that there is a significantly large uncertainty in the detached region at the leading edges. In addition, uncertainty can also be observed at the reattachment region to the rectangular cylinder and it results in the variation of the flow reattachment points.

4.4 Conclusion

In this chapter an uncertainty study using multi-fidelity NIPC has been carried out on the Benchmark on the Aerodynamics of a Rectangular 5:1 Cylinder

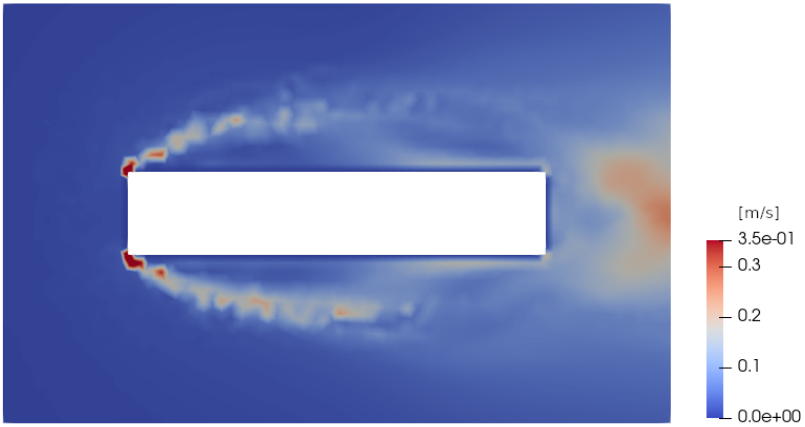

Figure 4.29: Standard deviation of span-wise averaged and time-averaged velocity calculated by MF-NIPC

(BARC). The effect of uncertainties associated with the angle of attack and radius of curvature of the cylinder corners were considered. Through a comparison of the PDFs for the bulk parameters, it was demonstrated that leveraging the results of low-fidelity models in a multi-fidelity framework could improve the accuracy of the uncertainty analysis. The results of the uncertainty analysis were then compared to experimental data from wind tunnel tests. It was observed that the multi-fidelity results were more consistent with the experimental data than deterministic simulations that were evaluated at the mean values of the uncertain inputs, with the pressure recovery start point moved noticeably further upstream. We can conclude from this study that the curvature radius and the angle of attack, that are both potential sources of uncertainty in wind tunnel tests, can effect the pressure coefficient results, particularly in the region of pressure recovery.

From a practical point of view, it is still not straightforward to carry out uncertainty analysis for the BARC geometry, even with the reductions in computational cost thanks to the multi-fidelity framework. A significant challenge exists in changing the curvature radius of the cylinder corners. This is understood to be a significant source of error in wind tunnel tests, however, the numerical implementation of this is difficult as it entails remeshing for each simulation, with a sufficiently refined mesh so that the curvature added to the cylinder corners can be captured by the simulation. This significantly increases the expense of the URANS simulations. Future research on this topic will seek to address these issues.

Chapter 5

Application of MF-NIPC to natural wind inflow problems

In this chapter, the introduced multi-fidelity Non-Intrusice Polynomial Chaos methods are applied to a natural wind inflow problem. The architectural structures are located in the atomospheric boundary layer (ABL), and the inlet wind velocity is affected by ground surface. In order to model this inlet velocity, the vertical wind variation and the turbulence intensity should be considered. In this chapter we choose the Silsoe 6m cube problem as a target case. The Silsoe 6m cube is well-documented benchmark cases for flow around a low-rise building. The significant advantage of the Silsoe cube is that there are full-scale observation data is available, while in CWE problems there are often only wind tunnel data available. In this chapter, first literature about the Silsoe cube are reviewed. Then, set ups and the validation of the CFD simulations are introduced. In order to carry out MF-NIPC, LES simulations are used as the high-fidelity simulation and URANS simulations are used as the low-fidelity simulations. Finally, the MF-NIPC is applied to the Silsoe 6m cube problem. The accuracy of MF-NIPC are checked by comparing the results from different models and the MF-NIPC results are compared with experiment results.

5.1 Introduction: the Silsoe 6m cube

For wind engineering problems, in many cases it is not possible to carry out wind tunnel experiments which have the same Reynolds number as actual problems, though it is recommended to keep the Reynolds number in the same range to observe turbulence phenomenon which have similar nature as the turbulence phenomenon of real buildings. For example, the Reynolds

number for the Silsoe cube is about 3×10^6. If 1/20 scale model is made, the inlet velocity should be about $166m/s$ to keep the same Reynolds number, which is almost impossible in normal wind tunnels. Therefore the full-scale data plays an important role in wind engineering problems.
In order to obtain the full-scale data, a 6m cube has been constructed at the Silsoe Research Institute in the United Kingdom in an open country exposed position as shown in Fig. 5.1. The 6m cube has a plain smooth surface finish and surface pressure is measured on a vertical and on a horizontal centerline section as shown in Fig. 5.2. Additionally surface pressure on the roof of the cube are also measured as shown in Fig. 5.3, however, these data are limited compared to the pressure on vertical- and horizontal center lines. In most measurements velocity is measured only at the reference mast, shown in Fig. 5.3, at the cube height. The most often reported Quantity of Interest in literature is the time averaged pressure coefficient $\overline{C_p}$ on the vertical- and horizontal ring. The time averaged pressure coefficient $\overline{C_p}$ is calculated as:

$$\overline{C_p} = \frac{\overline{p}}{\overline{q}}, \tag{5.1}$$

where $\overline{p}$ is the time averaged surface pressure and $\overline{q}$ is the time averaged dynamic pressure calculated from the velocity measured at the reference mast. The time statistics are calculated in time window of 12 minutes. The dynamic pressure q in Eq. (5.1) is defined as:

$$q = \frac{\rho}{2}(u^2 + v^2 + w^2), \tag{5.2}$$

where ρ is the air density and (u, v, w) is the instantaneous velocity components at the reference position. In the full scale measurement the pressure is stored as the relative pressure to static pressure at the reference mast. Literature about the Silsoe cube measurement can be roughly categorized to three categories, namely: about the full scale observation, about the CFD simulation and about the wind tunnel tests. Considering literature about the full scale observation, it can be classified to three aspects, namely: surface pressure observation (Kasperski et al. [75] and Richards et al. [120, 123, 127]), velocity field observation (Richards et al. [119, 122, 125] and Sterling et al. [145]) and the quasi-steady analysis (Richards et al. [118] and Richards et al. [121]). About the surface pressure, Kasperski et al. [75] investigated whether extreme values of the aerodynamic coefficients from the full scale observation follows the Extreme Value distribution type III. Though the full scale observation is advantageous, a problem of the full scale observation is that the wind condition is not controllable. Kasperski et al. [75] investigated how to obtain comparable peaks from raw data sets, by adjusting the time axis and frequency content. Richards et al. [123] introduce results of the additional pressure tappings on the roof shown in Fig. 5.3 and investigated pressure distribution on the roof. In addition, though most of the literature uses statistically analyzed data, such as mean, standard deviation, minimum and maximum values of measured data in a time window (mostly 12 minutes), Richards et al. [123] analyze raw data for 36 minutes before statistics are calculated,

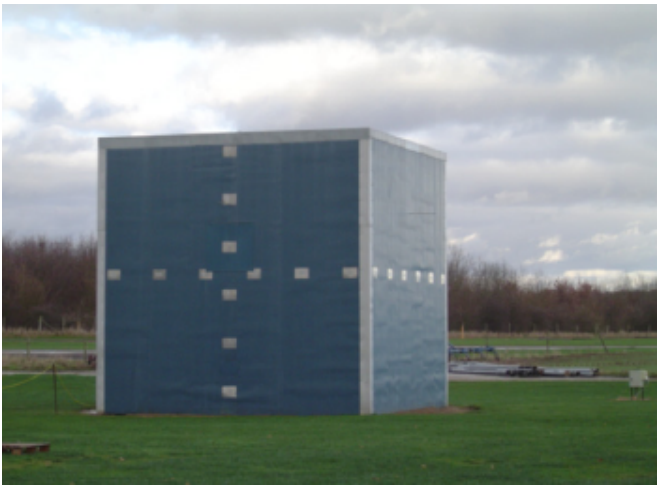

Figure 5.1: The Silsoe 6m cube (Richards et al. [120])

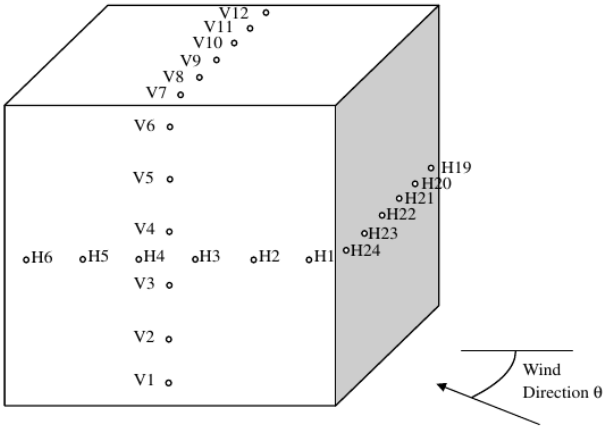

Figure 5.2: The pressure tap on a vertical and on a horizontal centerline (Richards et al. [120])

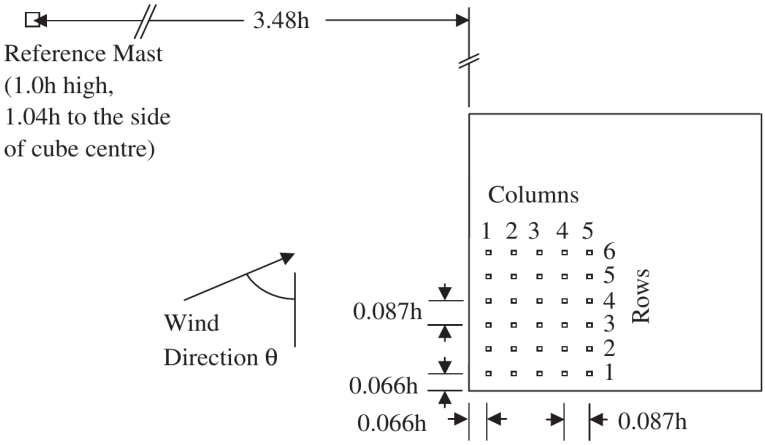

Figure 5.3: The additional roof tappings (Richards et al. [123])

and compares the effect of different time averaging window. Richards et al. [120] and Richards et al. [127] analyze the pressure on the vertical- and the horizontal center lines shown in Fig. 5.2, and fit the resulted pressure coefficient to the Fourier series as function of the time averaged wind direction $\overline{\theta}$ as:

$$\overline{C_p(\theta)} = \sum_{k=0}^{n} \overline{a_k} \cos(k\overline{\theta}) + \overline{b_k} \sin(k\overline{\theta}), \tag{5.3}$$

where $\overline{C_p}$ is the time averaged pressure coefficient, n is the order of the Fourier series and $\overline{a_k}$, $\overline{b_k}$ are fitted by the observation data. This is done by using large set of observation data. In order to get the variety of wind direction required to complete the Fourier analysis, the cube had been rotated. These results of Fourier analysis have been widely used for validation of CFD simulations and wind tunnel tests. In addition to the observation data, the quasi-steady method is often applied for the Silsoe cube problem. The quasi-steady method is popular in wind engineering problems, since mostly only the time averaged pressure coefficient is available as observation data, though the extreme pressure is required for designing structures. The quasi-steady method is a method to relate instantaneous pressure to the time averaged pressure coefficient and dynamic pressure. The simplest model in Richards et al. [121] is the equivalent-steady-gust (ESG) model:

$$p_{ESG} = \overline{C_p}(\overline{\theta})q, \tag{5.4}$$

where p_{ESG} is the pressure calculated from ESG model and q is the dynamic pressure.
CFD simulations have been carried out for the Silsoe cube using LES (e.g.

Guichard [63], Lim et al. [82], and Richards et al. [117]) and using RANS (e.g. Abohela et al. [3] and Wright et al. [166]). It should be noted that all CFD simulations in literature are carried out by the Finite Volume Method (FVM), rather than the Finite Element Method (FEM) used in this thesis. The notable aspect to carry out LES simulations to the Silsoe cube is that it is necessary to generate inflow turbulence (Lim et al. [82]), which is not common implementing LES simulations. Wind tunnel tests have been carried out and compared with full scale results (Richards et al. [124, 126]).

5.2 The Silsoe 6m cube test case

5.2.1 Calculation of the collocation points

In this chapter, the parameters of inlet wind, namely: velocity at the cube height and the inlet wind direction, are considered as uncertain variables. From now on we focus on an observation case with the wind direction 92°, which is a direction about to perpendicular to the front wall of the cube. We use a data set of 36 minutes observation, which is introduced in Richards et al. [123] as Run 242. In this observation the pressure taps on the roof and velocity at the mast in Fig. 5.3 had been recorded for 36 minutes. 4.17 samples are recorded per 1 second, which results in 9000 samples for 36 minutes. The reference velocity and wind direction are considered as input random variables. Definition of inlet velocity parameters will be explained in detail in following section. The histograms plotted by the 9000 samples are shown in Fig. 5.4. The collocation points are calculated by the arbitrary polynomial chaos methods introduced in previous chapter for the sparse grid level 2 and level 3. The sparse grid level corresponds to polynomial order = sparse grid level + 1. There are 14 collocation points for level 2 and 29 collocation points for level 3. 12 collocation points in level 3 are nested to those of the level 2.

5.2.2 High-fidelity model: Large Eddy Simulation

As a high-fidelity model the Large Eddy Simulation (LES) has been used. The computational domain is shown in Fig. 5.6. One side of the cube is $H = 6.0m$, and the size of computational domain was $(D_x, D_y, D_z) = (21H, 11H, 6H)$. The distance from the inlet boundary to the cube was $5H$. The outlet pressure was set to zero. The side boundaries and top boundary were slip boundary, and the slip condition and the wall functions were given to the surface of the cube and the ground. The wall function and the inlet wind boundary will be introduced in greater detail later. The computational domain was spatially discretized by unstructured tetrahedral elements. The computational domain was divided into four areas, and the meshes are refined in inner region. MPI with 72 threads are used for parallel computing. It is noted that KratosMultiphysics does not support periodic condition for MPI parallel computing, and in order to change the wind direction, the cube was rotated and the computational domain is remeshed. The mesh is shown in Fig. 5.8 for wind direction 92°. The height of the first cell closest to the cube

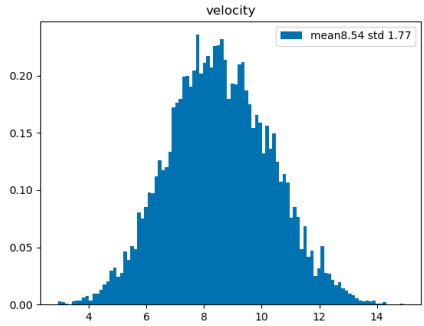

(a) velocity [m/s]

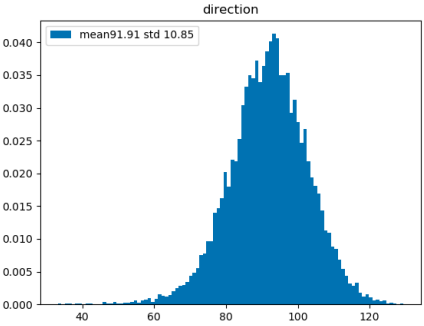

(b) wind direction [°]

Figure 5.4: Histograms plotted by 9000 samples of observation data

sides is 0.1. The mesh study has been carried out using coarser mesh and finer mesh, and the convergence with respect to C_p value on horizontal- and vertical rings are checked. The mesh is further refined at the roof to the height of the first cell as size 0.03. The mesh has $1,851,481$ elements. Time step is $0.03s$ and the statistical values are calculated for $600s$, so that the residual of the time averaged- and time standard deviation pressure coefficient on the roof center from the previous time window becomes less than 2.5 %. As time discretization the fractional step time discretization is used.

5.2.2.1 Inlet velocity

The natural wind velocity $\mathbf{u}$ is written as:

$$\mathbf{u} = \overline{\mathbf{u}} + \mathbf{u}', \tag{5.5}$$

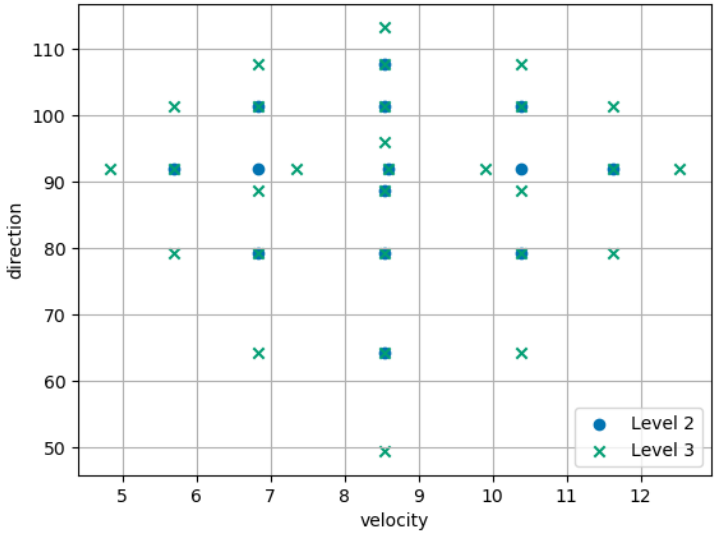

Figure 5.5: The collocation points calculated by the arbitrary polynomial chaos method based on the histograms

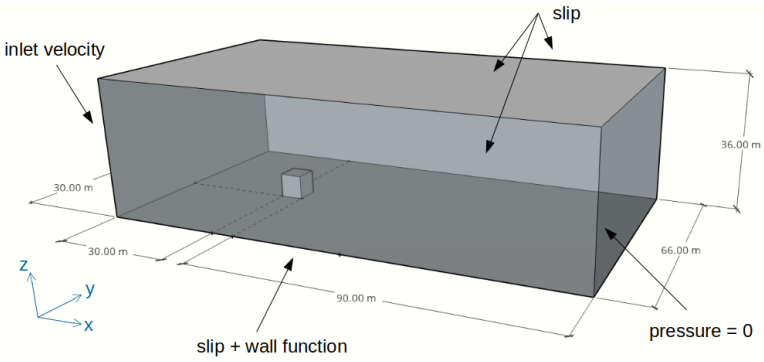

Figure 5.6: The computational domain of the Silsoe 6m cube simulation

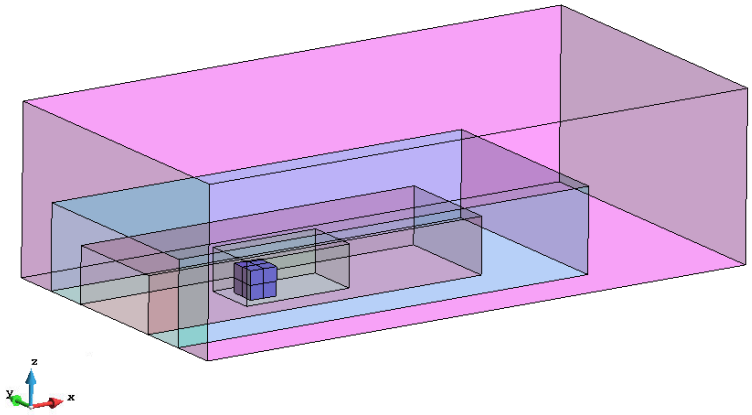

Figure 5.7: The computational domain of the Silsoe 6m cube simulation

where $\overline{\mathbf{u}}$ is the mean velocity and $\mathbf{u}'$ is the gust velocity. As it is pointed out by Lim et al. [82], it is important for natural wind LES simulations to take the gust velocity into account at the inlet boundary. In this section we introduce how to impose natural wind to inlet boundary to the LES simulations.

Considering the mean velocity $\overline{\mathbf{u}}$, according to Richards et al. [125], the mean velocity at the Silsoe research Institute follows the logarithmic profile:

$$u(z) = \frac{u_\tau}{\kappa} \ln(\frac{z}{z_0}), \tag{5.6}$$

with a roughness length $z_0 = 0.01m$, von Karman's constant $\kappa = 0.4$ and u_τ is the friction velocity. Here the friction velocity is determined as the velocity at the cube height and we call it now as the reference velocity. The reference velocity u_τ is considered as an input random variable in this chapter and is changed according to the collocation points calculation calculated in Section 5.2.1. Considering the gust velocity $\mathbf{u}'$, characteristics of the gust velocity is usually expressed by the Turbulence Intensity (T.I.) and the turbulence energy spectrum $S_i(f)$ as:

$$T.I. = \frac{\overline{u'u'}}{\overline{u}}, \tag{5.7}$$

$$S_i(f) = 2 \int_{-\infty}^{\infty} \overline{u_i'(t_0) u_i'(t_0 + t)} \exp(-2\pi i f t) dt. \tag{5.8}$$

Two methods are known to generate time-varying inlet wind from the turbulence intensity and the spectrum, namely: the precursor simulations (Tabor

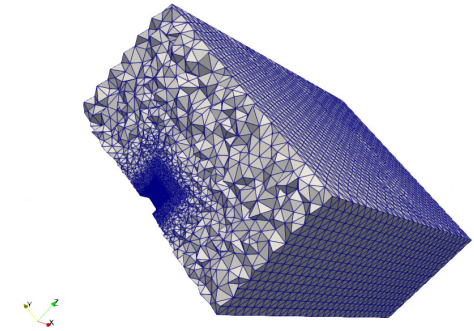

(a)

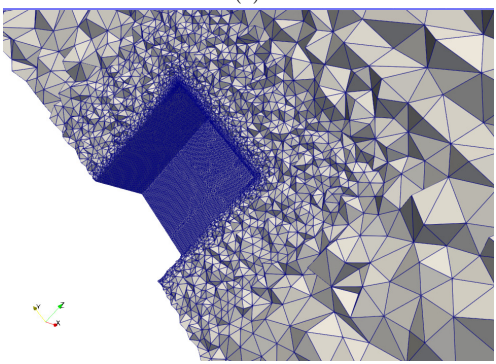

(b)

Figure 5.8: Meshing for LES (a) whole cross section and (b) near-body

et al. [151]) and the synthetic generations (Mann [87]). Due to lower computational cost, the Mann's method which is one of the synthetic generations is used in this chapter to generate the gust velocity at the inlet boundary of the LES simulations. Mann [86] introduces an explicit model of the spectral tensor $\mathbf{\Phi}(\beta_{LT})$, where $\beta_{LT} = t\frac{\partial \overline{u}}{\partial z}$: a dimensionless eddy lifetime. The spectral tensor corresponds to isotropic turbulence with von Kármán energy spectrum:

$$E(k) = E_0 L_{iso}^{5/3} \frac{(L_{iso}k)^4}{(1 + (L_{iso}k)^2))^{(17/6)}}, \tag{5.9}$$

where k: wavenumber and E_0 and L_{iso} is model parameters. The dimensionless eddy lifetime β_{LT} is modeled as:

$$\beta_{LT}(k) = \Gamma_{LT}(L_{iso}k)^{-2/3} \left[{}_2F_1\left(\frac{1}{3}, \frac{17}{6}; \frac{4}{3}; \frac{1}{(L_{iso}k)^2}\right)\right]^{-1/2}, \tag{5.10}$$

size of computational domain	$L_x \times L_y \times L_z$	$11520 \times 90 \times 45$
grid refinement in each direction	$N_x \times N_y \times N_z$	$16384 \times 128 \times 64$
the reference height	z	25 m
mean velocity at z	$\overline{u}(z)$	10.20 m
roughness for logarithmic profile of the mean velocity	z_0	0.01 m
roughness	z_*	0.03 m

Table 5.1: parameters for generating the inlet wind

where Γ_{LT} is a model parameters and it is often assumed as 3.9. In the Mann's method the gust velocity $\mathbf{u}'$ is calculated as:

$$\mathbf{u}'(\mathbf{x}) = \sum_{\mathbf{k}} \hat{\mathbf{u}}'(\mathbf{k}) \exp(i\mathbf{k} \cdot \mathbf{x}) \Delta\mathbf{k}, \tag{5.11}$$

where

$$\hat{\mathbf{u}}' = \frac{\sqrt{L_1 L_2 L_3}}{(2\pi)^{3/2}} \mathbf{C}(\mathbf{k}) \mathbf{n}(\mathbf{k}), \tag{5.12}$$

with L_i: computational domain for the time varying velocity calculation, $\mathbf{n}(\mathbf{k})$ is the independent Gaussian complex random vector of the unit variance and $\mathbf{C}(\mathbf{k})$ is a tensor calculated from the turbulence energy spectrum tensor $\mathbf{\Phi}(\beta_{LT})$. In order to give the time varying inlet velocity, first the spatially varying gust velocity is calculated by Eq. (5.11). Then temporally varying inlet velocity data is generated based on the Taylor's frozen turbulence hypothesis (Taylor [154]). The Mann's method is implemented in the C library as WindGen (Andre [8]). The interested reader for the implementation of the WindGen is reffered to Andre [7]. The parameters used for the inlet wind generations are shown in Table 5.1. These parameters are used for a validation case, in which mean velocity at the cube height is $8.34 m/s$. The reference height z is used to calculate the model parameter L_{iso} in Eq. (5.9) as $L_{iso} = 0.59z$, and it controls the turbulence length. The roughness z_* and the reference height z are used to calculate the model parameter E_0 in Eq. (5.9) as $E_0 = 3.2u_*^2/z^{2/3}$, where u_* is calculated from the logarithmic profile Eq. (5.6), with u_τ calculated from defined mean velocity and the roughness z_*. z_* influences the turbulence intensity and it is calibrated, so that the resulted turbulence intensity becomes around $10 \sim 20\%$. It should be noted that in WindGen the turbulence intensity cannot be imposed directly and the turbulence intensity should be controlled through the parameter z_*. Therefore it is very difficult to change the turbulence intensity to exact value and it is a reason why the turbulence intensity cannot be used as an input random variable. In order to generate the velocity at each collocation point calculated in Section 5.2.1, the mean velocity $\overline{u}(z)$ in Table 5.1 is adjusted, otherwise

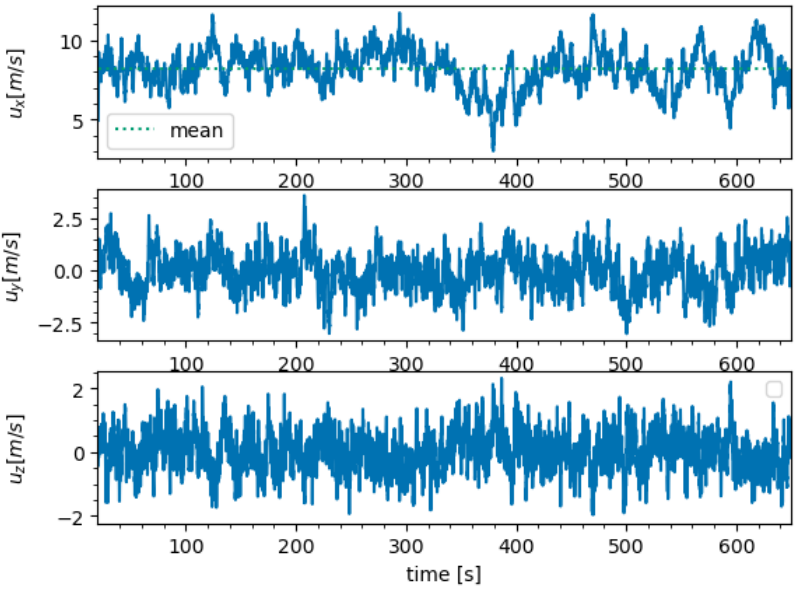

Figure 5.9: Inlet velocity at the cube height generated by the WindGen using parameters indicated in Table 5.1

parameters were kept same. The inlet velocity generated by WindGen at the cube height is shown in Fig. 5.9. The resulted turbulence intensity is $T.I. = 10.5\%$.

Having inputted the generated time varying inlet velocity, the LES simulations are carried out. Fig. 5.10 shows the wind velocity profile and the turbulence intensity profile at x = 0.0 m, 6.0m, 12.0 m and 18.0 m. The inlet boundary of the computational domain is located at the x = 0.0 m and the front wall of the cube is located at x = 30.0 m. The CFD results are compared with the full scale measurement data and the wind tunnel experiments data from Richards et al. [124]. The mean velocity distribution matches very well with the full scale measurement data. The turbulence intensity matches also well with the full scale data and the wind tunnel experiment data. The turbulence intensity in y direction (c) is slightly smaller than the full scale data. It may be because σ_v^2/σ_u^2 in the Kaimal model is smaller than the one in the full scale.

5.2.2.2 Near wall treatment

Since the Reynolds number is very high for the natural wind problems, it is required to use wall functions at the surface boundary of the cube instead of the no-slip condition. While the simple log-law model has been introduced in

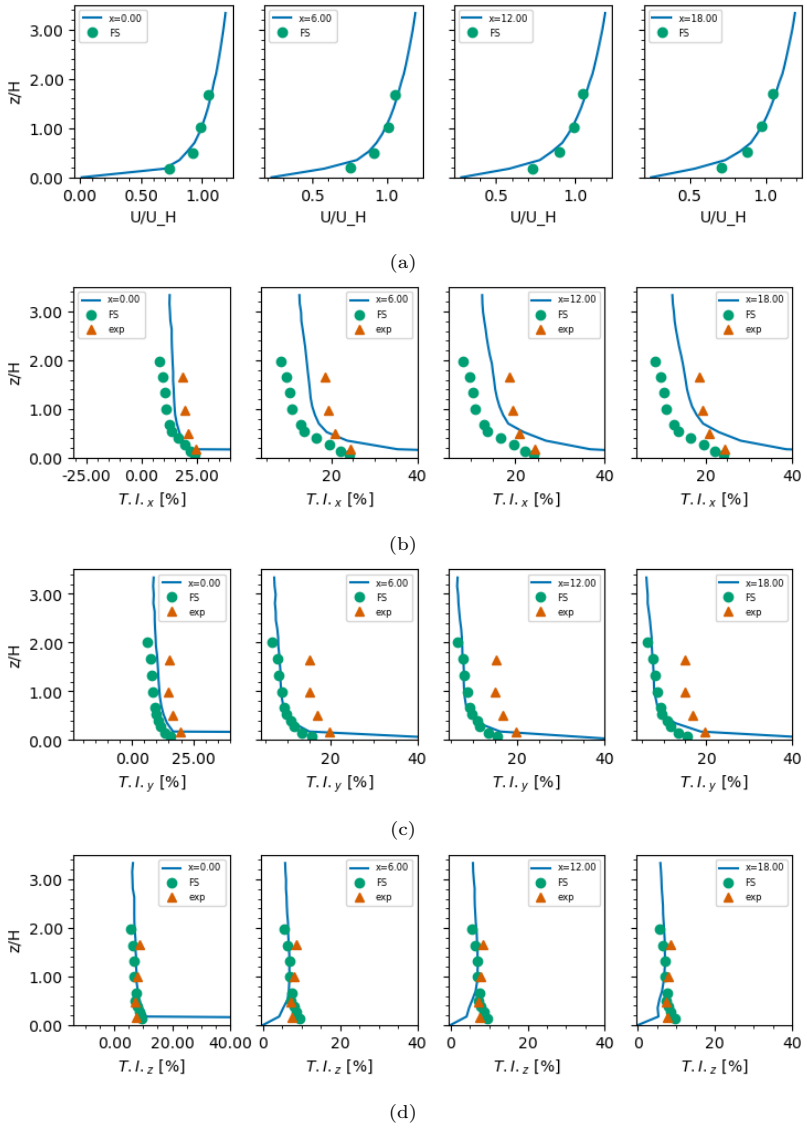

Figure 5.10: The evolution of z direction profile of (a) mean velocity (b) T.I. in x direction (c) T.I. in y direction (d) T.I. in z direction at x = 0.0 m, 6.0 m, 12.0 m, 18.0 m. The inlet boundary is located at x = 0.0 m and the front wall of the cube is located at x = 30.0m. The results are compared with the full scale observation data (:FS) and the wind tunnel experiment data (:exp) in Richards et al. [124]

the previous Chapter 3.1.3, for the LES simulation for the Silsoe cube, the Werner and Wengle wall functions has been used. The Werner and Wengle wall function was introduced by Werner et al. [161] for LES simulations of flow around obstacles with sharp edges and corners. Interested readers for detailed implementation and application examples of the Werner and Wengle wall function within the FEM based CFD are referred to Andre [7]. In the Werner and Wengle wall function, the wall shear stress τ_w is calculated as:

$$\tau_w = \begin{cases} \frac{\mu|\mathbf{u}(y_w)|}{y_w} & \text{if } \mu|\mathbf{u}(y_w)| \leq u_c \ , \\ \rho\left[\frac{1-\alpha}{2}A^{\frac{1+\alpha}{1-\alpha}}\left(\frac{\mu}{2\rho y_w}\right) + \frac{1+\alpha}{A}\left(\frac{\mu}{2\rho y_w}\right)^{\alpha}|\mathbf{u}(y_w)|\right]^{\frac{2}{1+\alpha}} & \text{otherwise,} \end{cases} \tag{5.13}$$

where $u_c = \frac{\mu}{4\rho y_w}A^{\frac{2}{1-\alpha}}$, $A = 8.3$ and $\alpha = 1/7$. $\mathbf{u}(y_w)$ is computed as the projection of the instantaneous velocity onto the plane defined by the boundary face. y_w is defined as an intersection point of the normal vector of the boundary face with the interior surface of the boundary cell. Using the τ_w, the friction velocity u_τ is calculated by $u_\tau = \sqrt{\tau_w/\rho}$ and the Neumann condition is applied using u_τ as explained in the previous Chapter 3.1.3.

5.2.3 Low-fidelity model: Unsteady Reynolds Averaged Navier-Stokes simulation

As a low-fidelity model the unsteady Reynolds Averaged Navier-Stokes simulations (URANS) has been used. URANS simulations with a k-ω SST turbulence model were carried out in three dimensions, so that the wind direction can be changed for MF-NIPC. The size of computational domain was same as the one for the LES simulations. At the inlet boundary condition the log normal mean velocity, the turbulence intensity 17.47% and the turbulence mixing length 126.0 m are given. The turbulence intensity is taken from the full scale measurement. The turbulence mixing length is the length of the computational domain. The given log normal mean velocity (Eq. (5.6)) at the inlet boundary is same as the ones used for the LES simulations. The reference velocity u_τ is changed according to value at each collocation point. The outlet pressure was set to zero. The side boundaries and top boundary were slip boundary, and the slip condition and the wall functions were given to the cube surface and the ground. The log-law function was used as a wall function (see Section 3.1.3). Time step was $0.03[s]$ and the simulation was run until it converges to steady state, which is until $50[s]$. As time discretization the fractional step time discretization is used. URANS simulations are paralleled by OpenMP with 12 threads. Determination of mesh will be explained in greater detail below.

Determination of mesh The accuracy of an URANS simulation highly depends on mesh refinement. The finer mesh gives more accurate results, however it is clear that the finer mesh requires more computational power. The objective of this thesis is to reduce total computational cost by running low-fidelity models in the higher order collocation points instead of running

	focused region	cube side surface	cube roof surface	number of cells
fine	0.05	0.017	0.017	1,607,004
middle	0.067	0.033	0.017	910,131
coarse	0.1	0.05	0.25	461,251

Table 5.2: Size of cells δ/H ($H = 6$m) and the number of cells for three different mesh settings

the high-fidelity model. In order to get meaningful computational time saving, an appropriate mesh size should be chosen by considering calculation accuracy and computational time. In this section the results of three meshes are compared and a mesh is chosen for the low-fidelity model. In Table 5.2 the size of cells and the number of cells for three mesh settings are indicated. The computational domain is divided in the same manner as for LES simulations (see Fig. 5.7). The cell sizes of outer region were kept same, since it has been observed that the size of the outer mesh has less influence to the results. The mesh overview for the coarse mesh is shown in Fig. 5.11. In Fig. 5.12 the result of the time averaged pressure coefficients on vertical- and horizontal ring calculated by the three different meshes are compared with the observation data based results with the angle of attack 90 ° in Richards et al. [120]. Then the total computational time for the MF-NIPC and the time saving of the multi-fidelity framework compared to single fidelity NIPC with the high-fidelity model and average relative deviation from the experimental data of $\overline{C_p}$ from Richards et al. [120] are compared in Table 5.3. LES simulations are calculated using 72 threads and one deterministic simulation takes about 1728 total CPU time [hours]. URANS simulations are calculated using 12 threads and one deterministic simulation takes fine mesh: 308 [h], middle mesh: 209 [h] and coarse mesh: 99 [h]. From Fig. 5.12 it can be seen that $\overline{C_p}$ converges for the fine mesh and middle mesh. $\overline{C_p}$ of the coarse mesh does not converge perfectly, however it can be seen that the coarse mesh is also able to detect the trend. According to Table 5.3, the average relative deviations from the observation data do not exceed 25% in every case, and the time saving of the coarse mesh is significant. Having considered that the coarse mesh could detect the trend of $\overline{C_p}$ distribution and its time saving, we decided to choose the coarse mesh as the low-fidelity model for MF-NIPC.

5.2.4 Validation of deterministic results

In this section, the results of aforementioned LES simulations and URANS simulations are compared with the observation data in purpose of validation. First, let us compare the evolution of velocity profile. Fig. 5.13 compares the evolution of mean velocity profile between LES simulation, URANS simulation and the full scale observation Richards et al. [124]. $x = 0.0$ is the inlet boundary of the computational domain and the front wall of the cube

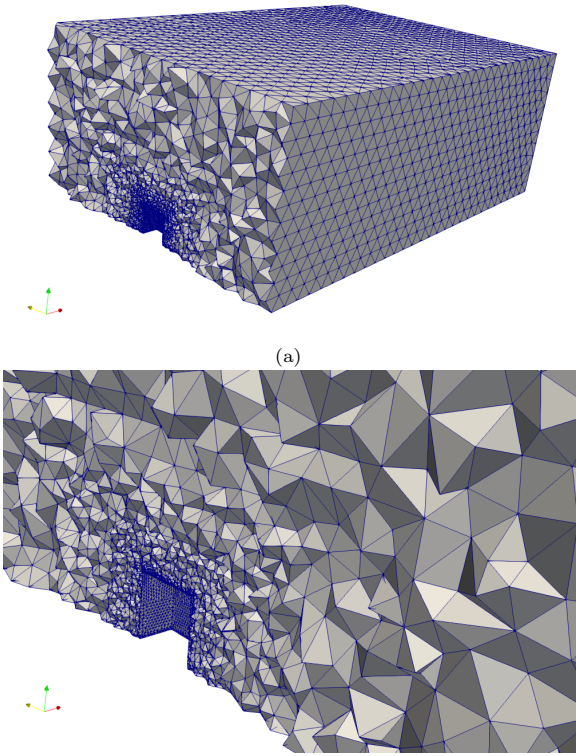

(a)

(b)

Figure 5.11: Meshing for URANS (a) whole cross section and (b) near-body

locates at $x = 30.0$. The mean velocity profile matches very well in all results. In order to change the wind direction in CFD simulations, the cube is rotated, therefore the inlet wind is changed only due to the mean velocity to carry out MF-NIPC.

Then let us compare the time averaged pressure coefficient $\overline{C_p}$ on the vertical- and horizontal ring. The definition of vertical- and horizontal lines' name are illustrated in Fig. 5.14. $\overline{C_p}$ results are plotted distance over the cube divided by a side of the cube $h = 6m$. In order to confirm that both models can detect change of wind direction, $\overline{C_p}$ is compared for the case with wind direction 92° (Fig. 5.15) and 64° (Fig. 5.16), which are values at ones of the collocation points. The inlet mean velocity at the cube height is $8.34m/s$ for the wind direction 92° and $8.54m/s$ for the wind direction 64°. The Fourier

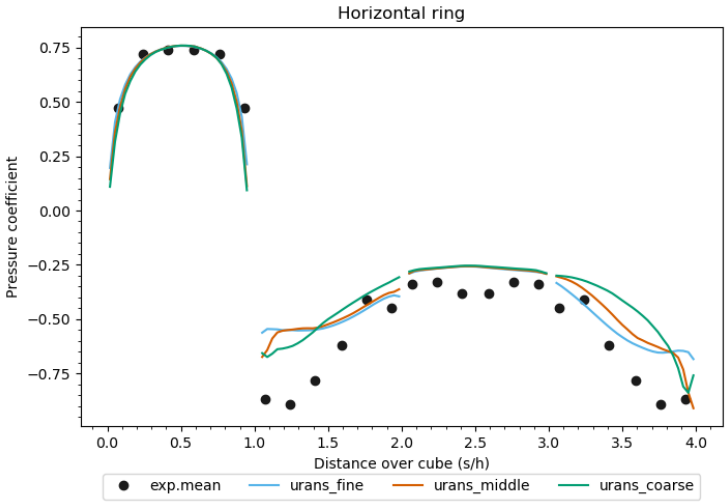

(a)

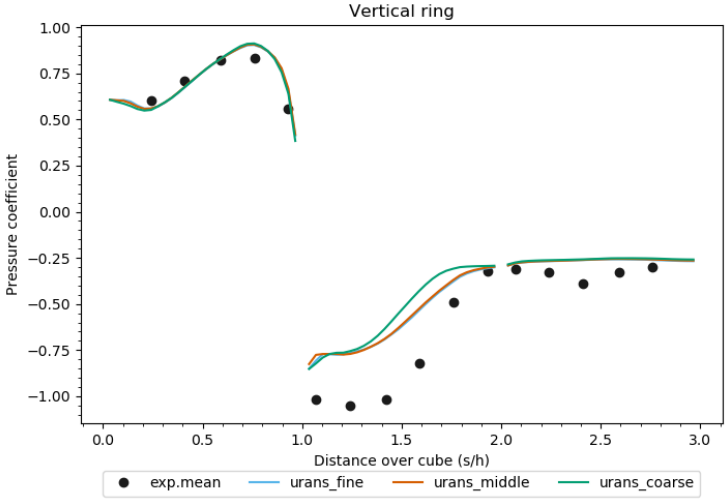

(b)

Figure 5.12: Comparison of the time averaged pressure coefficient $\overline{C_p}$ on (a) horizontal ring and (b) vertical ring. URANS simulations are calculated using the three mesh settings and compared with the experimental data analyzed for the wind direction 90° in Richards et al. [120]

	average relative deviation from exp.		total calculation time		time saving
	H-ring	V-ring	HF(L3)	MF	
fine	17.4 %	17.2 %	50112	34048	32.1 %
middle	18.7 %	17.9 %		30880	38.4 %
coarse	21.2 %	20.0 %		27360	45.4 %

Table 5.3: Comparison of calculation time and average relative deviations from the experimental data of $\overline{C_p}$. The calculation time is shown in total CPU time [hours]. HF(L3): total CPU time for Level 3 NIPC with high-fidelity model only, MF: total CPU time for multi-fidelity NIPC.

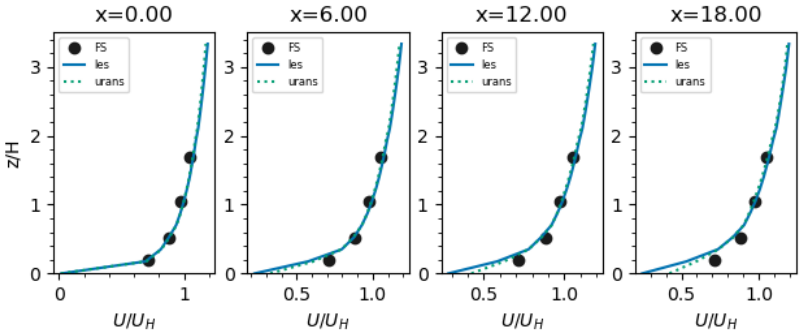

Figure 5.13: Comparison of evolution of the mean velocity profile. FS: the full scale observation data from Richards et al. [124]

analyzed full scale data from Richards et al. [120] with wind direction 90° and 60° are also plotted in Fig. 5.15 and Fig. 5.16 respectively. From Fig. 5.15 and Fig. 5.16, it can be seen that both LES and URANS show similar trend with the full-scale observation data. It is noted that the $\overline{C_p}$ distribution on horizontal ring $1.0 < s/h \leq 2$ and $3.0 < s/h \leq 4$ are not symmetric, because the wind directions in CFD simulations are not exactly 90° but 92°. In Table 5.4, the average relative deviation of LES results from the analyzed full scale data and the URANS results from the LES results for both wind direction 92° and 64° are summarized. It is calculated by averaging the relative deviation at the pressure taps on a same face of the cube. The numbering of each face is illustrated in Fig. 5.14. The average relative deviation on $H4$ for 64° is very high, because the absolute value is close to zero. Except for this, the average relative deviation does not exceed 27% and it can be said that all results agree well, as all the average relative deviation is smaller than 27%.

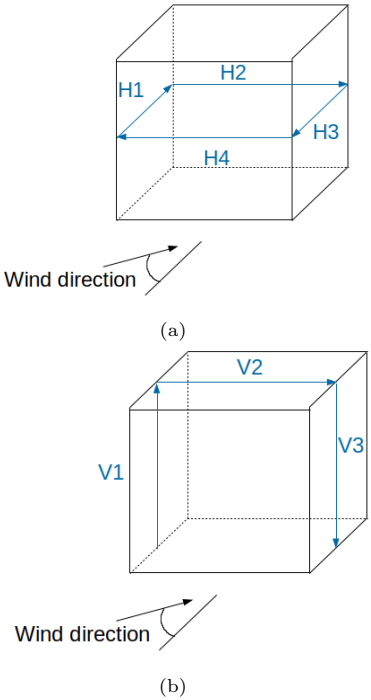

Figure 5.14: (a) horizontal ring and (b) vertical ring

Comparing the average relative deviation of URANS from LES between 92° and 64°, there are no trend which direction can be estimated better or worse by the low-fidelity model URANS.

Then time averaged pressure coefficient $\overline{C_p}$ at the pressure taps on the roof of the cube calculated by the LES simulation, the URANS simulation and the full scale observation reported in Richards et al. [123] are compared in Fig. 5.17. The numbering of the pressure taps is illustrated in Fig. 5.3. The averaged relative deviation for each row is calculated in Table. 5.5. It can be seen that in every row results of LES simulations matches well with experimental data, as the average relative deviations from the experimental data are less than 10% for every row. The discrepancy between URANS results and LES results are relatively large at the rows close to the edge (R1 and R2). Since the mesh of URANS is coarser than the mesh of LES, URANS might include larger error due to singularity happened at the edges than at the center of the cube. In every row, the LES simulations underestimate the minimum suction of first column (C1) where the closest column to windward face, especially at the corner of the roof (R1C1) the underestimation is significant. This will be investigated in greater detail later with the MF-NIPC results.

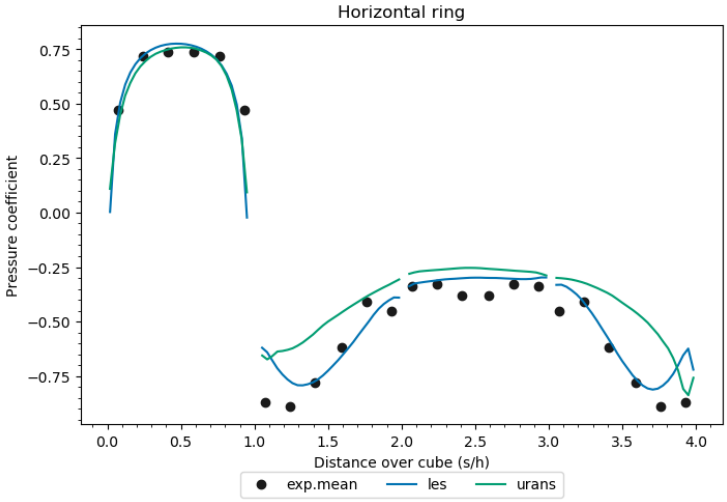

(a)

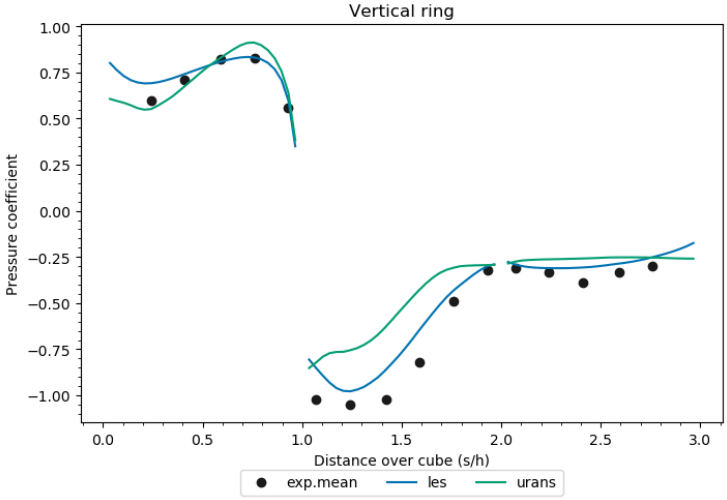

(b)

Figure 5.15: Comparison of the time averaged pressure coefficient $\overline{C_p}$ on (a) horizontal ring and (b) vertical ring. URANS and LES simulations are carried out for wind direction 92°. The experimental data was Fourier analyzed for the wind direction 90° in Richards et al. [120]

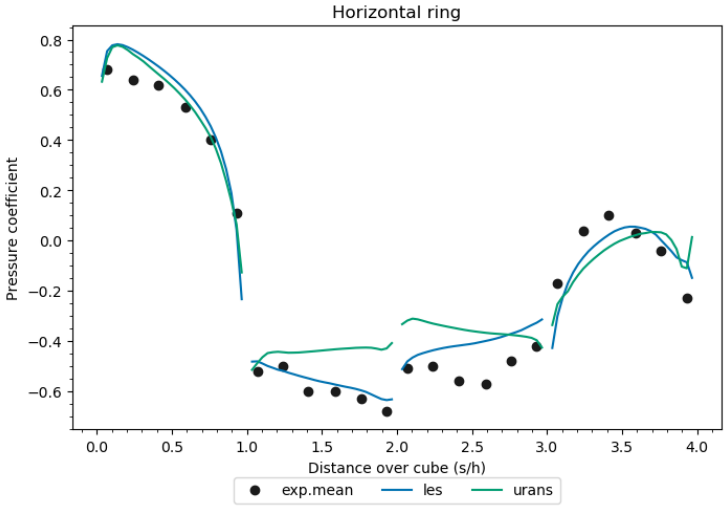

(a)

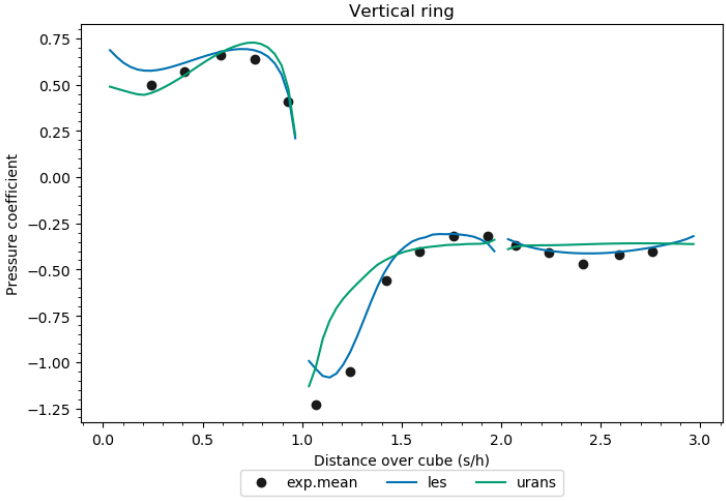

(b)

Figure 5.16: Comparison of the time averaged pressure coefficient $\overline{C_p}$ on (a) horizontal ring and (b) vertical ring. URANS and LES simulations are carried out for wind direction 64°. The experimental data was Fourier analyzed for the wind direction 60° in Richards et al. [120]

wind direction 92°							
	H1	H2	H3	H4	V1	V2	V3
LES - exp.	8.2 %	13.0 %	11.7 %	12.2 %	5.7 %	12.8 %	12.5 %
URANS - LES	3.8 %	**26.7** %	14.0 %	**23.2** %	14.3 %	**22.6** %	15.5 %
wind direction 64°							
	H1	H2	H3	H4	V1	V2	V3
LES - exp.	**21.6** %	6.0 %	19.6 %	**111.4** %	8.4 %	11.0 %	5.8 %
URANS - LES	10.7 %	**22.5** %	17.2 %	**206.8** %	12.7 %	19.6 %	9.3 %

Table 5.4: Average relative deviation for $\overline{C_p}$ on horizontal ring (H1-H4) and vertical ring (V2-V3). The average relative deviation of LES results from the full scale analyzed data from Richards et al. [120] and URANS results from LES results for wind direction 92° and 64° are calculated. The average relative deviation which exceed 20% are shown in bold.

	R1	R2	R3	R4	R5	R6
LES-exp.	7.4 %	7.4 %	7.6 %	7.8 %	9.3 %	9.1 %
URANS-LES	36.6 %	32.1 %	28.3 %	24.3 %	22.5 %	22.6 %

Table 5.5: Relative deviations for $\overline{C_p}$ of the roof pressure tap. The relative deviations are averaged in every row. The average relative deviation of LES results from the full scale analyzed data from Richards et al. [123] and URANS results from LES results for wind direction 92° are calculated.

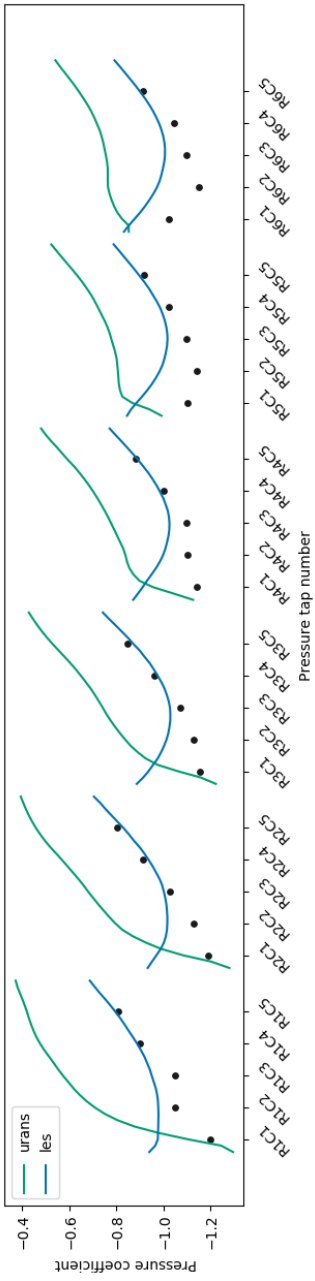

Figure 5.17: Comparison of the time averaged pressure coefficient $\overline{C_p}$ on pressure taps on the roof of the cube shown in Fig. 5.3. URANS and LES simulations are carried out for wind direction 92°. The CFD results are compared with the experimental data in Richards et al. [123]

5.3 Results: Multi-fidelity Non-Intrusive Polynomial Chaos

In this section, the result of MF-NIPC applied to the flow around the Silsoe cube simulations is introduced. First we compare Probability Density Function (PDF) results calculated by MF-NIPC and single-fidelity NIPC, and investigate accuracy of the multi-fidelity framework. Afterwards we compare the stochastic results calculated by MF-NIPC with experimental results and investigate the effect of input random variables to the Quantity of Interests (QoIs).

5.3.1 Accuracy of the multi-fidelity framework

In this section, PDF results of pressure coefficient C_p at the pressure taps on the roof center V7 - V12 calculated by different models are compared to highlight the accuracy of the multi-fidelity framework compared to single-fidelity NIPC (See the numbering of the pressure taps in Fig. 5.2). The results are compared between high-fidelity level 2 (HF(L2)), high-fidelity level 3 (HF(L3)), low-fidelity level 3 (LF(L3)) and multi-fidelity (MF). Before analyzing the PDF, let us look at streamlines for a deterministic simulation to overview flow characteristic around the roof. Fig. 5.18 shows the time averaged streamlines calculated by a LES deterministic simulation with wind direction 92°. From Fig. 5.18 it can be seen that flow separate at the leading edge and reattach around the observation point V11, which corresponds to the $\overline{C_p}$ distribution result Fig. 5.15. Now let us analyze the PDFs of the pressure coefficients calculated by different models. First we consider the time averaged pressure coefficient as QoI. Fig. 5.19 shows PDFs calculated by the high-fidelity model with the sparse grid level 3(HF(L3)), the high-fidelity model with the sparse grid level 2(HF(L2)), the low-fidelity model with the sparse grid level 3(LF(L3)) and the multi-fidelity model(MF). At the tap V7 and V9, PDFs of HF(L2), HF(L3) and MF converge to the almost same results and the improvement of MF framework from HF(L2) is not significant. PDFs of V10 and V11 have discrepancy between HF(L2) and HF(L3), however MF gives rather similar results with HF(L2) than HF(L3), and the improvement of MF framework is not clear. PDFs of V8 and V12 have also discrepancy between HF(L2) and HF(L3). PDF of MF has closer shape to HF(L3) than to HF(L2), and the improvement of MF can be seen here. Fig. 5.20 shows the response surface estimated by MF-NIPC and the deterministic results calculated by the high-fidelity model and the low-fidelity model. The pressure taps V8 and V12, where improvement of MF can be seen, have more complicated response surface shape compared to other pressure taps.

Then, let us consider the time standard deviation of the pressure coefficients. Following Richards et al. [120], the time standard deviation of the pressure coefficient $t - std(C_p)$ is calculated as:

$$t - std(C_p) = \frac{\sigma_p}{\sigma_q}, \tag{5.14}$$

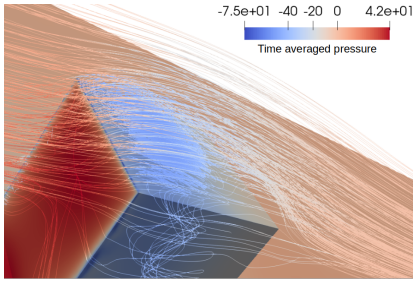

(a)

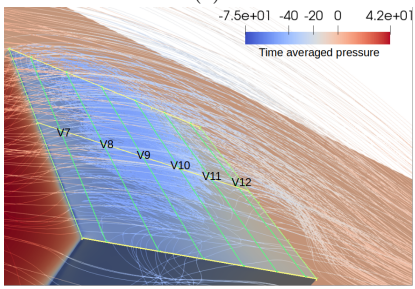

(b)

Figure 5.18: Time averaged streamlines calculated by LES for wind direction 92° and inlet velocity at the cube height 8.53 m/s. The streamlines around the roof is shown in (a), and the pressure observation points are indicated in (b)

where σ_p is the time standard deviation of the pressure and σ_q is the time standard deviation of the dynamic pressure. Since URANS simulations converge to the steady state solution, the time standard deviation of the pressure coefficients cannot be obtained from URANS simulations. Richards et al. [121] introduces the quasi-steady methods to estimate the time standard deviation of the pressure coefficients from the time averaged pressure coefficients. Based on the simplest quasi-steady theory (Cook [31]), the pressure variations are caused by change in the instantaneous dynamic pressure alone, therefore the standard deviation of the pressure coefficients may be estimated by equal to the absolute value of the time averaged pressure coefficients. Though it is the simplest and rough estimation of the standard deviation of the pressure coefficients, we investigate the ability of MF framework to improve the stochastic results compared to single-fideliy NIPC. Fig. 5.21 shows the PDF comparisons of the time standard deviation of the pressure coefficients at the pressure taps V7 - V12. At V9, V10, V11 and V12 the PDFs of HF(L2) almost converges to the PDFs of HF(L3) and MF. At V7, PDF estimated by MF is in between HF(L2) and HF(L3) and the improvement of MF can be seen, even though LF is the very rough estimation calculated by the quasi-steady

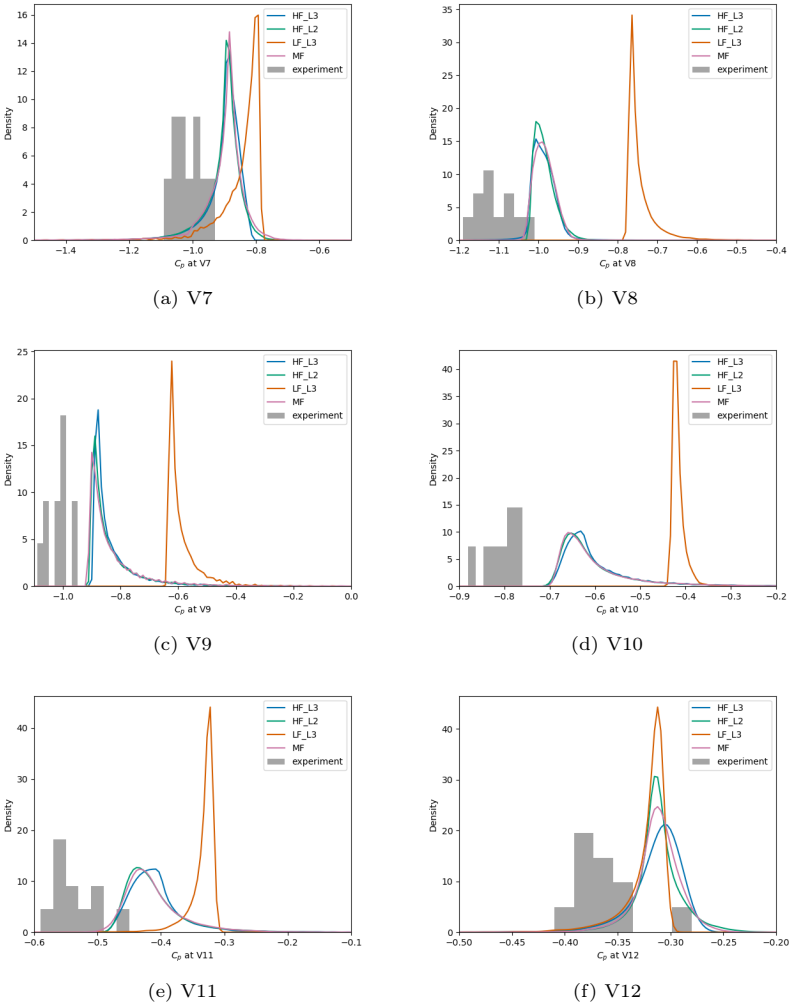

(a) V7 (b) V8

(c) V9 (d) V10

(e) V11 (f) V12

Figure 5.19: Probability Density Function of the time averaged pressure coefficient at the pressure tap (a) V7 (b) V8 (c) V9 (d) V10 (e) V11 (f) V11, calculated by the high-fidelity model with sparse grid level 2(HF_L2, green), the high-fidelity model with sparse grid level 2(HF_L3, blue), the low-fidelity model with sparse grid level 3(LF_L3, orange) and the multi-fidelity model (MF, pink). The experimental results from Richards et al. [120] are also plotted.

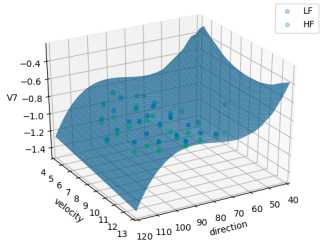

(a) V7

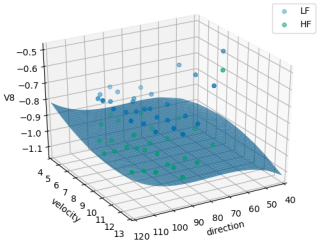

(b) V8

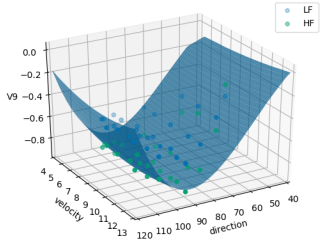

(c) V9

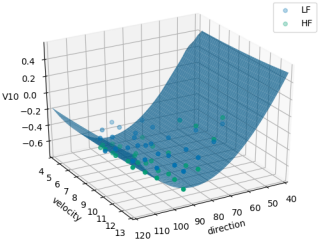

(d) V10

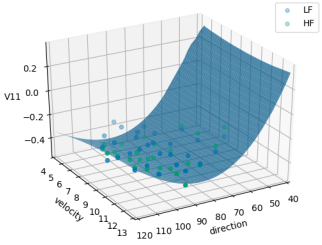

(e) V11

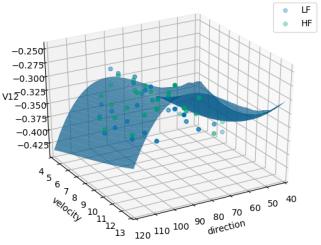

(f) V12

Figure 5.20: Response surface of the time averaged pressure coefficient at the pressure tap (a) V7 (b) V8 (c) V9 (d) V10 (e) V11 (f) V11, calculated by the high-fidelity model(HF), the low-fidelity model (LF) and the multi-fidelity model (MF).

model. At V8, PDF of MF and HF(L2) are almost same and the improvement of MF is not significant. Fig. 5.22 shows the response surface estimated by MF-NIPC and the deterministic results calculated by the high-fidelity model and the low-fidelity model. The pressure tap V7, where improvement of MF can be seen, have more non-linear response surface compared to other pressure taps as observed in the response surface of $\overline{C_p}$.

Overall, it is confirmed that the MF-NIPC can improve the stochastic results compared to single-fidelity NIPC, especially in case the resulted response surface have complicated shape. As indicated in Table 5.3, MF framework can save 45.4 % of total CPU time compared to HF(L3). Having considered this significant time saving, though improvement of MF is not observed at the all pressure taps, we can conclude that it is worth applying MF framework to NIPC.

5.3.2 Comparison of UQ results with experimental data

From this point we will use only MF-NIPC results as UQ result. First, let us consider the pressure coefficient distribution of the vertical ring shown in Fig. 5.2. In Section 5.2.4 the CFD results are compared with results from Richards et al. [120], which is after the Fourier analysis. In this section the stochastic results calculated by MF-NIPC are compared with experimental raw data before Fourier analysis is applied. One experimental data is time averaged in 12 minutes and the data sets which has mean wind direction $92\pm1^\circ$ are selected for comparison. Fig. 5.23 shows the comparison of the stochastic results, deterministic results of LES and URANS and the experimental data. The 95% confidence interval is calculated using the parametric bootstrapping explained in the previous chapter. Unlike BARC case, the stochastic mean value has very close value as the deterministic result calculated by a LES deterministic simulation. It is to say that the stochastic mean value is not greatly affected by considered input random variables, namely: wind direction and velocity at the reference height. Comparing the variation of experimental data and the 95% confidence interval calculated by MF-NIPC, on the windward face ($0.0 \leq s/h < 1.0$) and the leeward face ($2.0 \leq s/h < 3.0$), the variation of the experimental data and the 95% confidence interval calculated by MF-NIPC has almost same range. It means that the variation of the experimental data can be caused by the input random variables considered in MF-NIPC. However, at the roof ($1.0 \leq s/h < 2.0$) the variation of the experimental data and the 95% confidence interval shows different range. At the observation point V8 (s=1.24), where the pressure coefficient takes minimum value, the 95% interval of MF-NIPC is much smaller than variation of the observation data. On the other hand, at observation points V9 - V11, where the pressure is recovering, the 95% interval of MF-NIPC is slightly bigger than variation of the experimental data. From this results, it can be expected that at the observation points V8, not the wind direction and the wind velocity at the reference height, but other uncertainties in the full scale observations, for example, geometry of the cube, turbulence intensity, the shape of the wind distribution and the measurement technique, may affect variation of the experimental data. Considering the shape of the pressure coefficient

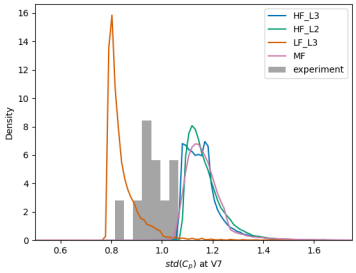

(a) V7

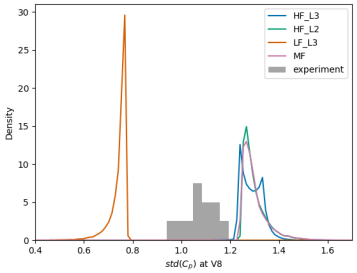

(b) V8

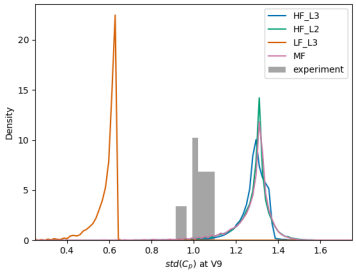

(c) V9

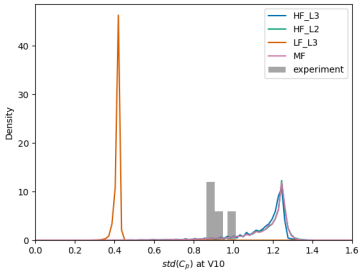

(d) V10

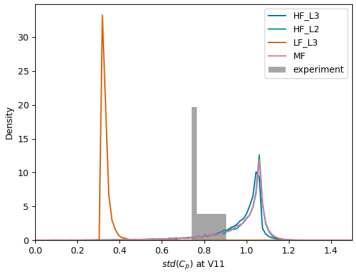

(e) V11

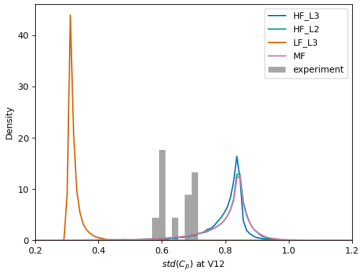

(f) V12

Figure 5.21: Probability Density Function of the standard deviation of pressure coefficient at the pressure tap (a) V7 (b) V8 (c) V9 (d) V10 (e) V11 (f) V12, calculated by the high-fidelity model with sparse grid level 2(HF_L2, green), the high-fidelity model with sparse grid level 2(HF_L3, blue), the low-fidelity model with sparse grid level 3(LF_L3, orange) and the multi-fidelity model (MF, pink). The experimental results from Richards et al. [120] are also plotted.

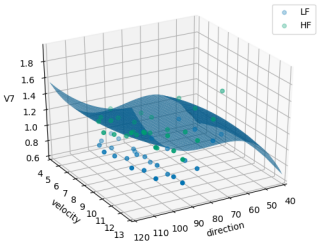

(a) V7

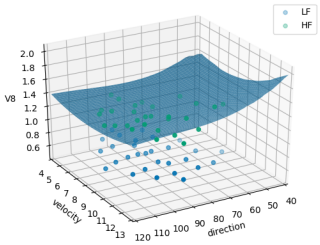

(b) V8

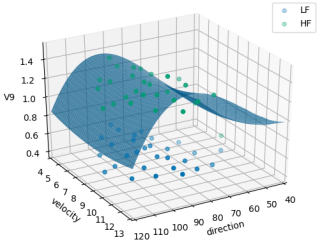

(c) V9

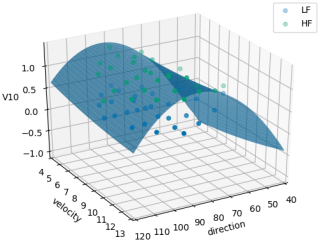

(d) V10

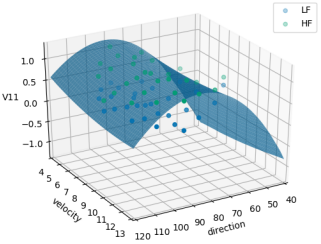

(e) V11

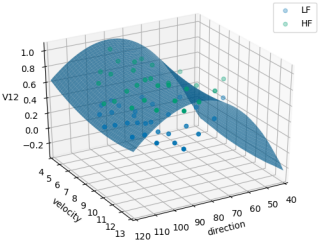

(f) V12

Figure 5.22: Response surface of the standard deviation of pressure coefficient at the pressure tap (a) V7 (b) V8 (c) V9 (d) V10 (e) V11 (f) V11, calculated by the high-fidelity model(HF), the low-fidelity model (LF) and the multi-fidelity model (MF).

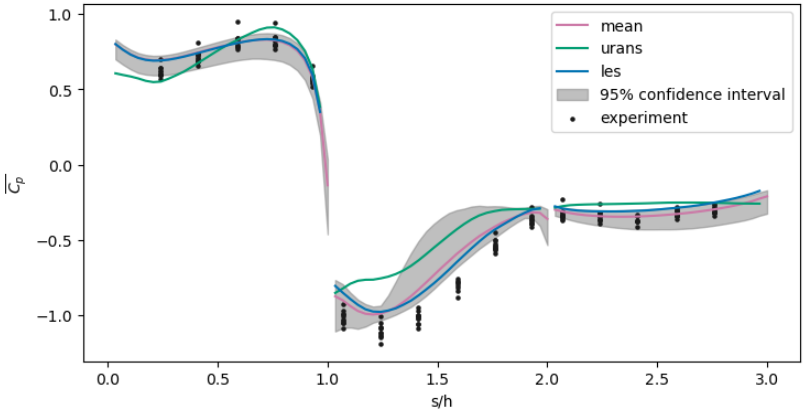

Figure 5.23: the pressure coefficient distribution on the vertical ring of the cube of mean calculated by MF-NIPC(pink), 95% confidence interval calculated by bootstrapping of the result of MF-NIPC(grey), LES deterministic simulation(blue), URANS deterministic simulation(green) and the experimental data(black)

distribution on the roof ($1.0 \leq s/h < 2.0$), after minimum pressure coefficient at V8 the flow reattachment to the roof happens. The larger gradient of the pressure coefficient means faster reattachment, in other words, gradient of the pressure coefficient distribution at the roof ($1.0 \leq s/h < 2.0$) shows flow separation and reattachment process. Fig. 5.24 shows the gradient of the pressure coefficient distribution between each observation points calculated from the pressure coefficient distribution in Fig. 5.23. After minimum pressure at V8 the pressure recovers, the positive bigger gradient means faster pressure recovery. About the gradient between V9 - V10 the variation of experiment data and the MF-NIPC results matches very well, otherwise the MF-NIPC results are more variant compared to experiment results, especially at V8 - V9, where the beginning of pressure recovery. At V8-V9 the gradient calculated by MF-NIPC is bigger than the experimental data, it is to say that the pressure recovers faster in MF-NIPC results than the experiment data. The reason of this fast pressure recovery in MF-NIPC can be caused by either:

1. the computational simulation overestimate the effect of input uncertainties, namely: velocity at the reference height and wind direction or

2. uncertainties, which are not considered in the MF-NIPC, controls reattachment more than the considered input uncertainties

Considering 1), the CFD simulations have been validated for wind direction 92° and 64° in Section 5.2.4 for both LES and URANS simulations (See

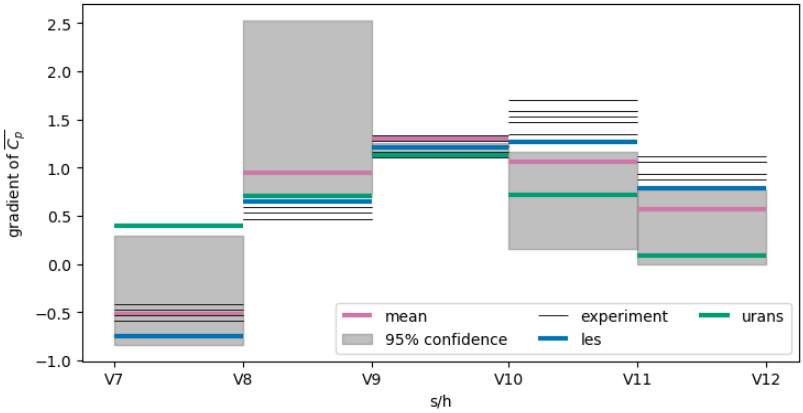

Figure 5.24: gradient of the pressure coefficient distribution on the vertical ring of the cube of mean calculated by MF-NIPC(pink), 95% confidence interval calculated by bootstrapping of the result of MF-NIPC(grey), LES deterministic simulation(blue), URANS deterministic simulation(green) and the experimental data(black)

Fig.5.15 and Fig. 5.15). As we discussed, the pressure coefficient on the vertical ring calculated from CFD simulations matched well in both value and trend, though both CFD simulations underestimate the minimum pressure coefficient at V8. In addition to the previous validation, let us consider correlation of CFD results and experimental data again, in this time using CFD results obtained in UQ process. Since only the wind direction and the pressure coefficients value are recorded for the experimental data, the correlation between CFD results and experimental data with respect to the wind direction will be compared. In Fig. 5.25, $\overline{C_p}$ which has the same wind direction are plotted. Since the PDF of HF(L3) and MF converge well, we now focus only on HF results. From Fig. 5.25, it can be seen that, though the HF results under estimate $\overline{C_p}$ than experimental data, the correlation between HF results and experimental results can be seen for both observation taps V8 and V9. Therefore we suggest that it is less likely that the MF-NIPC significantly overestimates the effect of input uncertainties.

Considering 2), it has been known that the experimental data of the roof shows patterns which cannot be explained and may be associated with the approaching turbulence intensity variation. It is to say that the roof top pressure reattachment on the center line of the cube can be controlled rather by the inlet turbulence intensity variation than input uncertainties which are used in this case, namely: the reference velocity and angle of attack. In the WindGen (Andre [8]), which is the software used in this chapter to generate the time varying input inlet velocity, the turbulence intensity is not a direct

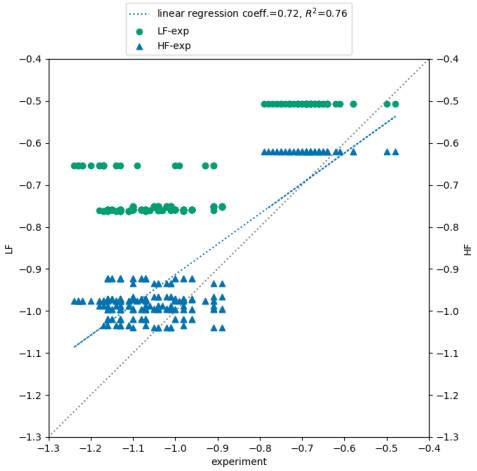

(a) V8

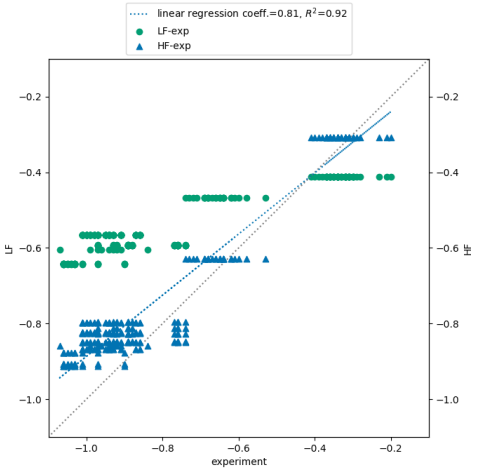

(b) V9

Figure 5.25: Correlation between experimental data and CFD simulations HF(blue) and LF(green) at observation point (a)V8 and (b)V9. $\overline{C_p}$ which has the same wind direction are plotted. The grey line show $y = x$, which means that the experimental data and the HF simulations data are completely correlated. The blue dotted line shows linear regression of plots for HF and experimental data

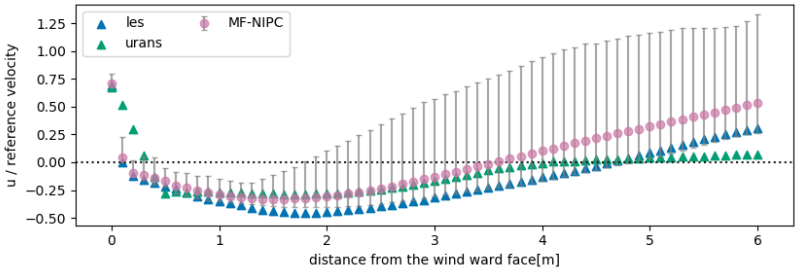

Figure 5.26: time averaged velocity coefficient (velocity component perpendicular to the windward face divided by the reference velocity) 60mm above the cube calculated by MF-NIPC(pink), 95% confidence interval calculated by bootstrapping of the result of MF-NIPC(grey), LES deterministic simulation(blue) and URANS deterministic simulation(green)

input parameter but calibrated using another parameter, and it requires a huge amount of effort to find out the appropriate parameter to reproduce the required turbulence intensity. It was the reason why the turbulence intensity is not chosen as an input random variable, however future research on this topic will seek to address this issue.

In order to further analyze the recirculation of the flow above the roof, let us look at the time averaged velocity 60 mm above the cube. Fig. 5.26 shows the time averaged velocity coefficient 60 mm above the cube calculated by MF-NIPC, LES deterministic simulation and URANS deterministic simulations. The results of MF-NIPC consists of its mean value and 95% confidence interval. The velocity coefficients are calculated by dividing velocity component perpendicular to the windward face by the reference velocity. The negative velocity coefficient means that there is the recirculation 60 mm above the roof. Comparing the result of MF-NIPC and the LES deterministic simulation, starting point of the recirculation is almost same in both results, however in the MF-NIPC the recirculation is smaller than in the LES deterministic simulation. This tendency is consistent to the results of pressure coefficient, as MF-NIPC shows the faster pressure recovery.

Having considered the pressure and velocity distribution, we can now conclude that the input uncertainties, the reference velocity and the wind direction, affects the size of the recirculation. The input uncertainties make the recirculation above the roof smaller and the pressure recovery faster than without considering the uncertainties.

Now let us move on to the time averaged pressure coefficient of the pressure taps on the roof of the cube. The numbering of the pressure taps on the roof is shown in Fig. 5.3. The experimental data for the roof taps are limited compared to the pressure distribution data on the vertical ring. Row

6 corresponds to the center line of the cube, and C1R6, C3R6 and C5R6 correspond to V7, V8 and V9 respectively. Looking at Fig. 5.27, unlike the pressure coefficient on the vertical ring shown in Fig. 5.23, the result calculated by LES deterministic simulation and the mean calculated by MF-NIPC have discrepancies especially close to the edge row of the cube (R1). The discrepancy between the LES deterministic result and the mean calculated by MF-NIPC decreases as it goes to the center row (R5). The absolute value of the pressure coefficient of the LES deterministic results are closer to the experimental data especially close to the center column (C5) than mean value of MF-NIPC, however trend of the mean value of MF-NIPC shows matches better to trend of the experimental data. Especially at the edge row (R1), the pressure coefficient shows minimum suction at the corner of the cube (R1C1), as observed in Richards et al. [123]. To further investigate pressure distribution of the roof, the time averaged pressure contour is drawn in Fig. 5.29 (a) calculated by a LES deterministic simulation and (b) mean of MF-NIPC. From the result of the LES deterministic simulation, the maximum suction (:the minimum pressure) occurs not at specific corner but in area close to windward face. However, the mean of MF-NIPC shows that the minimum suction occurs at the corner of the cube. According to Banks et al. [12], if the wind direction is aligned to the wind-ward face of the structure, the minimum suction occur at the corner of the roof because of the corner vortices. Having considered that MF-NIPC takes into account the variation of the wind direction, it is reasonable that the result of the MF-NIPC shows the minimum suction at the corner. Fig. 5.29 shows standard deviation of the time averaged pressure calculated by MF-NIPC. From Fig. 5.29, it can be seen that the variation of pressure becomes large in the region close to the windward face, where the suction occurs as seen in Fig. 5.29. In addition, there are also variations at the side edges of the cube. We suggest that it is because the region where minimum suction occurs changes depending on the wind direction, as with aligned wind the minimum suction occurs at the edge of the roof.

5.4 Conclusion

In this chapter MF-NIPC is applied to the Silsoe cube problem. In order to investigate effect of uncertainties exists in the full scale observation, the wind direction and the velocity at the reference height are considered as input random variables and the uncertainties are propagated to quantity of interests. To carry out the MF-NIPC, the LES simulations are used as a high-fidelity model and the URANS simulations are used as a low-fidelity model. Though a relatively coarse mesh is chosen as the low-fidelity simulation, we observed that the multi-fidelity framework improves the stochastic results compared to the single-fideliy NIPC in terms of the time averaged- and the time stand deviation of the pressure coefficient on the roof. Considering the 45.5 % computational time reduction of the multi-fidelity framework from the single-fidelity model, we confirmed that it is reasonable to use the multi-fidelity framework. After the accuracy of MF-NIPC is confirmed, the pressure coefficients calculated by

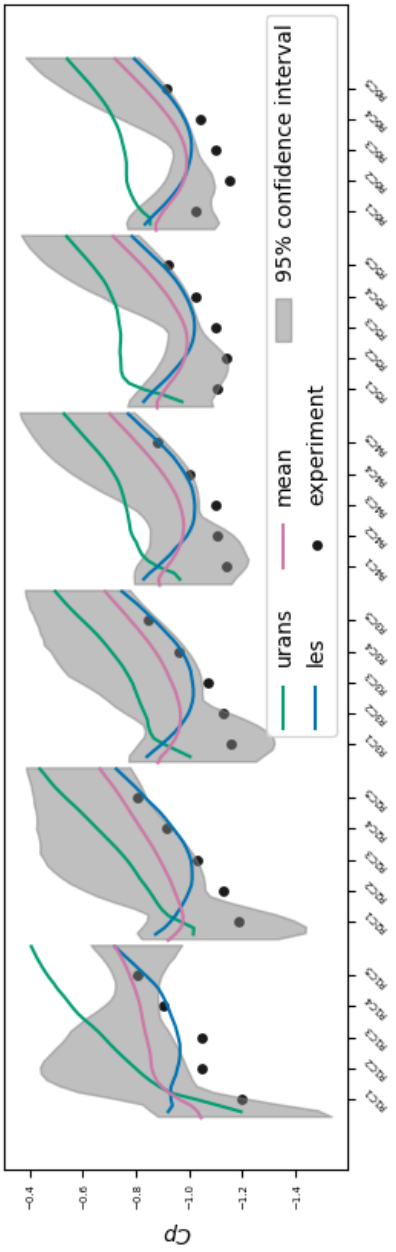

Figure 5.27: Comparison of the time averaged pressure coefficient $\overline{C_p}$ on pressure taps on the roof of the cube shown in Fig. 5.3. $\overline{C_p}$ are calculated by MF-NIPC(pink), 95% confidence interval calculated by bootstrapping of the result of MF-NIPC(grey), URANS deterministic simulation(green), LES deterministic simulation(blue) and experimental data(black)

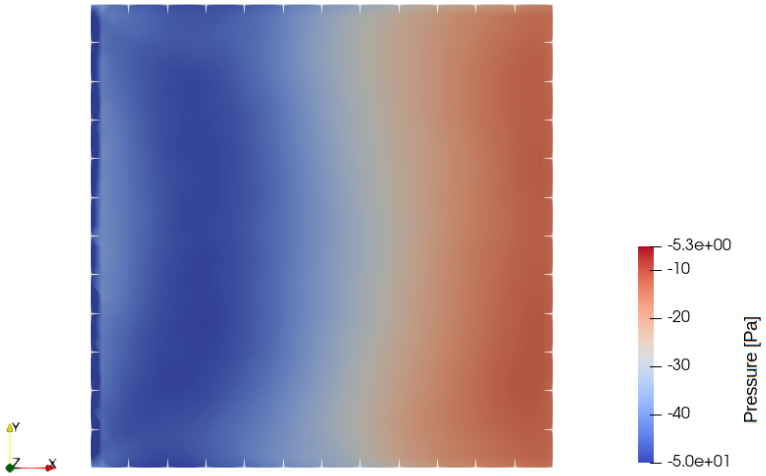

(a)

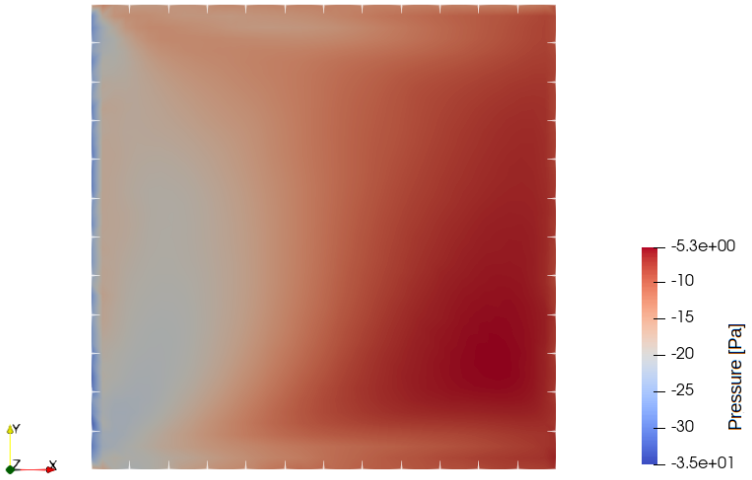

(b)

Figure 5.28: Time averaged pressure contour of the roof of (a) LES deterministic simulation result and (b) mean of MF-NIPC

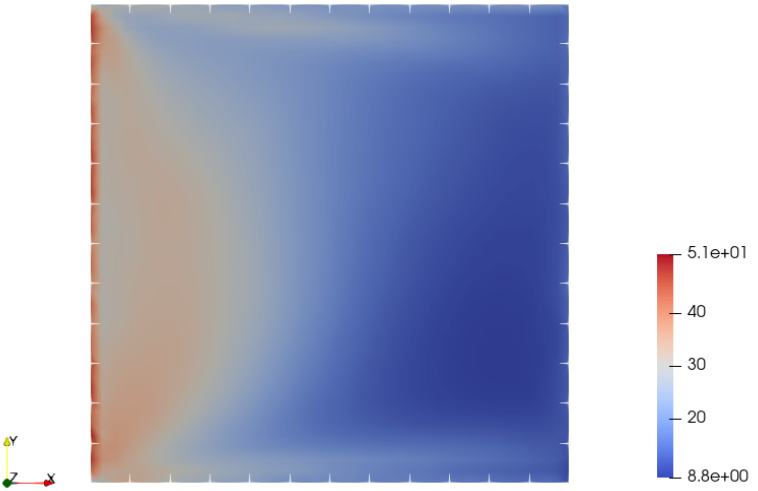

Figure 5.29: Standard deviation of time averaged pressure contour of the roof calculated by MF-NIPC

the MF-NIPC is compared with the deterministic results of the LES simulation and the URANS simulation and the experimental data given from the full scale observation. Considering pressure coefficient distribution at the taps of the roof, by taking into account the input uncertainties, UQ could express that the minimum suction occurs at the corner of the roof, which matches to the full scale observation. This is also confirmed from the counter of the mean value calculated by MF-NIPC. Considering pressure coefficient distribution on the center line of the cube, it is found that considered uncertainties affect characteristics of the recirculation of the flow and the pressure recovery on the roof of the cube. It is observed that in the MF-NIPC results the recirculation area above the roof becomes smaller and the pressure recovery happens faster than a deterministic simulation evaluated with the mean value of the input random variables. On the other hand, having compared the MF-NIPC results with the experimental data, the variation obtained by the MF-NIPC is smaller than the variation of the experimental data and this cannot be explained from currently obtained results. It is suggested in future to include the turbulence intensity as an input random variables.

I would like to acknowledge Prof. Peter J. Richards for kindly providing the full scale observation data sets.

Chapter 6

Conclusions and outlook

In this thesis the Multi-Fidelity Non-Intrusive Polynomial Chaos methods were applied to computational wind engineering problems. Though computational wind simulations include uncertainties, the uncertainty analysis has not been popular in the computational wind engineering field. It is because, the computational wind engineering problems have high Reynolds number compared to mechanical engineering problems and are computationally expensive. Since the uncertainty analysis requires number of deterministic simulations, it has been difficult to apply the uncertainty analysis to the computational wind engineering problems. To overcome this problem, we introduced the multi-fidelity framework. The multi-fidelity framework has been getting attention mainly for the optimization, which is not common in the computational wind engineering, and in this thesis the multi-fidelity uncertainty quantification is applied for the first time to the computational engineering problems.

To carry out the multi-fidelity analysis the Large Eddy Simulations were used as the high-fidelity model and the Unsteady Reynolds Averaged Navier-Stokes simulations were used as the low-fidelity model. Both CFD simulations are discretized by Finite Element Method, which has an advantage to express accurate geometry. As target problems we chose two well-documented benchmark cases in the computational engineering problems, namely: the Benchmark on Aerodynamics of a Rectangular 5:1 Cylinder (BARC) problem and flow around the Silsoe 6 m cube problem. The rectangular shape used in BARC problem plays an important role in architectural design and BARC focuses on analyzing the flow around the rectangular shape. In this thesis the curvature of the rectangular cylinder and the angle of attack are considered as input random variables for the purpose of validation of CFD simulations with the experiment data of the wind tunnel tests. It is confirmed by comparing the results of the bulk parameters calculated by the multi-fidelity models and single-fidelity models that the multi-fidelity framework could improve the

accuracy of uncertainty analysis. Then results of the uncertainty analysis was compared with the experimental results. It was observed that the multi-fidelity results are more comparable to the experimental data than the deterministic simulations evaluated at the mean value of the input random variables. From this study we conclude that the common uncertainties in the wind tunnel tests affect the pressure distribution especially in the region of the pressure recovery.

The other benchmark case is flow around the Silsoe 6m cube problem, which represents natural inflow problems. The architectural structures are located in the atmospheric boundary layer, in which the wind velocity is affected by ground surface. The Silsoe cube problem is a well-documented benchmark problem for a low-rise building located at the open terrain, and the full scale observation had been carried out. In this thesis the wind direction and the velocity at the cube height were considered as input random variables for the purpose of validation of CFD simulations with experiment data of the full scale observation. The accuracy of the multi-fidelity framework was confirmed by comparing PDF results with ones calculated from the single-fidelity model, even though comparably coarse mesh was chosen as the low-fidelity model. By using the multi-fidelity analysis we could save 45% of calculation time compared to the single-fidelity model. Then the results of the multi-fidelity model was compared with the experimental data. It was observed that the multi-fidelity model can demonstrate that the minimum suction on the roof occurs at the corner of the roof, which is compatible with the experiment data of the full scale observation.

By investigating two well-known benchmark cases in the computational wind engineering, we demonstrated the applicability of MF-NIPC to practical computational engineering problems. By comparing the multi-fidelity results with single-fidelity results, we confirmed that the multi-fidelity framework could improve the accuracy. Both studies were carried out for the purpose of validation of the CFD simulations with the experimental data, and we observed that the multi-fidelity analysis gives more compatible results to the experimental data than the deterministic simulations evaluated at the mean value of input random variables. In addition we observed significant computational time saving especially for the Silsoe cube problem. Practically, it requires great effort to set up the CFD simulations at the collocation points calculated by the polynomial chaos methods, as it was observed to express change of the curvature in BARC problems. The Finite Element Method based CFD has strong advantage to simulate accurate geometries. In future more research would be necessary with respect to change inlet wind velocity for natural wind, so that inlet wind direction and the turbulence intensity can be easily set to value at the collocation points without remeshing.

Appendix A

Polynomial Chaos based Sobol's indices

Polynomial Chaos Expansion (PCE) of Y is written as:

$$Y = g(\mathbf{X}) \approx \sum_{k=1}^{P} a_k \Psi_k(\mathbf{X}), \tag{A.1}$$

where $\mathbf{X} = (X_1, ..., X_n)$ is the input random variables and $\Psi_k(\mathbf{X})$ is the orthogonal polynomials. Let us assume a multivariate polynomial orthogonal as:

$$\Psi_j \equiv \Psi_\alpha : \Psi_j(\mathbf{X}) = \prod_{i=1}^{n} P_{\alpha_i}(x_i), \tag{A.2}$$

where $P_k(x)$ is the k th orthogonal polynomial and $\alpha = (\alpha_1, \ldots, \alpha_n)$. Let us define $\mathscr{I}_{\{i_1,\ldots,i_s\}}$, the set of α as:

$$\mathscr{I}_{i_1,\ldots,i_s} = \left\{ \begin{array}{llll} \alpha_k > 0 & \forall k = 1, \ldots, n, & k \in (i_1, \ldots, i_s) \\ \alpha_j = 0 & \forall k = 1, \ldots, n, & k \notin (i_1, \ldots, i_s) \end{array} \right\}. \tag{A.3}$$

The polynomial chaos based Sobol decomposition is written as:

$$\begin{aligned} g_{\mathrm{PC}}(\mathbf{X}) =& g_0 + \sum_{i=1}^{n} \sum_{\alpha \in \mathscr{I}_i} g_\alpha \Psi_\alpha \left(X_i\right) \\ &+ \sum_{1 \leqslant i_1 < i_2 \leqslant n} \sum_{\alpha \in \mathscr{I}_{i_1,i_2}} g_\alpha \Psi_\alpha \left(X_{i_1}, X_{i_2}\right) + \cdots \\ &+ \sum_{1 \leqslant i_1 < \cdots < i_s \leqslant n} \sum_{\alpha \in \mathscr{I}_{i_1,\ldots,i_s}} g_\alpha \Psi_\alpha \left(X_{i_1}, \ldots, X_{i_s}\right) \\ &+ \cdots + \sum_{\alpha \in \mathscr{I}_{1,2\ldots n}} g_\alpha \Psi_\alpha \left(X_1, \ldots, X_n\right). \end{aligned} \tag{A.4}$$

Having considered the polynomial chaos based Sobol decomposition, the Sobol's indices $SU_{i_1,\ldots,i_s}$ is written as:

$$SU_{i_1,\ldots,i_s} = \sum_{\alpha \in \mathscr{I}_{i_1,\ldots,is}} g_\alpha^2 \mathrm{E}\left[\Psi_\alpha^2\right] / D_{\mathrm{PC}}, \tag{A.5}$$

where D_{PC} is the total variance.

Appendix B

Sparse quadrature (Smolyak rule)

Sparse quadrature method for the Gauss quadrature Q_{q_j} is written as:

$$Q_{d,k} = \sum_{k-d}^{k-1} (-1)^{(k-1-i)} \binom{d-1}{k-1-i} \sum_{q \in N_i^d} Q_{q_1} \otimes \dots Q_{q_d}. \tag{B.1}$$

An advantage to use the sparse quadrature instead of the Gauss quadrature ever for small number of input random variables is what the collocation points calculated by the sparse grid are nested. Fig. B.1 shows the collocation points calculated by the Gauss quadrature methods for the polynomial order 2 and 3 and the sparse quadrature methods for the sparse grid level 2 and 3 for the input random variables of BARC, namely angle of attack as a normal distribution with a mean of 0.0 and standard deviation 0.51 and the curvature radius r/D with a uniform distribution in $(0, 0.054)$. The collocation points calculated by the Gauss quadrature are not nested at all, while about the collocation points calculated by the sparse quadrature 11 points of level 3 are included in the points for level 2. In order to carry out MF-NIPC, the nested collocation points play an important role, since the low-fidelity model should be run at the collocation points of both level 2 and level 3. Therefore in this thesis the sparse grid method has been used in this thesis, though the dimension of input random variables are not high.

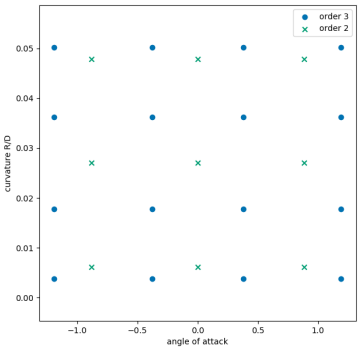

(a)

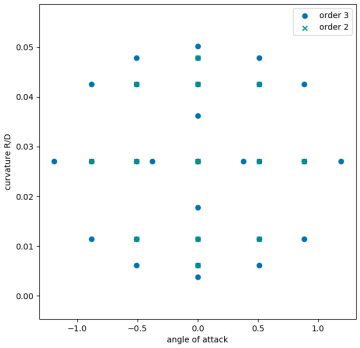

(b)

Figure B.1: Comparison of the collocation points calculated by (a) the Gauss quadrature for polynomial order 2 and 3 (b) the sparse quadrature for sparse grid level 2 and 3

List of Figures

List of Tables

Bibliography

[1] *a Benchmark on the Aerodynamics of a Rectangular 5:1 Cylinder*. Italian National Association for Wind Engineering (ANIV).

[2] A. K. Abodonya. "Verification methodology for computational wind engineering prediction of wind loads on structures". PhD thesis. 2019.

[3] I. Abohela, N. Hamza, and S. Dudek. "Validating CFD Simulation Results: Wind flow around a surface mounted cube in a turbulent channel flow". In: *28th Conference, Opportunities, Limits Needs Towards an environmentally responsible architecture*. Lima, Peru, 2012.

[4] R. Ahlfeld, B. Belkouchi, and F. Montomoli. "SAMBA: Sparse Approximation of Moment-Based Arbitrary Polynomial Chaos". In: *Journal of Computational Physics* 320 (2016), pp. 1–16. DOI: 10.1016/j.jcp.2016.05.014.

[5] R. Ak, V. Vitelli, and E. Zio. "An interval-valued neural network approach for uncertainty quantification in short-term wind speed prediction". In: *IEEE transactions on neural networks and learning systems* 26.11 (2015), pp. 2787–2800. DOI: 10.1109/TNNLS.2015.2396933..

[6] American Society of Civil Engineers. *ASCE 7: Minimum Design Loads for Buildings and Other Structures*. 2013.

[7] M. Andre. "Aeroelastic modeling and simulation for the assessment of wind effects on a parabolic trough solar collector". PhD thesis. Technical University of Munich, 2018.

[8] M. Andre. *WindGen*. 2017. URL: https://github.com/msandre/WindGen.

[9] M. S. Andre. "Aeroelastic modeling and simulation for the assessment of wind effecs on a parabolic trough solar collector". PhD thesis. 2018.

[10] Architectural Institute of Japan. *AIJ Recommendations for Loads on Buildings*. 2015.

[11] Architectural Institute of Japan. *Guidebook of Recommendations for Loads on Buildings 2 – Wind induced Response and Load Estimation/Practical Guide of CFD for Wind Resistant Designs*. 2017.

[12] D. Banks, R. Meroney, P. Sarkar, Z. Zhao, and F. Wu. "Flow visualization of conical vortices on flat roofs with simultaneous surface pressure measurement". In: *Journal of Wind Engineering and Industrial Aerodynamics* 84.1 (2000), pp. 65–85. DOI: 10.1016/S0167-6105(99)00044-6.

[13] Y. Bazilevs and T. J. Hughes. "Weak imposition of Dirichlet boundary conditions in fluid mechanics". In: *Computers & Fluids* 36.1 (2007), pp. 12–26. DOI: 10.1016/j.compfluid.2005.07.012.

[14] E. Bernardini, S. M. Spence, D. Wei, and A. Kareem. "Aerodynamic shape optimization of civil structures: A CFD-enabled Kriging-based approach". In: *Journal of Wind Engineering and Industrial Aerodynamics* 144 (2015), pp. 154–164. DOI: 10.1016/j.jweia.2015.03.011.

[15] B. Blocken. "50 years of Computational Wind Engineering: Past, present and future". In: *Journal of Wind Engineering and Industrial Aerodynamics* 129 (June 2014), pp. 69–102. DOI: 10.1016/j.jweia.2014.03.008.

[16] B. Blocken, T. Stathopoulos, J. Carmeliet, and J. L. Hensen. "Application of computational fluid dynamics in building performance simulation for the outdoor environment: an overview". In: *Journal of Building Performance Simulation* 4.2 (June 2011), pp. 157–184. DOI: 10.1080/19401493.2010.513740.

[17] R. Bradley. "CFD Validation Philosophy". In: *AGARD Symposium on Validation of Computational Fluid Dynamics, Conf. Paper No. 1.* 1988.

[18] A. Bronkhorst, C. Geurts, and C. Van Bentum. "Unsteady pressure measurements on a 5: 1 rectangular cylinder". In: *Proceedings of the 13th International Conference on Wind Engineering, Amsterdam, The Netherlands*. Vol. 1015. 2011.

[19] L. Bruno, C. Canuto, and D. Fransos. "Stochastic aerodynamics and aeroelasticity of a flat plate via generalised polynomial chaos". In: *Journal of Fluids and Structures* 25.7 (2009), pp. 1158–1176. DOI: 10.1016/j.jfluidstructs.2009.06.001.

[20] L. Bruno and D. Fransos. "Probabilistic evaluation of the aerodynamic properties of a bridge deck". In: *Journal of wind engineering and industrial aerodynamics* 99.6-7 (2011), pp. 718–728. DOI: 10.1016/j.jweia.2011.03.007.

[21] L. Bruno, D. Fransos, N. Coste, and A. Bosco. "3D flow around a rectangular cylinder: a computational study". In: *Journal of Wind Engineering and Industrial Aerodynamics* 98.6-7 (2010), pp. 263–276. DOI: 10.1016/j.jweia.2009.10.005.

[22] L. Bruno, M. V. Salvetti, and F. Ricciardelli. "Benchmark on the aerodynamics of a rectangular 5: 1 cylinder: an overview after the first four years of activity". In: *Journal of Wind Engineering and Industrial Aerodynamics* 126 (2014), pp. 87–106. DOI: 10.1016/j.jweia.2014.01.005.

[23] C. Canuto and D. Fransos. "Numerical solution of partial differential equations in random domains: An application to wind engineering." In: vol. 5. 2-4. Citeseer, 2009, pp. 515–531.

[24] M. Carnevale, F. Montomoli, A. D'Ammaro, S. Salvadori, and F. Martelli. "Uncertainty quantification: A stochastic method for heat transfer prediction using LES". In: *Journal of Turbomachinery* 135.5 (2013), p. 051021. DOI: 10.1115/1.4007836.

[25] M. Casey, T. Wintergerste, T. European Research Community on Flow, and Combustion. *ERCOFTAC Best Practice Guidelines: ERCOFTAC Special Interest Group on "quality and Trust in Industrial CFD"*. ERCOFTAC, 2000.

[26] W.-C. Chuang and S. M. Spence. "Rapid uncertainty quantification for non-linear and stochastic wind excited structures: a metamodeling approach". In: *Meccanica* 54.9 (2019), pp. 1327–1338. DOI: 10.1007/s11012-019-00958-9.

[27] M. Ciampoli, F. Petrini, and G. Augusti. "Performance-based wind engineering: towards a general procedure". In: *Structural Safety* 33.6 (2011), pp. 367–378. DOI: 10.1016/j.strusafe.2011.07.001.

[28] "Climate change 2007: The physical science basis". In: *Agenda* 6.07 (2007), p. 333.

[29] R. Codina, J. Principe, O. Guasch, and S. Badia. "Time dependent subscales in the stabilized finite element approximation of incompressible flow problems". In: *Computer Methods in Applied Mechanics and Engineering* 196.21 (Apr. 2007), pp. 2413–2430. DOI: 10.1016/j.cma.2007.01.002.

[30] T. Connor, R. Niall, P. Cummings, and M. Papillo. "Incorporating Climate Change Adaptation into Engineering Design Concepts and Solutions". In: *Australian Journal of Structural Engineering* 14.2 (2013), pp. 125–134. DOI: 10.7158/13287982.2013.11465127.

[31] N. Cook. "The designer's guide to wind loading of buildings structures. Part 2: static structures". In: *BRE (Building Research Establishment)* (1985).

[32] J. Côté, S. Gravel, A. Méthot, A. Patoine, M. Roch, and A. Staniforth. "The operational CMC–MRB global environmental multiscale (GEM) model. Part I: Design considerations and formulation". In: *Monthly Weather Review* 126.6 (1998), pp. 1373–1395. DOI: 10.1175/1520-0493(1998)126<1373:TOCMGE>2.0.CO;2.

[33] J. Cousin and M. Metcalfe. "The bae (commercial aircraft) ltd transport aircraft synthesis and optimisation program (tasop)". In: *Aircraft Design, Systems and Operations Conference*. 1990, p. 3295. DOI: 10.2514/6.1990-3295.

[34] W. Cui and L. Caracoglia. "New GPU computing algorithm for wind load uncertainty analysis on high-rise systems". In: *Wind and Structures An International Journal* 21 (Nov. 2015), pp. 461–487. DOI: 10.12989/was.2015.21.5.461.

[35] J. C. Dalmau. "Applications of turbulence modeling in civil engineering". PhD thesis. 2016.

[36] Deutsches Institut für Normung e. V. *DIN EN 1991-1-4/NA, Nationaler Anhang - National festgelegte Parameter - Eurocode 1: Einwirkungen auf Tragwerke - Teil 1-4: Allgemeine Einwirkungen - Windlasten*. 2010.

[37] F. Ding and A. Kareem. "A multi-fidelity shape optimization via surrogate modeling for civil structures". In: *Journal of Wind Engineering and Industrial Aerodynamics* 178 (2018), pp. 49–56. DOI: 10.1016/j.jweia.2018.04.022.

[38] E. H. Dowell and K. C. Hall. "Modeling of fluid-structure interaction". In: *Annual review of fluid mechanics* 33.1 (2001), pp. 445–490. DOI: 10.1146/annurev.fluid.33.1.445.

[39] P. Du, W. Li, X. Ke, N. Lu, O. A. Ciniglio, M. Colburn, and P. M. Anderson. "Probabilistic-based available transfer capability assessment considering existing and future wind generation resources". In: *IEEE Transactions on sustainable Energy* 6.4 (2015), pp. 1263–1271. DOI: 10.1109/TSTE.2015.2425354.

[40] S. Dubreuil, M. Berveiller, F. Petitjean, and M. Salaün. "Construction of bootstrap confidence intervals on sensitivity indices computed by polynomial chaos expansion". In: *Reliability Engineering System Safety* 121 (Jan. 2014), pp. 263–275. DOI: 10.1016/j.ress.2013.09.011.

[41] P. A. Durbin and B. P. Reif. *Statistical theory and modeling for turbulent flows*. John Wiley & Sons, 2011.

[42] B. Efron. "Bootstrap Methods: Another Look at the Jackknife". In: *Breakthroughs in Statistics: Methodology and Distribution*. Ed. by S. Kotz and N. L. Johnson. New York, NY: Springer New York, 1992, pp. 569–593. DOI: 10.1007/978-1-4612-4380-9_41.

[43] M. Eldred, L. Ng, M. Barone, and S. Domino. "Multifidelity Uncertainty Quantification Using Spectral Stochastic Discrepancy Models". In: Jan. 2015, pp. 1–45. DOI: 10.1007/978-3-319-11259-6_25-1.

[44] M. S. Eldred, L. W. T. Ng, M. F. Barone, and S. P. Domino. "Multifidelity Uncertainty Quantification Using Spectral Stochastic Discrepancy Models". In: *Handbook of Uncertainty Quantification*. Ed. by R. Ghanem, D. Higdon, and H. Owhadi. Cham: Springer International Publishing, 2015, pp. 991–1040.

[45] M. Eldred, L. Ng, M. Barone, and S. Domino. "Multifidelity uncertainty quantification using spectral stochastic discrepancy models". In: ed. by R. Ghanem, D. Higdon, and H. Owhadi. Vol. 6. Springer, 2017, pp. 991–1036.

[46] European Committee for standardization. *EN 1991-1-4:2005+A1, Eurocode 1: Actions on structures -Part 1-4: General actions -Wind actions*. 2010.

[47] J. Feinberg and H. P. Langtangen. "Chaospy: An open source tool for designing methods of uncertainty quantification". In: *Journal of Computational Science* 11 (2015), pp. 46–57. DOI: 10.1016/j.jocs.2015.08.008.

[48] V. M. Ferrándiz, P. Bucher, R. Rossi, R. Zorrilla, J. Cotela, J. Maria, M. A. Celigueta, and G. Casas. *KratosMultiphysics (Version 8.1)*. https://zenodo.org/record/3234644. Nov. 2020.

[49] A. I. Forrester, A. Sóbester, and A. J. Keane. "Multi-fidelity optimization via surrogate modelling". In: *Proceedings of the royal society a: mathematical, physical and engineering sciences* 463.2088 (2007), pp. 3251–3269. DOI: 10.1098/rspa.2007.1900.

[50] J. Franke, C. Hirsch, A. Jensen, H. Krüs, M. Schatzmann, P. Westbury, S. Miles, J. Wisse, and N. Wright. "Recommendations on the use of CFD in predicting pedestrian wind environment". In: *Cost action C*. Vol. 14. 2004.

[51] J. Franke, C. Hirsch, G. Jensen, H. Krüs, S. Miles, M. Schatzmann, P. Westbury, J. Wisse, and N. Wright. "Recommendations on the use of CFD in wind engineering". English. In: *Proceedings of the International Conference on Urban Wind Engineering and Building Aerodynamics*. 2004, pp. C.1.1–C1.11.

[52] J. Franke, A. Hellsten, K. H. Schluenzen, and B. Carissimo. "The COST 732 Best Practice Guideline for CFD simulation of flows in the urban environment: a summary". eng. In: *International Journal of Environment and Pollution* 44.1-4 (2011), pp. 419–427. DOI: 10.1504/IJEP.2011.038443.

[53] C. Garcıéa-Sánchez and C. Gorlé. "Uncertainty quantification for microscale CFD simulations based on input from mesoscale codes". In: *Journal of Wind Engineering and Industrial Aerodynamics* 176 (2018), pp. 87–97. DOI: 10.1016/j.jweia.2018.03.011.

[54] C. Garcıéa-Sánchez, D. Philips, and C. Gorlé. "Quantifying inflow uncertainties for CFD simulations of the flow in downtown Oklahoma City". In: *Building and environment* 78 (2014), pp. 118–129. DOI: 10.1016/j.buildenv.2014.04.013.

[55] C. Garcıéa-Sánchez, G. Van Tendeloo, and C. Gorlé. "Quantifying inflow uncertainties in RANS simulations of urban pollutant dispersion". In: *Atmospheric environment* 161 (2017), pp. 263–273. DOI: 10.1016/j.atmosenv.2017.04.019.

[56] M. Gasca and T. Sauer. "Polynomial interpolation in several variables". In: *Advances in Computational Mathematics* 12.4 (2000), pp. 377–410. DOI: 10.1023/A:1018981505752.

[57] N. Geneva and N. Zabaras. "Quantifying model form uncertainty in Reynolds-averaged turbulence models with Bayesian deep neural networks". In: *Journal of Computational Physics* 383 (2019), pp. 125–147. DOI: 10.1016/j.jcp.2019.01.021.

[58] M. Giselle Fernández-Godino, C. Park, N. H. Kim, and R. T. Haftka. "Issues in deciding whether to use multifidelity surrogates". In: *AIAA Journal* 57.5 (2019), pp. 2039–2054. DOI: 10.2514/1.J057750.

[59] M. B. Goldsmith, B. V. Sankar, R. T. Haftka, and R. K. Goldberg. "Effects of microstructural variability on thermo-mechanical properties of a woven ceramic matrix composite". In: *Journal of Composite Materials* 49.3 (2015), pp. 335–350. DOI: 10.1177/0021998313519151.

[60] G. H. Golub and J. H. Welsch. "Calculation of Gauss Quadrature Rules". In: *Math. Comp.* 23 (1969), pp. 221–230. DOI: 10.1090/S0025-5718-69-99647-1.

[61] C. Gorlé, S. Zeoli, M. Emory, J. Larsson, and G. Iaccarino. "Epistemic uncertainty quantification for Reynolds-averaged Navier-Stokes modeling of separated flows over streamlined surfaces". In: *Physics of Fluids* 31.3 (2019), p. 035101. DOI: 10.1063/1.5086341.

[62] C. Gorlé, C. Garcia-Sanchez, and G. Iaccarino. "Quantifying inflow and RANS turbulence model form uncertainties for wind engineering flows". In: *Journal of Wind Engineering and Industrial Aerodynamics* 144 (2015), pp. 202–212. DOI: 10.1016/j.jweia.2015.03.025.

[63] R. Guichard. "Large eddy simulation of pressure fluctuations on a surface-mounted cube". In: *Proc. For the 7th European-African Conference on Wind Engineering*. 2017.

[64] *Guide for the Verification and Validation of Computational Fluid Dynamics Simulations*. American Institute of Aeronautics and Astronautics. 1998.

[65] T. A. Helgedagsrud, Y. Bazilevs, A. Korobenko, K. M. Mathisen, and O. A. Øiseth. "Using ALE-VMS to compute aerodynamic derivatives of bridge sections". In: *Computers & Fluids* 179 (2019), pp. 820–832. DOI: 10.1016/j.compfluid.2018.04.037.

[66] T. van Hooff, B. Blocken, J. Hensen, and H. Timmermans. "On the predicted effectiveness of climate adaptation measures for residential buildings". In: *Building and Environment* 82 (2014), pp. 300–316. DOI: 10.1016/j.buildenv.2014.08.027.

[67] S. Hosder, R. W. Walters, and M. Balch. "Point-collocation nonintrusive polynomial chaos method for stochastic computational fluid dynamics". In: *AIAA journal* 48.12 (2010), pp. 2721–2730. DOI: 10.2514/1.39389.

[68] K. Hourigan, M. Thompson, and B. Tan. "SELF-SUSTAINED OSCILLATIONS IN FLOWS AROUND LONG BLUNT PLATES". In: *Journal of Fluids and Structures* 15.3 (Apr. 2001), pp. 387–398. DOI: 10.1006/jfls.2000.0352.

[69] T. J. Hughes. "Multiscale phenomena: Green's functions, the Dirichlet-to-Neumann formulation, subgrid scale models, bubbles and the origins of stabilized methods". In: *Computer Methods in Applied Mechanics and Engineering* 127.1 (1995), pp. 387–401. DOI: 10.1016/0045-7825(95)00844-9.

[70] L. Huyse and R. W. Walters. *Random field solutions including boundary condition uncertainty for the steady-state generalized Burgers equation*. Tech. rep. NATIONAL AERONAUTICS and SPACE ADMINISTRATION HAMPTON VA LANGLEY RESEARCH CENTER, 2001.

[71] G. Iaccarino, A. Ooi, P. Durbin, and M. Behnia. "Reynolds averaged simulation of unsteady separated flow". In: *International Journal of Heat and Fluid Flow* 24.2 (Apr. 2003), pp. 147–156. DOI: 10.1016/S0142-727X(02)00210-2.

[72] D. I. Jeong and L. Sushama. "Projected changes to extreme wind and snow environmental loads for buildings and infrastructure across Canada". In: *Sustainable cities and society* 36 (2018), pp. 225–236. DOI: 10.1016/j.scs.2017.10.004.

[73] J. Jin, Y. Che, J. Zheng, and F. Xiao. "Uncertainty Quantification of a Coupled Model for Wind Prediction at a Wind Farm in Japan". In: *Energies* 12.8 (2019), p. 1505. DOI: 10.3390/en12081505.

[74] A. Kareem. "Numerical simulation of wind effects: A probabilistic perspective". In: *Journal of Wind Engineering and Industrial Aerodynamics* 96.10–11 (Oct. 2008), pp. 1472–1497. DOI: 10.1016/j.jweia.2008.02.048.

[75] M. Kasperski and R. Hoxey. "Extreme-value analysis for observed peak pressures on the Silsoe cube". In: *Journal of wind engineering and industrial aerodynamics* 96.6-7 (2008), pp. 994–1002. DOI: 10.1016/j.jweia.2007.06.024.

[76] S. Kawai and K. Shimoyama. "Kriging-model-based uncertainty quantification in computational fluid dynamics". In: *32nd AIAA Applied Aerodynamics Conference*. 2014, p. 2737. DOI: 10.2514/6.2014-2737.

[77] L. Kleerekoper, A. van den Dobbelsteen, G. Hordijk, M. van Dorst, and C. Martin. "Climate adaptation strategies: achieving insight in microclimate effects of redevelopment options". In: *Smart and Sustainable Built Environment* (2015). DOI: 10.1108/SASBE-08-2014-0045.

[78] D. Kuzmin, R. Löhner, and S. Turek. *Flux-corrected transport: principles, algorithms, and applications*. Second. Scientific Computation. Springer, 2012. ISBN: 9789400740389.

[79] G. Lamberti and C. Gorlé. "Uncertainty Quantification for RANS Predictions of Wind Loads on Buildings". In: *Conference of the Italian Association for Wind Engineering*. Springer. 2018, pp. 402–412. DOI: 10.1007/978-3-030-12815-9_32.

[80] O. P. Le Maître and O. M. Knio. *Spectral methods for uncertainty quantification: with applications to computational fluid dynamics*. Scientific computation. Springer, 2010. ISBN: 9789048135196.

[81] G. Li and H. Hu. "Risk design optimization using many-objective evolutionary algorithm with application to performance-based wind engineering of tall buildings". In: *Structural Safety* 48 (2014), pp. 1–14. DOI: 10.1016/j.strusafe.2014.01.002.

[82] H. C. Lim, T. Thomas, and I. P. Castro. "Flow around a cube in a turbulent boundary layer: LES and experiment". In: *Journal of Wind Engineering and Industrial Aerodynamics* 97.2 (2009), pp. 96–109. DOI: 10.1016/j.jweia.2009.01.001.

[83] J. Ling and J. Templeton. "Evaluation of machine learning algorithms for prediction of regions of high Reynolds averaged Navier Stokes uncertainty". In: *Physics of Fluids* 27.8 (2015), p. 085103. DOI: 10.1063/1.4927765.

[84] A. Loeven, J. Witteveen, and H. Bijl. "Efficient uncertainty quantification using a two-step approach with chaos collocation". In: *European Conference on Computational FluidDynamics ECCOMAS CFD*. 2006.

[85] G. Loeven and H. Bijl. "Probabilistic collocation used in a two-step approach for efficient uncertainty quantification in computational fluid dynamics". In: *Computer Modelling in Engineering and Science* 36.3 (2008), pp. 193–212. DOI: 10.3970/cmes.2008.036.193.

[86] J. Mann. "The spatial structure of neutral atmospheric surface-layer turbulence". In: *Journal of fluid mechanics* 273 (1994), pp. 141–168. DOI: 10.1017/S0022112094001886.

[87] J. Mann. "Wind field simulation". In: *Probabilistic engineering mechanics* 13.4 (1998), pp. 269–282. DOI: 10.1016/S0266-8920(97)00036-2.

[88] C. Mannini, A. Šoda, and G. Schewe. "Numerical investigation on the three-dimensional unsteady flow past a 5: 1 rectangular cylinder". In: *Journal of Wind Engineering and Industrial Aerodynamics* 99.4 (2011), pp. 469–482. DOI: 10.1016/j.jweia.2010.12.016.

[89] C. Mannini, A. Šoda, and G. Schewe. "Unsteady RANS modelling of flow past a rectangular cylinder: Investigation of Reynolds number effects". In: *Computers & fluids* 39.9 (2010), pp. 1609–1624. DOI: 10.1016/j.compfluid.2010.05.014.

[90] L. Margheri and P. Sagaut. "A hybrid anchored-ANOVA–POD/Kriging method for uncertainty quantification in unsteady high-fidelity CFD simulations". In: *Journal of Computational Physics* 324 (2016), pp. 137–173. DOI: 10.1016/j.jcp.2016.07.036.

[91] A. Mariotti, M. Salvetti, P. Shoeibi Omrani, and J. Witteveen. "Stochastic analysis of the impact of freestream conditions on the aerodynamics of a rectangular 5:1 cylinder". In: *Computers Fluids* 136 (Sept. 2016), pp. 170–192. DOI: 10.1016/j.compfluid.2016.06.008.

[92] A. Mariotti, M. V. Salvetti, P. S. Omrani, and J. Witteveen. "Stochastic analysis of the impact of freestream conditions on the aerodynamics of a rectangular 5: 1 cylinder". In: *Computers & Fluids* 136 (2016), pp. 170–192. DOI: 10.1016/j.compfluid.2016.06.008.

[93] A. Mariotti, L. Siconolfi, and M. V. Salvetti. "Stochastic sensitivity analysis of large-eddy simulation predictions of the flow around a 5: 1 rectangular cylinder". In: *European Journal of Mechanics-B/Fluids* 62 (2017), pp. 149–165. DOI: 10.1016/j.euromechflu.2016.12.008.

[94] B. Maskew. "Prediction of subsonic aerodynamic characteristics: a case for low-order panel methods". In: *Journal of Aircraft* 19.2 (1982), pp. 157–163. DOI: 10.2514/3.57369.

[95] F. Menter. "Zonal two equation kw turbulence models for aerodynamic flows". In: *23rd fluid dynamics, plasmadynamics, and lasers conference*. 1993, p. 2906. DOI: 10.2514/6.1993-2906.

[96] A. Mochida and I. Y. Lun. "Prediction of wind environment and thermal comfort at pedestrian level in urban area". In: *Journal of Wind Engineering and Industrial Aerodynamics* 96.10–11 (Oct. 2008), pp. 1498–1527. DOI: 10.1016/j.jweia.2008.02.033.

[97] F. Montomoli, D. Amirante, N. Hills, S. Shahpar, and M. Massini. "Uncertainty quantification, rare events, and mission optimization: Stochastic variations of metal temperature during a transient". In: *Journal of Engineering for Gas Turbines and Power* 137.4 (2015). DOI: 10.1115/1.4028546.

[98] *muenchen.de Das offizielle Stadtportal*. URL: https://www.muenchen.de/.

[99] J. P. Murcia, P.-E. Réthoré, N. Dimitrov, A. Natarajan, J. D. Sørensen, P. Graf, and T. Kim. "Uncertainty propagation through an aeroelastic wind turbine model using polynomial surrogates". In: *Renewable Energy* 119 (2018), pp. 910–922. DOI: 10.1016/j.renene.2017.07.070.

[100] J. Murray and M. Barone. "The development of cactus, a wind and marine turbine performance simulation code". In: *49th AIAA Aerospace Sciences Meeting including the New Horizons Forum and Aerospace Exposition*. 2011, p. 147. DOI: 10.2514/6.2011-147.

[101] H. Nakaguchi, K. Hashimoto, and S. Muto. "An Experimental Study on Aerodynamic Drag of Rectangular Cylinders". In: *The Journal of the Japan Society of Aeronautical Engineering* 16.168 (1968), pp. 1–5. DOI: 10.2322/jjsass1953.16.1.

[102] A. Narayan, C. Gittelson, and D. Xiu. "A stochastic collocation algorithm with multifidelity models". In: *SIAM Journal on Scientific Computing* 36.2 (2014), A495–A521. DOI: 10.1137/130929461.

[103] A. Nelson, J. Alonso, and T. Pulliam. "Multi-fidelity aerodynamic optimization using treed meta-models". In: *25th AIAA applied aerodynamics conference*. 2007, p. 4057. DOI: 10.2514/6.2007-4057.

[104] W. Oberkampf. "A proposed framework for computational fluid dynamics code calibration/validation". In: *25th Plasmadynamics and Lasers Conference*. American Institute of Aeronautics and Astronautics, June 1994. DOI: 10.2514/6.1994-2540.

[105] W. Oberkampf, J. Helton, and K. Sentz. "Mathematical representation of uncertainty". In: *19th AIAA applied aerodynamics conference*. 2001, p. 1645. DOI: 10.2514/6.2001-1645.

[106] W. L. Oberkampf, T. G. Trucano, and C. Hirsch. "Verification, validation, and predictive capability in computational engineering and physics". In: *Applied Mechanics Reviews* 57.5 (Sept. 2004), pp. 345–384. DOI: 10.1115/1.1767847.

[107] W. L. Oberkampf, T. G. Trucano, and C. Hirsch. "Verification, validation, and predictive capability in computational engineering and physics". In: *Appl. Mech. Rev.* 57.5 (2004), pp. 345–384. DOI: 10.1115/1.1767847.

[108] H. Ouvrard, B. Koobus, A. Dervieux, and M. V. Salvetti. "Classical and variational multiscale LES of the flow around a circular cylinder on unstructured grids". In: *Computers Fluids* 39.7 (Aug. 2010), pp. 1083–1094. DOI: 10.1016/j.compfluid.2010.01.017.

[109] A. S. Padron, J. J. Alonso, F. Palacios, M. F. Barone, and M. S. Eldred. "Multi-fidelity uncertainty quantification: application to a vertical axis wind turbine under an extreme gust". In: *15th AIAA/ISSMO multidisciplinary analysis and optimization conference*. 2014, p. 3013. DOI: 10.2514/6.2014-3013.

[110] P. S. Palar, L. R. Zuhal, K. Shimoyama, and T. Tsuchiya. "Global Sensitivity Analysis via Multi-Fidelity Polynomial Chaos Expansion". In: *Reliability Engineering and System Safety* 170.C (2018), pp. 175–190. DOI: 10.1016/j.ress.2017.10.013.

[111] C. Park, R. T. Haftka, and N. H. Kim. "Remarks on multi-fidelity surrogates". In: *Structural and Multidisciplinary Optimization* 55.3 (2017), pp. 1029–1050. DOI: 10.1007/s00158-016-1550-y.

[112] B. Peherstorfer, K. Willcox, and M. Gunzburger. "Survey of multifidelity methods in uncertainty propagation, inference, and optimization". In: *Siam Review* 60.3 (2018), pp. 550–591. DOI: 10.1137/16M1082469.

[113] N. Pepper, F. Montomoli, and S. Sharma. "Data fusion for Uncertainty Quantification with Non-Intrusive Polynomial Chaos". In: *Computer Methods in Applied Mechanics and Engineering* 374 (2021), p. 113577. DOI: 10.1016/j.cma.2020.113577.

[114] D. A. Phillips and M. J. Soligo. "Will CFD ever Replace Wind Tunnels for Building Wind Simulations?" In: *International Journal of High-Rise Buildings* 8.2 (June 2019), pp. 107–116. DOI: 10.21022/IJHRB.2019.8.2.107.

[115] M. Pisaroni, F. Nobile, and P. Leyland. *Continuation multi-level Monte-Carlo method for uncertainty quantification in turbulent compressible aerodynamics problems modeled by RANS*. Tech. rep. Technical Report 10.2017, École Polytechnique Fédérale de Lausanne, 2017. DOI: 10.13140/RG.2.2.28473.57442.

[116] M. Ravensbergen, T. A. Helgedagsrud, Y. Bazilevs, and A. Korobenko. "A variational multiscale framework for atmospheric turbulent flows over complex environmental terrains". In: *Computer Methods in Applied Mechanics and Engineering* 368 (2020), p. 113182. DOI: 10.1016/j.cma.2020.113182.

[117] P. Richards and S. Norris. "LES modelling of unsteady flow around the Silsoe cube". In: *Journal of Wind Engineering and Industrial Aerodynamics* 144 (2015), pp. 70–78. DOI: 10.1016/j.jweia.2015.03.018.

[118] P. J. Richards and R. P. Hoxey. "Quasi-steady theory and point pressures on a cubic building". In: *Journal of wind engineering and industrial aerodynamics* 92.14-15 (2004), pp. 1173–1190. DOI: 10.1016/j.jweia.2004.07.003.

[119] P. Richards, S. Fong, and R. Hoxey. "Anisotropic turbulence in the atmospheric surface layer". In: *Journal of wind engineering and industrial aerodynamics* 69 (1997), pp. 903–913. DOI: 10.1016/S0167-6105(97)00216-X.

[120] P. Richards and R. Hoxey. "Pressures on a cubic building—Part 1: Full-scale results". In: *Journal of Wind Engineering and Industrial Aerodynamics* 102 (2012), pp. 72–86. DOI: 10.1016/j.jweia.2011.11.004.

[121] P. Richards and R. Hoxey. "Pressures on a cubic building—part 2: quasi-steady and other processes". In: *Journal of wind engineering and industrial aerodynamics* 102 (2012), pp. 87–96. DOI: 10.1016/j.jweia.2011.11.003.

[122] P. Richards and R. Hoxey. "Unsteady flow on the sides of a 6 m cube". In: *Journal of Wind Engineering and Industrial Aerodynamics* 90.12-15 (2002), pp. 1855–1866. DOI: 10.1016/S0167-6105(02)00293-3.

[123] P. Richards and R. Hoxey. "Wind loads on the roof of a 6 m cube". In: *Journal of Wind Engineering and Industrial Aerodynamics* 96.6-7 (2008), pp. 984–993. DOI: 10.1016/j.jweia.2007.06.032.

[124] P. Richards, R. Hoxey, B. Connell, and D. Lander. "Wind-tunnel modelling of the Silsoe Cube". In: *Journal of Wind Engineering and Industrial Aerodynamics* 95.9-11 (2007), pp. 1384–1399. DOI: 10.1016/j.jweia.2007.02.005.

[125] P. Richards, R. Hoxey, and J. Short. "Spectral models for the neutral atmospheric surface layer". In: *Journal of Wind Engineering and Industrial Aerodynamics* 87.2-3 (2000), pp. 167–185. DOI: 10.1016/s0167-6105(00)00035-0.

[126] P. Richards, R. Hoxey, and L. Short. "Wind pressures on a 6 m cube". In: *Journal of Wind Engineering and Industrial Aerodynamics* 89.14-15 (2001), pp. 1553–1564. DOI: 10.1016/S0167-6105(01)00139-8.

[127] P. Richards, R. Hoxey, and B. Wanigaratne. "The effect of directional variations on the observed mean and rms pressure coefficients". In: *Journal of wind engineering and industrial aerodynamics* 54 (1995), pp. 359–367. DOI: 10.1016/0167-6105(94)00067-N.

[128] P. J. Roache. "QUANTIFICATION OF UNCERTAINTY IN COMPUTATIONAL FLUID DYNAMICS". In: *Annual Review of Fluid Mechanics* 29.1 (Jan. 1997), pp. 123–160. DOI: 10.1146/annurev.fluid.29.1.123.

[129] P. Roache, K. Ghia, and F. White. "Editorial policy statement on the control of numerical accuracy". In: *Journal of Fluids Engineering* 108 (1986), p. 2. DOI: 10.1115/1.3242537.

[130] B. Rocchio, A. Mariotti, and M. Salvetti. "Flow around a 5:1 rectangular cylinder: Effects of upstream-edge rounding". In: *Journal of Wind Engineering and Industrial Aerodynamics* 204 (Sept. 2020), p. 104237. DOI: 10.1016/j.jweia.2020.104237.

[131] H. Rutishauser. "On a modification of the QD-algorithm with Graeffe-type convergence". In: *Proc. IFIP Congress, vol. 62*. 1963, pp. 93–96. DOI: 10.1007/bf01601077.

[132] S. D. Sabatino, R. Buccolieri, and P. Salizzoni. "Recent advancements in numerical modelling of flow and dispersion in urban areas: a short review". In: *International Journal of Environment and Pollution* 52.3/4 (2013), p. 172. DOI: 10.1504/IJEP.2013.058454.

[133] E. Sakai, M. Bai, R. Ahlfeld, K. Klemmer, and F. Montomoli. "Bi-fidelity UQ with combination of co-Kriging and arbitrary polynomial chaos: Film cooling with back facing step using RANS and DES". In: *International Journal of Heat and Mass Transfer* 131 (2019), pp. 261–272. DOI: 10.1016/j.ijheatmasstransfer.2018.10.071.

[134] B. V. Sankar and R. V. Marrey. "Analytical method for micromechanics of textile composites". In: *Composites Science and Technology* 57.6 (1997), pp. 703–713. DOI: 10.1016/S0266-3538(97)00030-4.

[135] G. Schewe. "Reynolds-number-effects in flow around a rectangular cylinder with aspect ratio 1:5". In: *Journal of Fluids and Structures* 39 (May 2013), pp. 15–26. DOI: 10.1016/j.jfluidstructs.2013.02.013.

[136] S. Schlesinger. "Terminology for model credibility". In: *SIMULATION* 32.3 (Mar. 1979), pp. 103–104. DOI: 10.1177/003754977903200304.

[137] H. Schlichting. *Boundary-layer theory*. 7th ed. McGraw-Hill series in mechanical engineering. McGraw-Hill, 1979. ISBN: 9780070553347.

[138] K. Shimoyama and A. Inoue. "Uncertainty quantification by the nonintrusive polynomial chaos expansion with an adjustment strategy". In: *AIAA journal* 54.10 (2016), pp. 3107–3116. DOI: 10.2514/1.J054359.

[139] L. Siconolfi, A. Mariotti, and M. Salvetti. "Uncertainty Quantification in Large-Eddy Simulations of the Flow Around a 5: 1 Rectangular Cylinder". In: *Direct and Large-Eddy Simulation X*. Springer, 2018, pp. 101–107. DOI: 10.1007/978-3-319-63212-4_12.

[140] E. Simiu and D. Yeo. *Wind effects on structures: Modern structural design for wind*. John Wiley & Sons, 2019. ISBN: 9781119375883.

[141] P. Sochala, C. Chen, C. Dawson, and M. Iskandarani. "A polynomial chaos framework for probabilistic predictions of storm surge events". In: *Computational Geosciences* 24.1 (2020), pp. 109–128. DOI: 10.1007/s10596-019-09898-5.

[142] M. A. Sprague, S. Ananthan, G. Vijayakumar, and M. Robinson. "ExaWind: A multifidelity modeling and simulation environment for wind energy". In: *Journal of Physics: Conference Series*. Vol. 1452. 1. IOP Publishing. 2020, p. 012071. DOI: 10.1088/1742-6596/1452/1/012071.

[143] A. E. Stagrum, E. Andenæs, T. Kvande, and J. Lohne. "Climate change adaptation measures for buildings—A scoping review". In: *Sustainability* 12.5 (2020), p. 1721. DOI: 10.3390/su12051721.

[144] T. Stathopoulos and H. Wu. "Using Computational Fluid Dynamics (CFD) for Pedestrian Winds". In: *Structures 2004*. American Society of Civil Engineers, May 2004, pp. 1–9. ISBN: 9780784407004. DOI: 10.1061/40700(2004)51.

[145] M. Sterling, C. Baker, P. Richards, R. Hoxey, and A. Quinn. "An investigation of the wind statistics and extreme gust events at a rural site". In: *Wind & structures* 9.3 (2006), pp. 193–215. DOI: 10.12989/was.2006.9.3.193.

[146] M. G. Stewart and X. Deng. "Climate impact risks and climate adaptation engineering for built infrastructure". In: *ASCE-ASME Journal of Risk and Uncertainty in Engineering Systems, Part A: Civil Engineering* 1.1 (2015), p. 04014001. DOI: 10.1061/AJRUA6.0000809.

[147] B. Sudret. "Global sensitivity analysis using polynomial chaos expansions". In: *Reliability engineering & system safety* 93.7 (2008), pp. 964–979. DOI: 10.1016/j.ress.2007.04.002.

[148] B. Sudret. "Global sensitivity analysis using polynomial chaos expansions". In: *Reliability Engineering System Safety* 93.7 (July 2008), pp. 964–979. DOI: 10.1016/j.ress.2007.04.002.

[149] X. Sun, J. Park, J.-I. Choi, and G. H. Rhee. "Uncertainty quantification of upstream wind effects on single-sided ventilation in a building using generalized polynomial chaos method". In: *Building and Environment* 125 (2017), pp. 153–167. DOI: 10.1016/j.buildenv.2017.08.037.

[150] Y. Sun, Y. Heo, M. Tan, H. Xie, C. Jeff Wu, and G. Augenbroe. "Uncertainty quantification of microclimate variables in building energy models". In: *Journal of Building Performance Simulation* 7.1 (2014), pp. 17–32. DOI: 10.1080/19401493.2012.757368.

[151] G. R. Tabor and M. Baba-Ahmadi. "Inlet conditions for large eddy simulation: A review". In: *Computers & Fluids* 39.4 (2010), pp. 553–567. DOI: 10.1016/j.compfluid.2009.10.007.

[152] T. Tamura. "Reliability on CFD estimation for wind-structure interaction problems". In: *Journal of Wind Engineering and Industrial Aerodynamics* 81.1–3 (May 1999), pp. 117–143. DOI: 10.1016/S0167-6105(99)00012-4.

[153] T. Tamura, K. Kondo, H. Kataoka, Y. Ono, and H. Kawai. "Application of LES to wind loading estimation on buildings". In: (2017), 1403163 Bytes. DOI: 10.17608/K6.AUCKLAND.5630992.V1.

[154] G. I. Taylor. "The spectrum of turbulence". In: *Proceedings of the Royal Society of London. Series A-Mathematical and Physical Sciences* 164.919 (1938), pp. 476–490. DOI: 10.1098/rspa.1938.0032.

[155] A. L. Teckentrup, P. Jantsch, C. G. Webster, and M. Gunzburger. "A multilevel stochastic collocation method for partial differential equations with random input data". In: *SIAM/ASA Journal on Uncertainty Quantification* 3.1 (2015), pp. 1046–1074. DOI: 10.1137/140969002.

[156] L. Temmerman, M. A. Leschziner, C. P. Mellen, and J. Fröhlich. "Investigation of wall-function approximations and subgrid-scale models in large eddy simulation of separated flow in a channel with streamwise periodic constrictions". In: *International Journal of Heat and Fluid Flow* 24.2 (2003), pp. 157–180. DOI: 10.1016/S0142-727X(02)00222-9.

[157] M. S. Thordal, J. C. Bennetsen, S. Capra, and H. H. H. Koss. "Towards a standard CFD setup for wind load assessment of high-rise buildings: Part 1–Benchmark of the CAARC building". In: *Journal of Wind Engineering and Industrial Aerodynamics* 205 (2020), p. 104283. DOI: 10.1016/j.jweia.2020.104283.

[158] Y. Tominaga, A. Mochida, R. Yoshie, H. Kataoka, T. Nozu, M. Yoshikawa, and T. Shirasawa. "AIJ guidelines for practical applications of CFD to pedestrian wind environment around buildings". In: *Journal of Wind Engineering and Industrial Aerodynamics* 96.10–11 (Oct. 2008), pp. 1749–1761. DOI: 10.1016/j.jweia.2008.02.058.

[159] R. W. Walters and L. Huyse. *Uncertainty analysis for fluid mechanics with applications*. Tech. rep. NATIONAL AERONAUTICS and SPACE ADMINISTRATION HAMPTON VA LANGLEY RESEARCH CENTER, 2002.

[160] H. G. Weller, G. Tabor, H. Jasak, and C. Fureby. "A tensorial approach to computational continuum mechanics using object-oriented techniques". In: *Computers in physics* 12.6 (1998), pp. 620–631. DOI: 10.1063/1.168744.

[161] H. Werner and H. Wengle. "Large-eddy simulation of turbulent flow over and around a cube in a plate channel". In: *Turbulent shear flows 8*. Springer, 1993, pp. 155–168. DOI: 10.1007/978-3-642-77674-8_12.

[162] A. Winterstein. "Modeling and simulation of wind-structure interaction of slender civil engineering structures including vibration mitigation systems". PhD thesis. 2020.

[163] J. Witteveen, P. S. Omrani, A. Mariotti, M. V. Salvetti, L. Bruno, and N. Coste. "Uncertainty Quantification of the Aerodynamics of a Rectangular 5:1 Cylinder". In: *Uncertainty Quantification in Computational Fluid Dynamics, Pisa, Italy*. 2014.

[164] W. Wood, M. Bossak, and O. Zienkiewicz. "An alpha modification of Newmark's method". In: *International journal for numerical methods in engineering* 15.10 (1980), pp. 1562–1566. DOI: 10.1002/nme.1620151011.

[165] S. Wornom, H. Ouvrard, M. V. Salvetti, B. Koobus, and A. Dervieux. "Variational multiscale large-eddy simulations of the flow past a circular cylinder: Reynolds number effects". In: *Computers Fluids* 47.1 (Aug. 2011), pp. 44–50. DOI: 10.1016/j.compfluid.2011.02.011.

[166] N. G. Wright and G. Easom. "Non-linear k–ε turbulence model results for flow over a building at full-scale". In: *Applied Mathematical Modelling* 27.12 (2003), pp. 1013–1033. DOI: 10.1016/S0307-904X(03)00123-9.

[167] T. Wu and A. Kareem. "A low-dimensional model for nonlinear bluff-body aerodynamics: a peeling-an-onion analogy". In: *Journal of Wind Engineering and Industrial Aerodynamics* 146 (2015), pp. 128–138. DOI: 10.1016/j.jweia.2015.08.009.

[168] D. Xiu and G. E. Karniadakis. "Modeling uncertainty in flow simulations via generalized polynomial chaos". In: *Journal of computational physics* 187.1 (2003), pp. 137–167. DOI: 10.1016/S0021-9991(03)00092-5.

[169] D. Xiu and G. E. Karniadakis. "The Wiener–Askey Polynomial Chaos for Stochastic Differential Equations". In: *SIAM Journal on Scientific Computing* 24.2 (2002), pp. 619–644. DOI: 10.1137/S1064827501387826.

[170] D. Xiu, D. Lucor, C.-H. Su, and G. E. Karniadakis. "Stochastic modeling of flow-structure interactions using generalized polynomial chaos". In: *J. Fluids Eng.* 124.1 (2002), pp. 51–59. DOI: 10.1115/1.1436089.

[171] R. Yoshie, A. Mochida, Y. Tominaga, H. Kataoka, K. Harimoto, T. Nozu, and T. Shirasawa. "Cooperative project for CFD prediction of pedestrian wind environment in the Architectural Institute of Japan". In: *Journal of Wind Engineering and Industrial Aerodynamics* 95.9–11 (Oct. 2007), pp. 1551–1578. DOI: 10.1016/j.jweia.2007.02.023.

Bisherige Titel der Schriftenreihe

Band	Titel
1	Frank Koschnick, *Geometrische Lockingeffekte bei Finiten Elementen und ein allgemeines Konzept zu ihrer Vermeidung*, 2004.
2	Natalia Camprubi, *Design and Analysis in Shape Optimization of Shells*, 2004.
3	Bernhard Thomee, *Physikalisch nichtlineare Berechnung von Stahlfaserbetonkonstruktionen*, 2005.
4	Fernaß Daoud, *Formoptimierung von Freiformschalen - Mathematische Algorithmen und Filtertechniken*, 2005.
5	Manfred Bischoff, *Models and Finite Elements for Thin-walled Structures*, 2005.
6	Alexander Hörmann, *Ermittlung optimierter Stabwerkmodelle auf Basis des Kraftflusses als Anwendung plattformunabhängiger Prozesskopplung*, 2006.
7	Roland Wüchner, *Mechanik und Numerik der Formfindung und Fluid-Struktur-Interaktion von Membrantragwerken*, 2006.
8	Florian Jurecka, *Robust Design Optimization Based on Metamodeling Techniques*, 2007.
9	Johannes Linhard, *Numerisch-mechanische Betrachtung des Entwurfsprozesses von Membrantragwerken*, 2009.
10	Alexander Kupzok, *Modeling the Interaction of Wind and Membrane Structures by Numerical Simulation*, 2009.

Band Titel

11 Bin Yang, *Modified Particle Swarm Optimizers and their Application to Robust Design and Structural Optimization*, 2009.

12 Michael Fleischer, *Absicherung der virtuellen Prozesskette für Folgeoperationen in der Umformtechnik*, 2009.

13 Amphon Jrusjrungkiat, *Nonlinear Analysis of Pneumatic Membranes - From Subgrid to Interface*, 2009.

14 Alexander Michalski, *Simulation leichter Flächentragwerke in einer numerisch generierten atmosphärischen Grenzschicht*, 2010.

15 Matthias Firl, *Optimal Shape Design of Shell Structures*, 2010.

16 Thomas Gallinger, *Effiziente Algorithmen zur partitionierten Lösung stark gekoppelter Probleme der Fluid-Struktur-Wechselwirkung*, 2011.

17 Josef Kiendl, *Isogeometric Analysis and Shape Optimal Design of Shell Structures*, 2011.

18 Joseph Jordan, *Effiziente Simulation großer Mauerwerksstrukturen mit diskreten Rissmodellen*, 2011.

19 Albrecht von Boetticher, *Flexible Hangmurenbarrieren: Eine numerische Modellierung des Tragwerks, der Hangmure und der Fluid-Struktur-Interaktion*, 2012.

20 Robert Schmidt, *Trimming, Mapping, and Optimization in Isogeometric Analysis of Shell Structures*, 2013.

21 Michael Fischer, *Finite Element Based Simulation, Design and Control of Piezoelectric and Lightweight Smart Structures*, 2013.

22 Falko Hartmut Dieringer, *Numerical Methods for the Design and Analysis for Tensile Structures*, 2014.

Band Titel

23 Rupert Fisch, *Code Verification of Partitioned FSI Environments for Lightweight Structures*, 2014.

24 Stefan Sicklinger, *Stabilized Co-Simulation of Coupled Problems Including Fields and Signals*, 2014.

25 Madjid Hojjat, *Node-based parametrization for shape optimal design*, 2015.

26 Ute Israel, *Optimierung in der Fluid-Struktur-Interaktion - Sensitivitätsanalyse für die Formoptimierung auf Grundlage des partitionierten Verfahrens*, 2015.

27 Electra Stavropoulou, *Sensitivity analysis and regularization for shape optimization of coupled problems*, 2015.

28 Daniel Markus, *Numerical and Experimental Modeling for Shape Optimization of Offshore Structures*, 2015.

29 Pablo Suárez, *Design Process for the Shape Optimization of Pressurized Bulkheads as Components of Aircraft Structures*, 2015.

30 Armin Widhammer, *Variation of Reference Strategy - Generation of Optimized Cutting Patterns for Textile Fabrics*, 2015.

31 Helmut Masching, *Parameter Free Optimization of Shape Adaptive Shell Structures*, 2016.

32 Hao Zhang, *A General Approach for Solving Inverse Problems in Geophysical Systems by Applying Finite Element Method and Metamodel Techniques*, 2016.

33 Tianyang Wang, *Development of Co-Simulation Environment and Mapping Algorithms*, 2016.

34 Michael Breitenberger, *CAD-integrated Design and Analysis of Shell Structures*, 2016.

Band Titel

35 Önay Can, *Functional Adaptation with Hyperkinematics using Natural Element Method: Application for Articular Cartilage*, 2016.

36 Benedikt Philipp, *Methodological Treatment of Non-linear Structural Behavior in the Design, Analysis and Verification of Lightweight Structures*, 2017.

37 Michael Andre, *Aeroelastic Modeling and Simulation for the Assessment of Wind Effects on a Parabolic Trough Solar Collector*, 2018.

38 Andreas Apostolatos, *Isogeometric Analysis of Thin-Walled Structures on Multipatch Surfaces in Fluid-Structure Interaction*, 2018.

39 Altuğ Emiroğlu, *Multiphysics Simulation and CAD-Integrated Shape Optimization in Fluid-Structure Interaction*, 2019.

40 Reza Najian Asl, *Shape optimization and sensitivity analysis of fluids, structures, and their interaction using Vertex Morphing Parametrization*, 2019.

42 Ahmed Abodonya, *Verification Methodology for Computational Wind Engineering Prediction of Wind Loads on Structures*, 2020.

43 Anna Maria Bauer, *AD-integrated Isogeometric Analysis and Design of Lightweight Structures*, 2020.

44 Andreas Winterstein, *Modeling and Simulation of Wind-Structure Interaction of Slender Civil Engineering Structures Including Vibration Mitigation Systems*, 2020.

45 Franz-Josef Ertl, *Vertex Morphing for constrained shape optimization of three-dimensional solid structures*, 2020.

46 Daniel Baumgärtner, *On the grid-based shape optimization of structures with internal flow and the feedback of shape changes into a CAD model*, 2020.

Band Titel

47 Mohamed Magdi Mohamed Mohamed Khalil, *Combining Physics-Based Models and Machine Learning for an Enhanced Structural Health Monitoring*, 2021.

48 Long Chen, *Gradient descent akin method*, 2021.

49 Aditya Ghantasala, *Coupling Procedures for Fluid-Fluid and Fluid-Structure Interaction Problems Based on Domain Decomposition Methods*, 2021.

50 Ann-Kathrin Goldbach, *The CAD-integrated Design Cycle for Structural Membranes*, 2021.

51 Iñigo Pablo López Canalejo, *A Finite-Element Transonic Potential Flow Solver with an Embedded Wake Approach for Aircraft Conceptual Design*, 2022